3D SPHEROID CULTURE SYSTEMS FOR METASTATIC PROSTATE CANCER DORMANCY STUDIES AND ANTI-CANCER THERAPEUTICS DEVELOPMENT

by

Amy Yu-Ching Hsiao

A dissertation submitted in partial fulfillment
of the requirements for the degree of
Doctor of Philosophy
(Biomedical Engineering)
in The University of Michigan
2011

Doctoral Committee:

Professor Shuichi Takayama, Chair
Professor Kenneth J. Pienta
Professor Russell S. Taichman
Associate Professor Joseph L. Bull
Assistant Professor Mohamed El-Sayed

To My Family

ACKNOWLEDGEMENTS

This dissertation reflects far beyond the culmination of research works I contributed over the years of study. It also manifests lifelong friendships, mentorships, and teamwork spirits I had experienced during the course of my graduate studies.

First, I would like to thank and express my sincerest gratitude towards my advisor, Professor Shuichi Takayama, for giving me the precious opportunity to work with him and learn from him throughout my graduate career. Thinking back to five years ago when I was still an immature undergraduate student unsure and hesitant about my future, it was his personal invitation e-mail that connected me to the fascinating research that he has been conducting and ultimately inspired me to join the graduate research force in Michigan. His kindness, creativity, enthusiasm, passion, vision, attitude, wisdom, and intellect have always motivated me to become a better researcher and make a difference in the world. His dedication to innovative research and commitment to students' developments have definitely greatly influenced the lives of many students like me. I am very thankful and proud to have been one of his students. In the past few years, I have truly learned from him not only countless valuable lessons in conducting meaningful high-quality research, but also invaluable lessons about life. Without his continued guidance and support for me, this work would not have been possible. Throughout the pursuit of my Ph.D., he has strengthened me with his patience when I was struggling, his

guidance when I was lost, his support when I was motivated, and his encouragements when I was down. The lessons I learned from Professor Takayama will always be treasured in my heart and serve as basis for all of my future endeavors as I grow through life.

Next, I would like to thank my committee members for all their support, help, teaching, advice, and guidance throughout my graduate studies. I am deeply grateful to Professor Kenneth Pienta for his clinical experience, expertise, assistance, and teaching in all of the clinical and biological sides of my projects. His sustained interest in applying innovative micro-technologies to study prostate cancer opened up opportunities for collaboration from the start of my graduate career. His tremendous support and encouragements have motivated me and made significant contributions to this research. I would also like to express my special thanks to Professor Russell Taichman for all the constructive advice and profound insights he has provided throughout the years. Without his ideas, this research would not have been complete. His continued guidance, support, and confidence in me have helped me grow as a researcher. I would also like to express my sincere gratitude to Professor Joseph Bull, who has been a great, interactive teacher and a dedicated committee member of mine. He has taught me valuable lessons through classes and provided constructive feedback on my research. I would also like to gratefully acknowledge Professor Mohamed El-Sayed for his helpful discussions and novel insights into spheroid research. I have truly learned a lot from him as a dedicated researcher.

I am also very grateful to have Dr. Yu-suke Torisawa and Dr. Yi-Chung Tung as my research mentors throughout my graduate career. As a novice researcher in the lab, they have taught me lessons in how to conduct basic research step by step since I first joined the lab. Their teachings, support, assistance, helpful discussions, constructive criticisms, advice, guidance, and encouragements have shaped me into an independent and confident researcher to conduct the works described in this dissertation. They will always serve as my role models for the rest of my career.

In addition to the professors and mentors who have guided me throughout my graduate career, I would also like to gratefully recognize the friendship, teamwork, collaboration, support, and help from all former and current Takayama lab members. I have been extremely fortunate to have the privilege to work and be friends with: Steven Allen, Tommaso Bersano-Begey, Steve Cavnar, Wansik Cha, Bor-Han Chueh, Yao-Kuang Chung, Angela Dixon, Nick Douville, John Frampton, Nobuyuki Futai, Yunseok Heo, Dongeun Huh, Andreja Jovic, Yoko Kamotani, Albert Kao, Nobuhiro Kato, Kerim Kaylan, Byoung Choul Kim, Sung Jin Kim, Jason Kuo, Joseph Labuz, Qianyi Lee, David Lai, Ran Li, Yan Chen Liu, Toshiki Matsuoka, Geeta Mehta, Roberto Miguez, Chris Moraes, Bobak Mosadegh, Joong Yull Park, Tejash Patel, Sasha Cai Lesher-Perez, Poorna Ramamurthy, Whi Jae Roh, Amir Sarvestani, Christopher Shah, Young Jae Shin, Arlyne Simon, Jonathan Song, Hossein Tavana, Joshua White, Jonathan Yin, and Ying Zheng. I would also like to thank my collaborators: Rachel Bedenis, Anjali Mishra, Lalit Patel, Yusuke Shiozawa, and Sudha Sud, and express my deepest gratitude towards all of the wonderful staff members in the Department of Biomedical Engineering, especially

Mayte Brown, Maria Steele, Susan Bitzer, Ruth Halsey, Tonya Brown, Kathy McCrumb, Amanda Nelson, and Katharine Guarino. I also deeply appreciate the friendship, hospitality, support, and encouragements from all the friends I have met in Michigan. I know I will miss all the laughter and tears I shared with all of you. Thank you all for being part of my life.

Finally, I would like to express my love and deepest gratitude to my family for their endless love, encouragements, endurance, patience, and support throughout this long journey. Their belief and confidence in my abilities through times of my successes and failures are the main reasons for all of my achievements. Many thanks to my father Hsien-Jen Hsiao who has always been very proud of all of my accomplishments, my mother Regina Hsiao who has always been beside me through rain and shine, and my brother David Hsiao who has always been supportive of my decisions all years long. Thank you for always being there for me.

TABLE OF CONTENTS

LIST OF FIGURES

FIGURE

Chapter 2

Chapter 3

Chapter 4

Chapter 5

Chapter 6

LIST OF TABLES

TABLE

ABSTRACT

Prostate cancer is the most common non-skin cancer in United States men. Despite recent advances, mortality still remains high due to the emergence of therapy-resistant cancer cells that metastasize. Recently it has been postulated that only cancer stem cells (CSCs) are able to establish metastases, and therefore are the essential targets to destroy. Unfortunately, current use of CSCs is limited by the small number of CSCs that can be isolated, and the difficulty of culturing the CSCs *in vitro*. Furthermore, current *in vitro*-based metastatic prostate cancer models do not faithfully recreate the complex multi-cellular, three-dimensional (3D) tumor microenvironment seen *in vivo*. It is therefore crucial to develop effective *in vitro* prostate cancer culture and testing systems that mimic the actual *in vivo* tumor niche microenvironment. Here we utilized novel microscale technologies to develop an accurate 3D metastatic tumor model for detailed study of metastatic prostate cancer dormancy as well as accurate anti-cancer therapeutics screening and testing *in vitro*. Guided by the observation that prostate cancer cells parasitize and stay quiescent in the hematopoietic stem cell niche that is rich in osteoblasts and endothelial cells *in vivo*, a microfluidic device was established to create 3D spheroid culture of prostate cancer cells supported by osteoblasts and endothelial cells. This 3D metastatic prostate cancer model recapitulates the physiologic, dormant growth behavior of prostate cancer cells in the hematopoietic stem cell niche. Furthermore, we developed a hanging drop-based high-throughput platform for general formation, stable

long-term culture, and robust drug testing and screening of 3D spheroids. Using this platform, we found significant differences in drug sensitivities against cells cultured under conventional 2D conditions versus physiological 3D models. A variety of techniques and methods were also established to specifically pattern the spatial localization of different co-culture cell types within a spheroid in this platform for accurate engineering of the 3D metastatic prostate cancer niche microenvironment. Collectively, these biological findings and technological innovations have led to advances in the understanding of prostate cancer biology and progress towards development of novel tools and therapeutics to fight against tumorigenic cancer cells.

CHAPTER 1

Introduction

Cancer is the second leading cause of death in the United States (Comprehensive Cancer Information—National Cancer Institute). Developments in the past decades have no doubt brought significant advancements to our current understanding and treatments of cancer. Nevertheless, as of today, many metastatic cancers such as prostate cancer still remain incurable. Prostate cancer is the most common non-skin cancer in United States men (Prostate Cancer Foundation). Despite recent advances, prostate cancer mortality still remains high due to the emergence of therapy-resistant cancer cells that metastasize (Hellerstedt and Pienta 2002). It has been postulated that only a subset of cancer cells called cancer stem cells (CSCs) are able to establish metastases and regenerate tumors (Li *et al*. 2007; Croker and Allan 2008; Kelly and Yin 2008). In turn, these CSCs directly contribute to the progression of prostate cancer metastasis and ultimately lead to deaths in patients. Therefore, it is critical to find novel approaches to specifically target and destroy prostate CSCs. An understanding of these prostate CSCs has fundamental impacts in cancer biology and advancements in medicine.

Unfortunately, current use of CSCs is limited by the small number of CSCs that can be isolated and the difficulty of maintaining the CSCs in undifferentiated states in *in vitro* cultures. CSCs typically only make up 0.1 to 2% of the bulk cancer cell population.

Culture of isolated CSCs in the conventional two-dimensional (2D) petri-dishes generally leads to spontaneous differentiation back to the bulk cancer cell population. Alternatively, CSCs have been enriched in animal models (Al-Hajj *et al*. 2003), but such *in vivo* cultures are very tedious, expensive, and not efficient. It is therefore essential to develop an effective *in vitro* CSC culture and testing system to better study the biology of these delicate CSCs. Just like how normal stem cells tend to reside in special "niches," it has also been suggested that CSCs are likely to be maintained in microenvironmental niches in tumors (Dontu *et al*. 2005; Croker and Allan 2008; Kelly and Yin 2008; Li and Neaves 2006; Li *et al*. 2007). However, current *in vitro*-based metastatic prostate cancer models do not faithfully recreate the complex multi-cellular, three-dimensional (3D) tumor microenvironments seen *in vivo*. Taking into account the importance of stem cell-niche interactions, it is crucial to develop a system that mimics the actual *in vivo* CSC niche microenvironment *in vitro*.

The work described in this dissertation presents multidisciplinary efforts directed towards the development of novel microscale systems to engineer accurate 3D metastatic prostate cancer and CSC models *in vitro* for detailed study of dormancy and anti-cancer drug development. The central biological concept of the thesis is built upon the niche parasitism hypothesis (proposed by Professor Russell S. Taichman and Professor Kenneth J. Pienta at the University of Michigan's Dental School and Medical School), which states that prostate cancer metastasis to the bone is mediated by prostate CSCs that localize to the hematopoietic stem cell (HSC) niche and function as parasites on the niche to facilitate growth and survival (Shiozawa *et al*. 2008; Shiozawa *et al*. 2008; Shiozawa

et al. 2010). The HSC niche, in turn, is comprised of multiple cell types including osteoblasts and endothelial cells delicately organized into 3D structures with tightly regulated oxygen tension (Shiozawa et al. 2008; Yin and Li 2006). Replication of such complex *in vivo* niche organization *in vitro* requires highly sophisticated 3D cell co-culture systems to be engineered to capture all the vital elements of the niche. This research effort has utilized novel microscale technologies to create 3D *in vitro* niches to mimic the prostate CSC and bulk prostate cancer cell microenvironment at the bone metastatic site. Such metastatic prostate cancer model can subsequently be used to study tumor dormancy and serve as base model for anti-cancer drug screening and testing.

To mimic *in vivo* situations *in vitro* accurately, the concepts of 3D culture and co-culture of multiple cell types become highly essential. With the realization that the surrounding environment is critical to cells, various 3D culture systems that better mimic physiological tissues have been valued as important research tools. Spheroids, which are spherical clusters of cells formed by self-assembly, stand out as one of the best models for 3D culture (Kunz-Schughart *et a*l. 2004; Friedrich *et al*. 2009). Due to their spherical structure, spheroids are excellent models for solid tumors and are known to provide more accurate and meaningful biological readouts compared to 2D models (Kunz-Schughart *et al*. 2004). Multiple cell types can also be incorporated into a single spheroid construct as co-culture model (Kelm and Fussenegger 2004). Currently, however, most biological experiments and studies in drug development are still based on 2D cell assays, which often skew research results and have limited predictive power in clinical efficacy (Hirschhaeuser *et al*. 2010). Although the advantages of 3D spheroid cultures are widely

known, typical spheroid culture methods are often tedious, low-throughput, difficult to handle, and produce non-uniform samples. Various such complications have thus hindered more researchers from adapting the more accurate 3D spheroid cultures into routine use in research.

Recent advances in micro-technologies offer great potentials to improve current state of the art *in vitro*-based cell culture systems for accurate biological studies. Microfluidic systems allow for integration of physiologically relevant elements and dimensions into *in vitro* cell culture devices in a simplified and efficient manner without extra operational complexities. Custom engineered platforms also allow for creation of multiple independent cellular compartments in high-throughput manners for parallel experiments, multiplexing, screening, and testing purposes.

The objective of this thesis research was to develop 3D cell culture platforms specifically designed to advance the understanding of prostate cancer metastasis and enhance current 3D anti-cancer drug screening and testing standards. The common themes among the research presented in this thesis include microscale systems and 3D spheroid cultures. Specifically, Chapter 2 describes the establishment and characterization of an accurate *in vitro* 3D metastatic prostate cancer model containing bulk prostate cancer cells and potential prostate CSCs. Guided by the recent observation that prostate CSCs parasitize to the HSC niche that is rich in osteoblasts and endothelial cells *in vivo*, a microfluidic device was used to create 3D spheroid culture of prostate cancer cells and prostate CSC-enriched $CD133^{+}$ subpopulation supported by osteoblasts

and endothelial cells. The growth behavior of the prostate cancer cells and $CD133^+$ prostate cancer cells in this model was subsequently characterized and found to be relatively quiescent. This model recapitulates the physiologic, quiescent growth behavior of prostate cancer cells and $CD133^+$ subpopulation in the HSC niche at their dormancy stage of metastasis, which is an excellent intervention point to prevent the outbreak of a full-blown metastasis that is often lethal. Since the dormant growth phenomenon of prostate cancer cells and $CD133^+$ prostate cancer cells in the model closely mimics the behavior of prostate cancer cells *in vivo* when they parasitize the HSC niche, the model is excellent for detailed biological studies of dormancy in prostate cancer metastasis and development of therapeutics that specifically target dormant metastatic prostate cancer cells. The quiescent behavior of the cells is an important characteristic of tumor dormancy that had not been previously achieved in conventional 2D mono-cultures. It is a feature of cancer metastasis previously difficult to study and recapitulate *in vitro*.

The work from Chapter 3 also extends the theme of microscale 3D spheroid culture, but here the system is scaled up to a high-throughput platform that can easily be mass produced for high-throughput screening (HTS) purposes. This new innovation greatly simplifies the tedious procedures required by the conventional spheroid formation methods and makes 3D cell culture as straightforward as conventional 2D cultures. The platform is based on the conventional spheroid formation method—hanging drop technique, and is designed to the standard 384-well plate format for compatibility with existing HTS instruments. This versatile 384 hanging drop array plate is not just for the culture of the metastatic prostate cancer models, but could also be used for 3D spheroid

formation of a wide variety of normal and diseased cell types. Using this platform, two distinct anti-cancer drugs have been demonstrated to have differential effects on cells cultured in 2D versus 3D, depending on the drug mode of action. This system introduces a simple, user-friendly solution to the typically complicated, cumbersome, and expensive 3D cell culture for the entire cell culture community. The plate is simple enough for routine long-term 3D cell culture in academia, yet also in a high-throughput format suitable for the pharmaceutical industry. This platform is envisioned to revolutionize current drug screening standards by the introduction of an efficient 3D cell culture based HTS platform. 3D cell cultures offer biologically relevant insights that are often lost and unattainable from 2D monolayer cultures. These advantages will positively contribute to future advancements in anti-cancer therapeutics.

Building upon the development described in Chapter 3, Chapter 4 further characterizes and improves the 384 hanging drop array plate to promote wider use of the high-throughput platform by a broader range of disciplines. The plate is shown to have excellent assay performances and therefore demonstrates its suitability for HTS applications such as drug screening and testing. The actual design of the plate was further refined to optimize for greater long-term stability of the hanging drops. The versatility of the plate is also demonstrated through the 3D spheroid culture of a wide variety of cell types, the ease of spheroid transferring and retrieval for further experimentation or analysis, and various 3D co-culture and patterning techniques allowed by the user-friendliness of the 384 hanging drop array plate.

Finally, works from Chapter 5 attempts to elucidate the factors contributing to the quiescent behavior of prostate cancer cells and $CD133^+$ subpopulation observed in the metastatic prostate cancer spheroid model described in Chapter 2 by utilizing the high-throughput 384 hanging drop array platform developed in Chapter 3 and Chapter 4. Effort to explore the underlying mechanisms that are regulating the $CD133^+$ prostate cancer cells in more depth was achieved through looking at the $CD133^+$ subpopulation's expression levels of key genes implicated in stem cell self-renewal, quiescence, homing, and localization. In addition to the proliferation rate data presented in Chapter 2, the quiescence of the prostate cancer cells cultured in the co-culture spheroids was further evaluated by looking at their cell cycling stage. Chapter 5 presents preliminary data on current characterizations in the key stem cell-relevant gene expression profiles in the $CD133^+$ subpopulation and the cell cycling stage of prostate cancer cells. Additional efforts are required to elucidate the underlying biology in keeping the $CD133^+$ prostate cancer cells quiescent and thus maintaining their stem-like markers.

Collectively, this dissertation highlights sophisticated utilization of micro-technologies to develop user-friendly platforms and engineer accurate models that closely mimic *in vivo* situations to study and answer fundamental cancer biology questions. In addition, the developed platforms allow for accurate, efficient, and effective drug screening and testing on 3D cellular models, which will eventually lead to advancements in medicine and anti-cancer therapeutics. The eventual translational goal is to introduce our simple 3D culture technologies to clinicians to enable efficient and reliable formation of physiologic tumor microtissues from the small number of patient-specific cancer cells

for individualized evaluation of anti-cancer drug sensitivity and develop specialized treatment options. The works described here demonstrate successful development of novel cutting-edge devices to improve current research methods in biology by establishing physiologically relevant models and introducing user-friendly techniques to clinicians and biologists to solve existing problems.

1.1 References

1. Al-Hajj M, Wicha MS, Benito-Hernandez A, Morrison SJ, Clarke MF. Prospective identification of tumorigenic breast cancer cells. Proc Natl Acad Sci U S A 2003;100(7):3983-8.

2. Comprehensive Cancer Information—National Cancer Institute: www.cancer.gov

3. Croker AK, Allan AL. Cancer stem cells: implications for the progression and treatment of metastatic disease. J Cell Mol Med 2008;12(2):374-90.

4. Dontu G, Liu S, Wicha MS. Stem cells in mammary development and carcinogenesis: implications for prevention and treatment. Stem Cell Rev 2005;1(3):207-13.

5. Friedrich J, Seidel C, Ebner R, Kunz-Schughart LA. Spheroid-based drug screen: considerations and practical approach. Nat Protoc 2009;4(3):309-24.

6. Hellerstedt BA, Pienta KJ. The current state of hormonal therapy for prostate cancer. CA Cancer J Clin 2002;52(3):154-79.

7. Hirschhaeuser F, Menne H, Dittfeld C, West J, Mueller-Klieser W, Kunz-Schughart LA. Multicellular tumor spheroids: an underestimated tool is catching up again. J Biotechnol 2010;148(1):3-15.

8. Kelly K, Yin JJ. Prostate cancer and metastasis initiating stem cells. Cell Res 2008;18(5):528-37.

9. Kelm JM, Fussenegger M. Microscale tissue engineering using gravity-enforced cell assembly. Trends Biotechnol 2004;22(4):195-202.

10. Kunz-Schughart LA, Freyer JP, Hofstaedter F, Ebner R. The use of 3-D cultures for high-throughput screening: the multicellular spheroid model. J Biomol Screen 2004;9(4):273-85.

11. Li F, Tiede B, Massague J, Kang Y. Beyond tumorigenesis: cancer stem cells in metastasis. Cell Res 2007;17(1):3-14.

12. Li H, Fan X, Houghton JM. Tumor microenvironment: the role of the tumor stroma in cancer. J Cell Biochem 2007;101(4):805-15.

13. Li L, Neaves WB. Normal stem cells and cancer stem cells: the niche matters. Cancer Res 2006;66(9):4553-7.

14. Prostate Cancer Foundation: www.pcf.org

15. Shiozawa Y, Havens AM, Jung Y, Ziegler AM, Pedersen EA, Wang J, et al. Annexin II/Annexin II receptor axis regulates adhesion, migration, homing, and growth of prostate cancer. J Cell Biochem 2008;105(2):370-80.

16. Shiozawa Y, Havens AM, Pienta KJ, Taichman RS. The bone marrow niche: habitat to hematopoietic and mesenchymal stem cells, and unwitting host to molecular parasites. Leukemia 2008;22(5):941-50.

17. Shiozawa Y, Pedersen EA, Patel LR, Ziegler AM, Havens AM, Jung Y, et al. GAS6/AXL axis regulates prostate cancer invasion, proliferation, and survival in the bone marrow niche. Neoplasia 2010;12(2):116-27.

18. Yin T, Li L. The stem cell niche in bone. J Clin Invest 2006;116(5):1195-201.

CHAPTER 2

Microfluidic System for Formation of PC-3 Prostate Cancer Co-culture Spheroids

The niche microenvironment in which cancer cells reside plays a prominent role in the growth of cancer. It is therefore imperative to mimic the *in vivo* tumor niche *in vitro* to better understand cancer and enhance development of therapeutics. Here, we engineer a 3D metastatic prostate cancer model that includes the types of surrounding cells in the bone microenvironment that the metastatic prostate cancer cells reside in. Specifically, we used a two-layer microfluidic system to culture 3D multi-cell type spheroids of fluorescently labeled metastatic prostate cancer cells (PC-3 cell line), osteoblasts and endothelial cells. This method ensures uniform incorporation of all co-culture cell types into each spheroid and keeps the spheroids stationary for easy tracking of individual spheroids and the PC-3's residing inside them over the course of at least a week. This culture system greatly decreased the proliferation rate of PC-3 cells without reducing viability and may more faithfully recapitulate the *in vivo* growth behavior of malignant cancer cells within the bone metastatic prostate cancer microenvironment.

2.1 Introduction

Cancer stem cells (CSCs) are postulated to be central to the establishment of metastases and the main challenge to the cure of cancer (Li *et al*. 2007; Croker and Allan 2008; Kelly and Yin 2008). Currently, however, the use of CSCs in research is limited by the small number of CSCs that can be isolated, and the spontaneous differentiation in *in vitro* cultures. The challenge of *in vitro* CSC culture is likely due, at least in part, to the lack of supportive microenvironmental niches (Li *et al*. 2007; Croker and Allan 2008; Kelly and Yin 2008; Dontu *et al*. 2005; Li and Neaves 2006) in conventional two-dimensional (2D) cultures. Bone metastasis, which is the most severe complication and leading cause of morbidity and ultimately mortality in prostate cancer (Taichman *et al*. 2007; Sun *et al*. 2007), provides clues for recreating a supportive CSC niche environment for prostate cancer cells. Recent data from our group suggests that prostate cancer utilizes the hematopoietic stem cell (HSC) homing mechanisms to metastasize to the bone marrow and thrive in the niche (Shiozawa *et al*. 2008; 2010). Based on this hypothesis that prostate cancers parasitize the niche, we have developed microscale 3D spheroid culture of prostate cancer cells supported by cells from the HSC niche. Here, we describe a microfluidic 3D culture system that recapitulates the *in vivo* growth behavior of malignant prostate cancer cells, specifically PC-3 cells, through construction of an *in vitro* bone metastatic prostate cancer microenvironment.

To develop a supportive metastatic prostate cancer model, we hypothesized that it would be crucial to culture the cells in 3D along with the surrounding cells in the

microenvironment that the metastatic prostate cancer cells reside in (Abbott 2003; Griffith and Swartz 2006; Yamada and Cukierman 2007). For example, cells are known to proliferate at a much slower rate that is more physiological when cultured in 3D than 2D (Mueller-Klieser 1997; Torisawa *et al*. 2005; Hotary *et al*. 2003). It is also known that prostate cancer cells not only proliferate differently when co-cultured with other stromal cells or fibroblasts, but can also affect the proliferation rates of the other cell types under various *in vitro* and *in vivo* models (Camps *et a*l., 1990; Yang *et al*. 2001; Barrett *et al*. 2005). We adopted co-culture spheroids as a 3D prostate cancer niche model.

Spheroids are sphere-shaped cell colonies formed by self-assembly that allow various growth and functional studies of diverse tissues (Ingram *et al*. 1997). Spheroids serve as excellent physiologic tumor models as they mimic avascular tumors and micrometastases (Klob *et al*. 2008) and are known to provide more reliable and meaningful therapeutic readouts (Kunz-Schughart *et al*. 2004). Although these advantages of tumor spheroids has been widely recognized (Kelm and Fussenegger 2004), challenges involved in the tedious procedures required for formation, maintenance, solution exchange, and microscale cell and fluid manipulation are still holding back the industry from using the well-validated spheroid tissue model more widely.

Formation of spheroids occurs spontaneously, in environments where cell-cell interaction dominates over cell-substrate interactions. Typical methods for spheroid generation include hanging drops, culture of cells on non-adherent surfaces, spinner flask

cultures, and NASA rotary cell culture systems (Lin and Chang 2008; Friedrich *et al*. 2007). Recently, various groups have also developed spheroids on a chip works utilizing microscale technologies such as microwell arrays and microfluidic devices (Torisawa *et al*. 2007; Wu *et al*. 2008; Toh *et al*. 2007; Fukuda *et al*. 2006; Ungrin *et al*. 2008; Leclerc *et al*. 2004; Mori *et al*. 2008). There have also been spheroid co-culture works including co-culture of endothelial cells with fibroblasts and smooth muscle cells using hanging drops (Kelm and Fussenegger 2004; Korff *et al*. 2001; Kelm *et al*. 2005). Metastatic prostate cancer cell line PC-3 cells have been co-cultured with fibroblasts using the NASA rotary cell culture system (Ingram *et al*. 1997). Many of these techniques, however, suffer from problems such as efficiency of forming spheroids, long-term culture, control of spheroid size, and uniform distribution of small numbers of co-culture cell types across all spheroids. Here, we apply a microfluidic spheroid formation technology used previously to form embryoid bodies (Torisawa *et al*. 2007) to the formation of heterogeneous co-culture spheroids of PC-3's supported by osteoblasts and endothelial cells as a model of the niche microenvironment for prostate cancer metastasis to the bone.

2.2 Materials and Methods

2.2.1 General Cell Culture

The PC-3 prostate cancer cells originally isolated from vertebral metastases in prostate cancer patient were obtained from ATCC (Rockville, MD). PC-3 cells were

stably transfected via DsRed lentivirus (LG501, Biogenova, Rockville, MD) following manufacturer's protocol. After transfection cells were sorted by flow cytometry for the brightest 10% of the population. PC-3 cells that stably express the DsRed protein are denoted as PC-3^{DsRed} cells. PC-3^{DsRed} cells were compared to PC-3 cells for several passages and were shown to behave normally. PC-3^{DsRed} cells were cultured in T-25 flasks (Corning, Acton, MA) and maintained in complete media consisting of RPMI-1640 (61870; Gibco) supplemented with 10% (v/v) fetal bovine serum (FBS; 10082; Gibco), and 1% (v/v) penicillin-streptomycin (Invitrogen). The PC-3^{DsRed} cells were routinely passaged at 70-90% confluence.

Human umbilical vein endothelial cells (HUVECs, Lonza) passage number 2-6 were cultured in endothelial growth medium-2 (EGM-2, Lonza) in T-25 flasks. The HUVECs were collected by washing and detaching with 0.25% trypsin/EDTA (Invitrogen). The trypsin solution was neutralized with 10% FBS in DMEM (Invitrogen) and spun down with a centrifuge (ThermoForma, Marietta, OH) for 5 min at 4^{o}C and resuspended in EGM-2. The spin and resuspension in EGM-2 were repeated to ensure removal of trypsin.

MC3T3-E1 cells are pre-osteoblasts derived from murine calvarias. When treated with ascorbate, these cells express osteoblast-specific markers and are capable of producing a mineralized matrix (Franceschi and Iyer 1992; Franceschi *et al*. 1994). These cells were routinely maintained in α-MEM (Alpha Minimum Essential Medium; Gibco) supplemented with 15% (v/v) FBS, and 1% (v/v) penicillin-streptomycin.

Differentiation of MC3T3-E1 cells into osteoblasts was only induced when cultured as spheroids by addition of 50 μg/ml ascorbic acid. All cultures were maintained in a humidified incubator at 37^{o}C, 5% CO_2, and 100% humidity.

2.2.2 Fabrication of Microfluidic Devices and Cell Seeding

The microfluidic device consists of a two-layer poly(dimethylsiloxane) (PDMS) device with two microchannels separated by a semi-permeable polycarbonate membrane (Figure 2.1). The upper channel consists of 28 side-chambers and is a dead-end designed to facilitate cell capture, whereas the lower channel is continuous to allow for media perfusion. The semi-permeable polycarbonate membrane was 10 μm thick with 5 μm pores with low cellular attachment (TMP04700; Fisher). Spheroids are cultured on the upper channel while the lower channel contains cell culture media. The fabrication of the device is as previously described (Torisawa *et al*. 2007). The lower channel is 100 μm in height and 2 mm in width. The dimensions of each cuboidal shaped side-chamber in the upper channel are 200 x 200 x 200 μm, while the central microchannel cross sectional area is 200 μm in height and 50 μm in width.

Microchannel and membrane surfaces are treated with 1% w/v Pluronic F108 (BASF) overnight to be resistant to cell adhesion. Before seeding cells, co-culture media consisting of PC-3 complete growth media and 50 μg/ml ascorbic acid was introduced into the device and incubated for 1 hr. Pre-mixed heterogeneous cell suspensions at 1:50:50 PC-3^{DsRed}:HUVEC:MC3T3-E1 ratio were then introduced into the upper channel

using gravity-driven flow. Specifically, the tube connected to the outlet of the lower channel was lowered to approximately 15 cm below the inlet reservoir during the cell seeding process. Consequently, gravity resulted from this height difference between the reservoirs created a suction force through the lower channel that facilitates uniform seeding of a confluent monolayer of cells in the upper channel. The cells were cultured under static conditions with daily media exchange through the lower channel.

2.2.3 PC-3^{DsRed} Proliferation Tracking and Evaluation of Viability

Co-culture spheroids that formed in the microchannel were imaged by phase contrast microscopy as well as fluorescence microscopy (Nikon TE-300). The number of PC-3^{DsRed} cells within each spheroid was tracked by fluorescence everyday for a total of 7 days. On the last day (day 7) of culture, the spheroids were stained with calcein-AM (Invitrogen) to evaluate cellular viability. Calcein-AM dissolved in PBS to a final concentration of 1μg/ml was introduced into both the upper and lower channels and incubated for 30 min at 37^{o}C. Cross-sections of the co-culture spheroids were subsequently imaged by confocal microscopy.

2.2.4 Doubling Time Calculation

PC-3^{DsRed} doubling time calculation for the co-culture spheroids inside devices (3D co-culture in device) was calculated by first fitting an exponential-fit line through the average data points from the PC-3^{DsRed} proliferation graph (Figure 2.2e, average number

of PC-3^{DsRed} cells/spheroid vs. time). The equation obtained from the fit was $y = 3.1679(e^{0.0707t})$ with $r^2 = 0.9041$. We subsequently set $y = 6$ (two times the initial average of PC-3^{DsRed} cells per spheroid on day 1) and solved for t (for the time it takes for the initial number of PC-3^{DsRed} cells at day 1 to double). The final doubling time equals t – 24 (the time it takes for the PC-3^{DsRed} cells present at day 1 to double). The same method was used to calculate the doubling time of PC-3^{DsRed} co-culture spheroids cultured on 96 well plates (3D co-culture in dish).

For PC-3 doubling time calculation under 2D mono-culture in dish, 2D co-culture in dish, and 3D mono-culture in dish (non-adherent culture), the initial and final number of cells were counted and the doubling time was solved from the equation $N(t) = N(t_0)\ 2^{[(t-t0)/D]}$ where N(t) = number of cells at time t (final number of cells), $N(t_0)$ = number of cells at time t_o (initial number of cells), t = harvesting time, t_0 = plating time, $t-t_0$ = time the cells have had to grow, and D = doubling time. The doubling time is reported in hours.

2.2.5 Spheroid Size Measurements

The size of the co-culture spheroids formed within the microchannel was determined by measuring their diameters as previously described (Torisawa *et al*. 2007). Co-culture spheroids that formed in the microchannel were imaged by phase contrast microscopy as described above. The mean diameter (d) of the co-culture spheroids was determined using the following equation: $d = (a \times b)^{1/2}$, where a and b are orthogonal

diameters of the spheroid (Kelm *et al*. 2003). The average size of the co-culture spheroids was reported as mean diameter ± standard deviation.

2.2.6 2D Co-culture, 3D Mono-culture, and 3D Co-culture in Dish

For the 2D co-culture experiment, HUVEC and MC3T3-E1 cell suspensions were pre-mixed at a 1:1 ratio. The heterogeneous cell mixture of HUVEC and MC3T3-E1 cells (support cells) were subsequently plated as a confluent monolayer on a tissue culture dish. 24 hours later when HUVEC and MC3T3-E1 cells had already attached to the tissue culture dish, PC-3^{DsRed} cells were added on top of the confluent monolayer of support cells at a co-culture ratio of 1 PC-3^{DsRed} to 100 support cells. The cells were maintained in co-culture media consisting of PC-3 complete growth media and 50 μg/ml ascorbic acid. Culture media were changed daily as in our co-culture spheroid system. The 2D co-culture system was monitored everyday for a total of 6 days. On the last day of culture (day 6), live stain (calcein-AM dissolved in PBS to a final concentration of 1μg/ml) was performed to determine the viability of the PC-3^{DsRed} cells.

For the culture of PC-3 cells on non-adherent surface as a model for closely aggregated 3D mono-culture, PC-3 cells were seeded in ultra-low attachment 96-well plates (Corning Costar) at a density of 5000 cells/well. PC-3 cells were maintained in PC-3 complete growth media and monitored for a total of 5 days. On the last day of culture (day 5), live/dead stain (calcein-AM and ethidium homodimer-1 dissolved in PBS

to a final concentration of 1μg/ml) was performed to determine the viability of the PC-3^{DsRed} cells.

For the culture of PC-3^{DsRed} co-culture spheroids on non-adherent dish, pre-mixed heterogeneous cell suspensions at 1:50:50 PC-3^{DsRed}:HUVEC:MC3T3-E1 ratio were first formed into 30 μl hanging drops with ~500 cells/drop. After 1 day in culture when PC-3^{DsRed} co-culture spheroids were formed, each spheroid was then transferred to each well in a non-adherent 96-well plate. PC-3^{DsRed} co-culture spheroids were maintained in co-culture media consisting of PC-3 complete growth media and 50 μg/ml ascorbic acid and monitored over 7 days. Half of the total volume of culture media was exchanged by fresh media daily.

2.2.7 PC-3^{DsRed} $CD133^{+}$ Cell Sorting

PC-3^{DsRed} $CD133^{+}$ cells were isolated using CD133 Cell isolation kit, according to the manufacturer's protocol (Miltenyl Biotec). Briefly, cells were made into single cell suspension by using cellstripper (Mediatech, Inc., VA), washed with PBS and resuspended into MACS Buffer supplemented with 0.5% BSA. The cells were labeled with CD133 microbeads for 30 minutes after blocking Fc receptors with FcR Blocking reagent. After labeling, the cells were washed with MACS buffer. Magnetically labeled CD133 positive cells were passed through LS columns (Miltenyl Biotech). Cells were eluted with MACS buffer.

2.3 Results and Discussion

2.3.1 Formation of PC-3^{DsRed} Co-culture Spheroids within Microchannel (Spheroid Size, Media Exchange, Distribution of PC-3^{DsRed} Cells)

A schematic of the microfluidic device comprised of two microchannels separated by a semi-permeable membrane is shown in Figure 2.1a, b. The PC-3^{DsRed} co-culture spheroids form through a process shown in Figure 2.1c. Heterogeneous cell mixture of PC-3^{DsRed}, MC3T3, and HUVEC cells at 1:100 PC-3^{DsRed} to support cells ratio was introduced into the upper channel as a monolayer. Since the microchannel surfaces were rendered resistant to cell adhesion, the cells self-aggregated to form co-culture spheroids within 1 day in culture. Figure 2.1d shows the actual images of the co-culture spheroid formation process. Despite the dead-end upper channel, cells could still be introduced into the upper channel through gravity-driven seeding with suction from the lower channel through the semi-permeable membrane. Furthermore, due to the circular flow pattern inside the cuboidal-shaped side-chambers (Figure 2.1c), the cells preferentially settled into the side chambers and tended to aggregate into circular shapes during seeding. Such automatic formation of semi-aggregated cellular mass during the seeding process facilitated the subsequent spheroid formation. The sizes of the spheroids were relatively uniform and synchronous in their formation. The area of each side chamber as dictated by the microchannel size specification provided control of uniformly-sized spheroids. In our device, the area of each side chamber (200 μm by 200 μm) was 4 x 10^4 μm^2. Since the size of each cell was about 10 μm in height, the estimated volume of a confluent

monolayer of rounded, unattached cells in each chamber was approximately 4 x 10^5 μm^3. To achieve this volume, the estimated diameter of each spheroid would have to be 90 μm, which was approximately the size of the spheroids that we consistently obtained in our experiments (86 ± 12 μm). The microchannel size specifications can easily be adjusted to allow uniform spheroid formation of various other sizes (Torisawa *et al*. 2007). In addition, the compartmentalization afforded by the 5 μm semi-permeable polycarbonate membrane allowed convenient exchange of media from the bottom channel while non-attached spheroids were cultured on the top channel without perturbation of the spheroid positions and convective washout. The side-chamber design further introduced compartmentalization to keep co-culture spheroids stationary for easy continuous PC-3^{DsRed} cell tracking despite daily culture media exchange.

In order to track and monitor the small number of prostate cancer cells within co-culture spheroids, we used PC-3 cells stably transfected with the fluorescent protein DsRed (PC-3^{DsRed}). PC-3^{DsRed} cells were co-cultured with osteoblasts (MC3T3-E1), and endothelial cells (HUVEC) in the microfluidic device to mimic a "niche"-like microenvironment. The choice of support cells was based on the fact that PC-3 cells were first isolated from prostate cancer metastasis to the bone. Furthermore, it has been suggested that the process of prostate cancer metastasis to the bone is similar to the homing of HSC's to the bone marrow (Taichman *et al*. 2007; Shiozawa *et al*. 2008; 2010). Prostate cancer cells that successfully established metastasis at the bone marrow seem to parasitize the HSC niche and harvest the normal machinery from the niche microenvironment to facilitate growth and survival (Taichman *et al*. 2007; Shiozawa *et al*.

2008; 2010). To mimic this HSC niche for prostate cancer cell culture, we chose a co-culture cell ratio of 1:100 PC-3^{DsRed} to support cells, which had previously been shown to yield the best supporting niche microenvironment for HSC's (unpublished results). Figure 2.1e shows an image of PC-3^{DsRed} co-culture spheroid. The PC-3^{DsRed} cells were red while green represented live cells (calcein-AM live stain). The PC-3^{DsRed} cells were clearly distinguished from all the other support cells by its red fluorescence. The spatial arrangement of the PC-3^{DsRed} cells within the spheroid was relatively random, with PC-3^{DsRed} cells located everywhere throughout the spheroids. Our microfluidic device was able to ensure the incorporation of small numbers of PC-3^{DsRed} cells inside co-culture spheroids with intimate contact with the support cells. In addition, the distribution of PC-3^{DsRed}'s across all spheroids in the device was relatively uniform. Since 10,000 cells were introduced into the device that consists of 28 side-chambers, the initial number of cells in each chamber was about 350 cells/chamber. At the co-culture ratio of 1 PC-3^{DsRed} to 100 support cells, the theoretical number of PC-3^{DsRed}'s was 3.5 cells/chamber. This was in good agreement with the number we obtained in our experiments with an average of 3 ± 2 cells/spheroid on day 1 in culture. Except the three chambers at the dead-end of the device in which there were fewer cells seeded overall, PC-3^{DsRed} cells were uniformly distributed along the length of the device at the consistent co-culture ratio of 1 percent. Uniform distribution of the PC-3^{DsRed} cells across all co-culture spheroids allows for a consistent pool of 3D tissue samples for a wide variety of applications such as anti-cancer drug sensitivity testing experiments.

2.3.2 PC-3^{DsRed} Proliferation and Viability (2D vs. 3D, Co-culture vs. Mono-culture)

The PC-3^{DsRed} cells were tracked for their proliferation within each spheroid by their fluorescence everyday for a total of 7 days. The growth pattern and viability of the PC-3^{DsRed} cells within the 3D co-culture environment over the course of 1 week is shown in Figure 2.2. Figure 2.2a, b, c show the optical and fluorescent time-lapse images of PC-3^{DsRed} cells cultured within MC3T3 and HUVEC co-culture spheroids. In this particular co-culture spheroid, there was only one PC-3^{DsRed} cell on day 1 of culture, which gradually proliferated into two cells by day 4, and again doubled to four cells by day 7. This showed that PC-3^{DsRed} cells were still able to proliferate inside co-culture spheroids. PC-3^{DsRed} cells were still alive after 7 days in culture inside spheroids as shown in Figure 2.2d with a representative section of the PC-3^{DsRed} co-culture spheroid obtained using confocal microscopy. Live cells were stained with calcein-AM and appeared to be green while PC-3^{DsRed} cells expressed red fluorescence. Since all the red cells co-localize with the viable green color, all the PC-3^{DsRed} cells were able to survive under the 3D co-culture environment after 7 days in culture. Together, these results demonstrated that PC-3^{DsRed} cells were able to survive and proliferate inside osteoblast and endothelial cell co-culture spheroids. As shown in Figure 2.2e, PC-3^{DsRed}'s mainly remained quiescent and proliferated at a relatively slow rate in 3D co-culture environment. PC-3^{DsRed} cells merely proliferated from an average of 3 cells/spheroid to an average of 5 cells/spheroid. The doubling time of the PC-3^{DsRed} cells under the 3D co-culture environment was estimated to be 212 h (about 9 days, Table 2.1). Such proliferation rate of PC-3^{DsRed} cells inside spheroids is much slower than the conventional 2D mono-culture (doubling time ≈ 24 h, Table 2.1). Although the *in vivo* metastatic prostate cancer cell proliferation rate is

not exactly known, we believe that our prostate cancer cell co-culture spheroid system mimicking the *in vivo* prostate cancer cell niche microenvironment more faithfully recapitulated a reasonable physiologic growth pattern of prostate cancer cells *in vitro*. The *in vivo* doubling time of PC-3 cells was roughly determined to be between 1 to 2 weeks from various PC-3 *in vivo* culture experiments (Nakanishi *et al*. 2003; Singh *et al*. 2004; Li *et al*. 2008), which was in good agreement with the observed PC-3^{DsRed} doubling time in our *in vitro* microfluidic 3D spheroid co-culture system.

Since we have previously demonstrated that cells can be cultured normally inside a membrane-type device (Torisawa *et al*. 2007; Huh *et al*. 2007), the device should not affect cellular proliferation. We cultured PC-3^{DsRed} co-culture spheroids on non-adherent dishes to confirm their proliferation behavior. Proliferation rate of PC-3^{DsRed} cells cultured on non-adherent dishes (doubling time ≈ 205 hrs, Table 2.1) was very similar to that cultured inside devices. Since a hanging drop method is difficult to culture spheroids for a week because of difficulty of changing culture media, and also non-adherent dish culture is difficult to monitor each spheroid because of aggregation of spheroids, spheroids were made by the hanging drop method and each spheroid was then transferred to each well in a non-adherent 96-well plate. The fact that the PC-3^{DsRed} cells proliferated at a considerably slower rate inside the co-culture spheroids was not device-dependent. Rather, the proliferation of cells inside these two-layer semi-permeable membrane devices seem to be cell type-dependent as other cell types cultured under both 2D and 3D conditions were still able to proliferate inside the devices.

We compared PC-3^{DsRed} proliferation in our co-culture spheroid system to 2D co-culture in dishes. PC-3^{DsRed}, HUVEC and MC3T3-E1 cells were co-cultured under 2D dish environment at 1:100 PC-3^{DsRed} to support cells ratio and PC-3^{DsRed} proliferation was monitored everyday for a total of 6 days. On day 1 of culture, there were very few PC-3^{DsRed} cells present (Figure 2.3a, b). But by day 6, it was clear that the PC-3^{DsRed} cells had proliferated extensively (Figure 2.3e, f), with an estimated doubling time of ≈ 29 hrs (Table 2.1). Furthermore, viability experiments confirmed that most of these actively proliferating PC-3^{DsRed} cells were still alive on day 6 (data not shown). These results demonstrated that the complex interplay of various soluble factors involved in prostate cancer and support cells co-culture was not enough to mimic the physiologic microenvironment. This finding also implied that mere cell-cell interaction in a 2D context between PC-3^{DsRed} cells and support cells was not sufficient to recapitulate a physiologic proliferation rate of the prostate cancer cells. Therefore, a physiologic microenvironment not only involves cell-cell interaction, but 3D environment is also a critical factor.

We also compared PC-3^{DsRed} 3D co-culture spheroid inside the device to PC-3^{DsRed} 3D mono-culture inside the same device. Instead of introducing heterogeneous mixture of the co-culture cells into the device, pure PC-3^{DsRed} cells were seeded. PC-3^{DsRed} cells did not form spheroids but quickly aggregated into cell clusters within one day of culture. Over 7 days of culture, it was clear that the PC-3^{DsRed} cells proliferated under such 3D mono-culture environment inside the device (data not shown). However, because it is difficult to quantify the number of PC-3^{DsRed} cells inside the device, we

estimated the PC-3^{DsRed} doubling time under 3D mono-culture condition by investigating the effect of blocking cell-substrate attachment on PC-3 cells. Initially, PC-3 cells were seeded in ultra-low attachment 96-well plates at a density of 5000 cells/well. PC-3 cells quickly aggregated into cell clusters of various sizes within 1 day in culture (Figure 2.3g), but they did not form spheroids. Nevertheless, such close-packed, non-adherent culture condition resembled PC-3 3D mono-culture in dish. Over the 5 days of culture, PC-3 cells still proliferated at a comparative rate (doubling time ≈ 36 h, Table 2.1) as the normal 2D mono-culture condition (Figure 2.3h). In addition, almost all PC-3 cells were still alive after 5 days in culture as demonstrated by live/dead stain (Figure 2.3i). This showed that PC-3 mono-culture under such closely-aggregated 3D-like environment was still not sufficient in recapitulating a more physiological growth rate of prostate cancer cells. Various PC-3-support cells interaction may be imperative in inducing the more physiological proliferation of PC-3^{DsRed} cells under the 3D co-culture spheroid condition. One other interesting characteristic of our co-culture spheroids was that the support cell did not seem to be proliferating. This was a desired characteristic as the endothelial cells and osteoblasts mainly function to support the PC-3^{DsRed} cells without depleting the nutrients in the microenvironment.

In summary, under normal 2D mono-cultures, PC-3^{DsRed}, HUVEC, and MC3T3-E1 cells all proliferated at a relatively fast rate. When grown as 3D mono-cultures, PC-3^{DsRed}, HUVEC, and MC3T3-E1 cells proliferated, died, and stayed relatively quiescent, respectively. When all three cell types are co-cultured in 2D, there seemed to be proliferation of all three cell types. But interestingly, co-culture of all three cell types in

3D seemed to be no death of the HUVECs, quiescence of the MC3T3-E1 cells, and slow proliferation of the PC-3^{DsRed} cells. These non-additive synergistic effects of co-culture contributed to a stable co-culture system, which contrasts with rapid proliferation of PC-3 cell mono-cultures in 2D and 3D, with the rapid proliferation in 2D but death of 3D spheroids of endothelial cell mono-cultures, and with rapid proliferation in 2D but slow growth of 3D spheroids of osteoblasts. Such cellular behavior may be a combination of effects from various soluble and insoluble factors, direct heterotypic cell-cell interactions between PC-3^{DsRed} and support cells in a semi-confined 3D context, and the unique extracellular matrix (ECM) composition contributed by all co-culture cell types leading to various proliferation inhibitory and survival effects through integrin signaling. Various other co-culture examples also exhibit promoting effects from support cells as well as synergistic cross-talk between co-culture cell types (Camps *et al*. 1990; Korff *et al*. 2001; Kelm *et al*. 2005). The results highlight the importance of culturing cells not only in 3D but also with appropriate co-culture of cells.

2.3.3 $CD133^+$ PC-3^{DsRed} Co-culture Spheroids

CD133 is a potential marker for prostate cancer stem cell (CSC), and therefore the $CD133^+$ population is believed to be enriched for CSCs. The 3D co-culture spheroid system was therefore also applied to $CD133^+$ PC-3^{DsRed} cells. Figure 2.4a, b, c shows the time-lapse images of $CD133^+$ PC-3^{DsRed} cell co-culture spheroids with MC3T3-E1 and HUVEC at 1:100 $CD133^+$ PC-3^{DsRed} cells to support cells ratio. In this particular co-culture spheroid, the only $CD133^+$ PC-3^{DsRed} cell present on day 1 (Figure 2.4a) did not

proliferate inside the spheroid throughout the 7 days of culture (Figure 2.4b, c). The same cell was kept alive but quiescent inside the spheroid for a week. Figure 2.4d shows the graph of the overall $CD133^+$ PC-3^{DsRed} cell proliferation pattern inside co-culture spheroids over 7 days. There seemed to be a slight decreasing trend in the average number of $CD133^+$ PC-3^{DsRed} cells per spheroid over the first 4 days. This might be due to the fact that a greater number of cells were dying in the first few days as these $CD133^+$ PC-3^{DsRed} cells might have been stressed more during the sorting process. The remaining viable cells seemed to stay quiescent or start to proliferate slowly. The greater variability in the $CD133^+$ PC-3^{DsRed} cell proliferation and survival between different spheroids also explains the larger standard deviation seen on day 4 and day 7 of culture. Overall, the $CD133^+$ PC-3^{DsRed} cells cultured inside co-culture spheroids supported by HUVEC and MC3T3-E1 cells were able to survive but did not proliferate much over the course of 1 week.

Under traditional 2D mono-culture condition, these $CD133^+$ PC-3^{DsRed} cells can easily differentiate to loose their cell surface marker. In our 3D co-culture spheroid system, the $CD133^+$ PC-3^{DsRed} cells remained mostly quiescent without much proliferation. Further experiments are needed to characterize in more detail the survival, proliferation, and the maintenance of the CD133 marker in these cells. The type and ratio of supporting cells used may also be critical for maintaining the cell surface marker of these cells. Nevertheless, our system demonstrated a unique culture method that may be able to capture the $CD133^+$ population of PC-3's at the quiescent stage. Such model would be suitable for the development of anti-cancer drugs that target CSCs. As

mentioned earlier, new therapeutics that specifically target CSCs are much needed, but currently it has been extremely difficult to maintain and culture CSCs *in vitro*. Our microfluidic 3D co-culture spheroids system efficiently provides physiologic 3D prostate cancer and CSC tissue constructs as models for anti-cancer drug sensitivity testing on the general tumor population as well as CSCs.

2.4 Conclusion

We describe the design and fabrication of a platform for efficient microfluidic 3D co-culture of metastatic prostate cancer cells within a "niche"-like construct. In addition to promoting reliable formation of uniformly-sized spheroids, our system also ensures uniform distribution of the small number of PC-3 cells as well as the other co-culture cell types across all spheroids within the device. In addition, the side-chamber microchannel design keeps the spheroids stationary during media exchange for easy tracking of the PC-3's during extended longer term cultures. Using these capabilities, we created 3D cancer "niche"-like microenvironments with high cell viability and a more physiological slower growth behavior of prostate cancer cells. The microscale 3D tumor tissue constructs may be valuable as a model for testing drugs that target the cancer microenvironment as well as the cancer cells themselves in their more quiescent state in the niche. Although this paper focused on prostate cancer cells and their niche, the technology described is versatile and should be readily applicable for culture of various other types of cells in a physiological 3D setting.

Figure 2.1. Schematic illustrations of the microfluidic spheroid formation device design **(a)** to **(b)** and PC-3^{DsRed} co-culture spheroid formation process **(c)**. The device consists of two PDMS microchannels separated by a semi-permeable polycarbonate membrane with 5 μm pores. The upper channel is a dead end channel with 28 side-chambers to culture spheroids, and the lower channel has flow through capability for culture medium. Before seeding cells, the channel and membrane surfaces are rendered resistant to cell adhesion. The heterogeneous mixture of PC-3^{DsRed} and support cells (MC3T3-E1 and HUVEC) at 1:100 co-culture ratio are introduced into the upper channel as a confluent monolayer. The cells preferentially settle inside the side-chambers and self-aggregate to form PC-3^{DsRed} co-culture spheroids within 1 day of culture. **(d)** Actual time-lapse images of PC-3^{DsRed} co-culture spheroid formation within microchannel (side-chambers: 200 x 200 x 200 μm, central microchannel: 50 μm width, 200 μm height). Optical images were taken immediately after seeding and 1 day after introducing the cells. **(e)** Optical and fluorescent images of a PC-3^{DsRed} co-culture spheroid after 1 day of cultlure in the microfluidic device. Red = PC-3^{DsRed} cells, Green = MC3T3 and HUVEC (support cells). Scale bar is 200 μm.

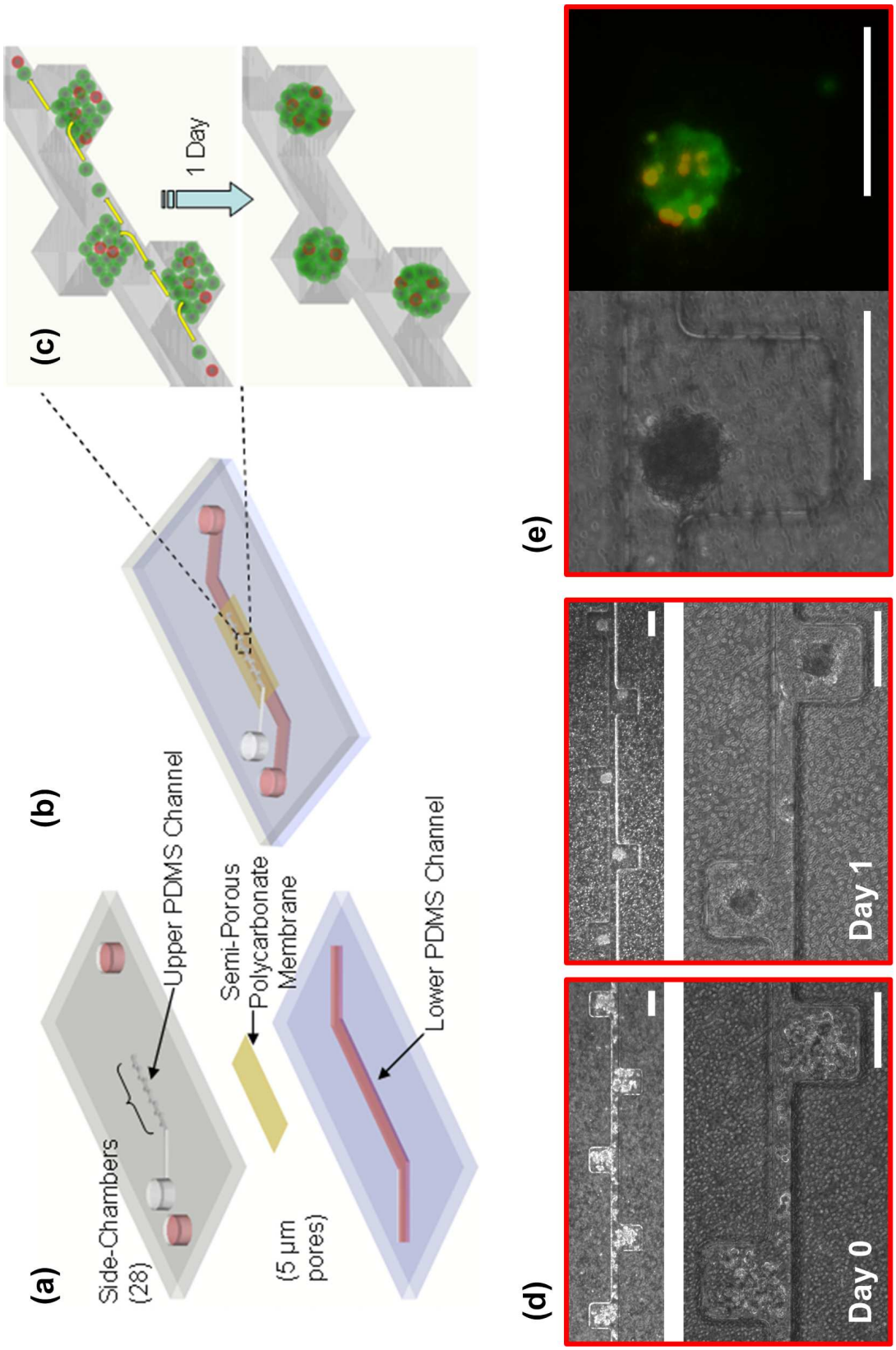
(a)
Side-Chambers
(28)
Upper PDMS Channel
Semi-Porous
Polycarbonate
Membrane
(5 µm
pores)
Lower PDMS Channel
(b)
(c)
1 Day
(d)
Day 0
Day 1
(e)

Figure 2.1

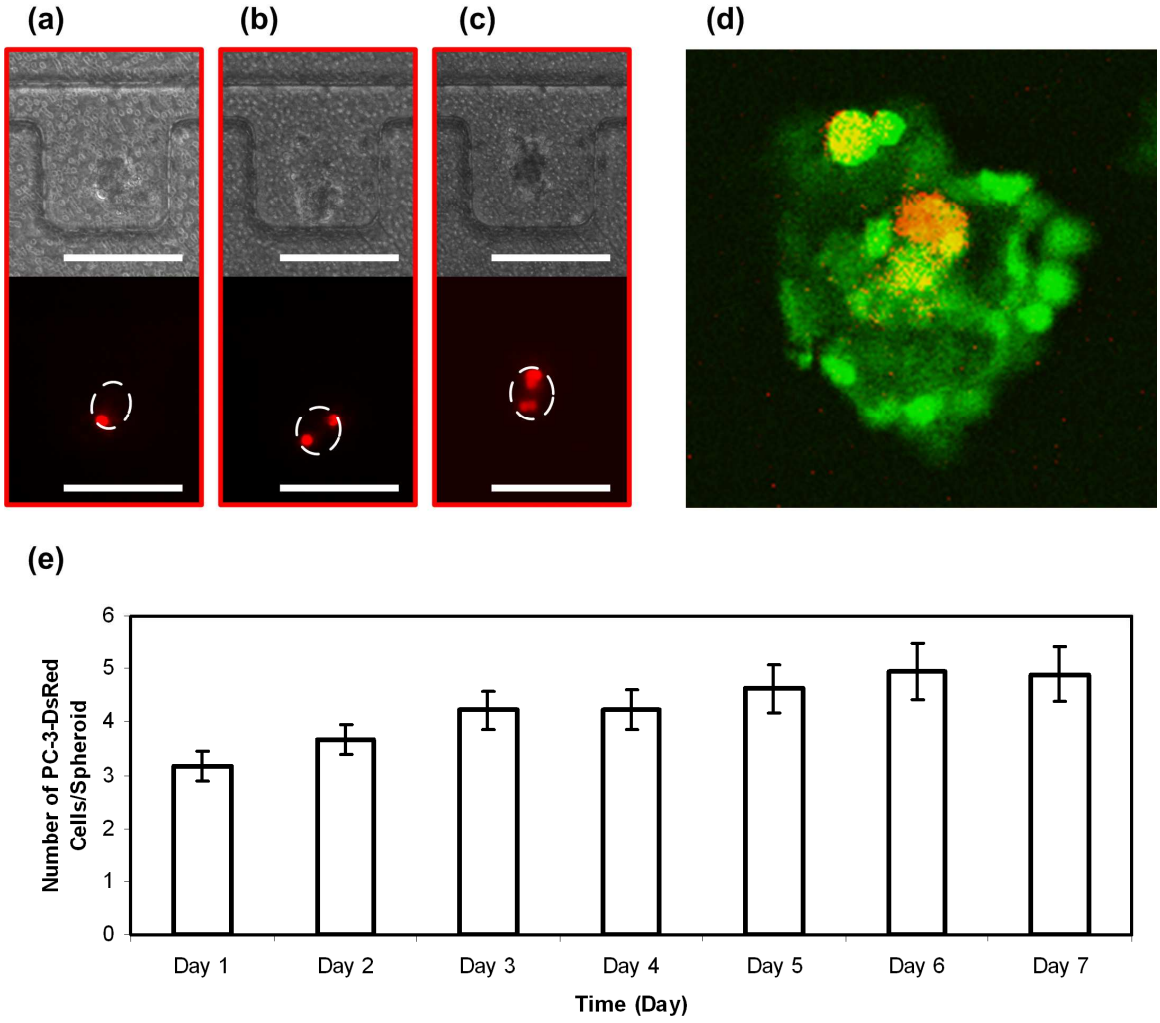

Figure 2.2. Time-lapse images of PC-3^{DsRed} cell proliferation within HUVEC and MC3T3-E1 co-culture spheroid in side-chambers of the microfluidic device. Optical images of the co-culture spheroids and fluorescent images of PC-3^{DsRed} cells on day 1 **(a)**, day 4 **(b)**, and day 7 **(c)** of culture. **(d)** A confocal section of PC-3^{DsRed} co-culture spheroid illustrating the viability of PC-3^{DsRed} cells. Red = PC-3^{DsRed} cells, Green = Live cells (Calcein-AM stain), Yellow = Live PC-3^{DsRed} cells. **(e)** Graph of PC-3^{DsRed} proliferation pattern inside co-culture spheroids over a course of 1 week. Y-axis shows the average number of PC-3^{DsRed} cells per spheroid (error bars are standard error), x-axis is the time in days. Scale bar is 200 μm.

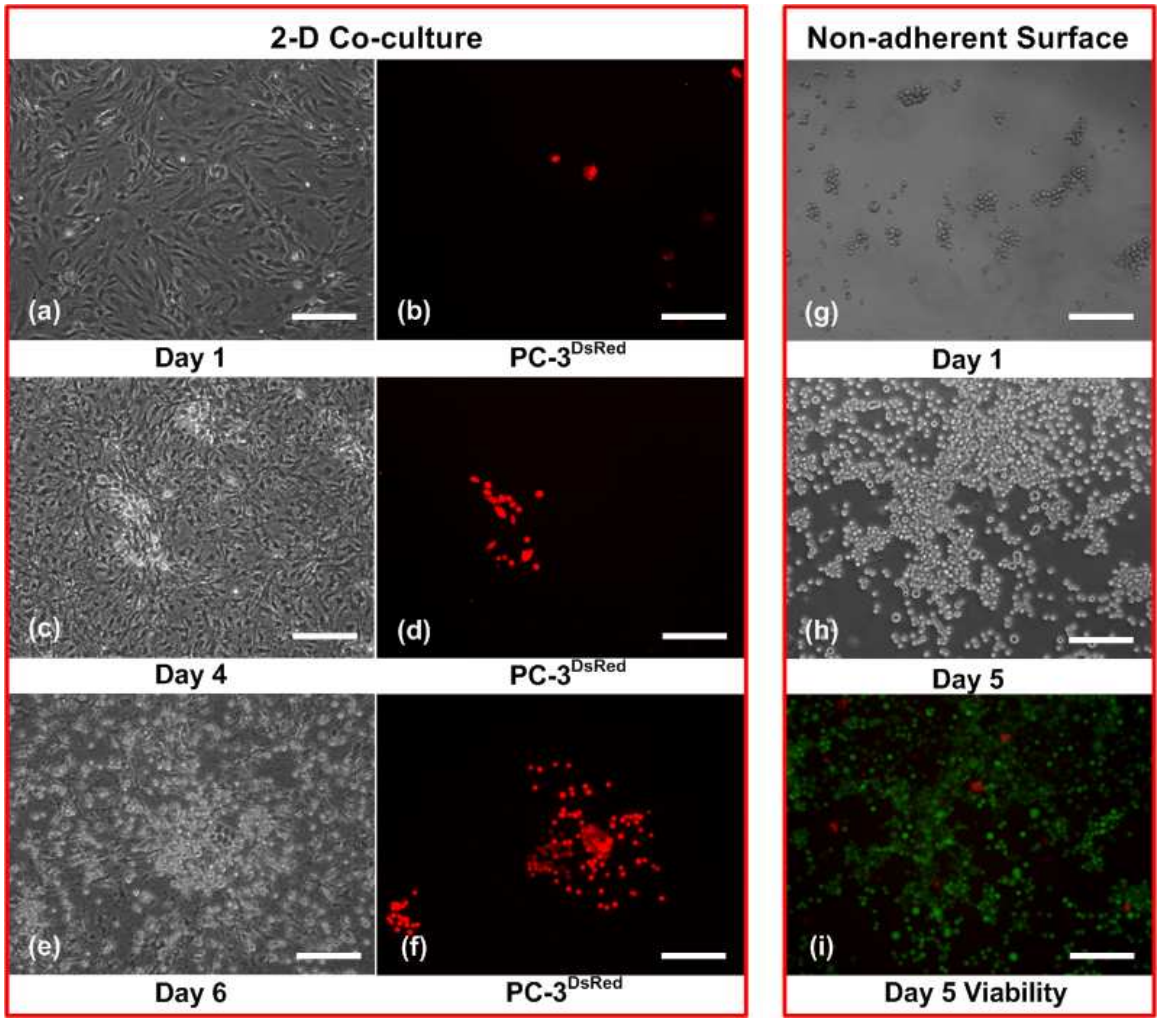

Figure 2.3. Time-lapse images of PC-3^{DsRed} proliferation under 2D co-culture with MC3T3-E1 and HUVEC **(a)** to **(f)**. Red = PC-3^{DsRed} cells. Time-lapse images of PC-3 proliferation on non-adherent surface **(g)** and **(h)** and day 5 viability **(i)**. Red = dead cells, Green = live cells. Scale bar is 200 μm.

Figure 2.4. Time-lapse images of PC-3^{DsRed} CD133^{+} cell proliferation within HUVEC and MC3T3-E1 co-culture spheroid in side-chambers of the microfluidic device. Optical images of the co-culture spheroids and fluorescent images of PC-3^{DsRed} CD133^{+} cells on day 1 **(a)**, day 4 **(b)**, and day 7 **(c)** of culture. **(d)** Graph of PC-3^{DsRed} CD133^{+} cell proliferation pattern inside co-culture spheroids over a course of 1 week. Y-axis shows the average number of PC-3^{DsRed} CD133^{+} cells per spheroid (error bars are standard error), x-axis is the time in days. Scale bar is 200 μm.

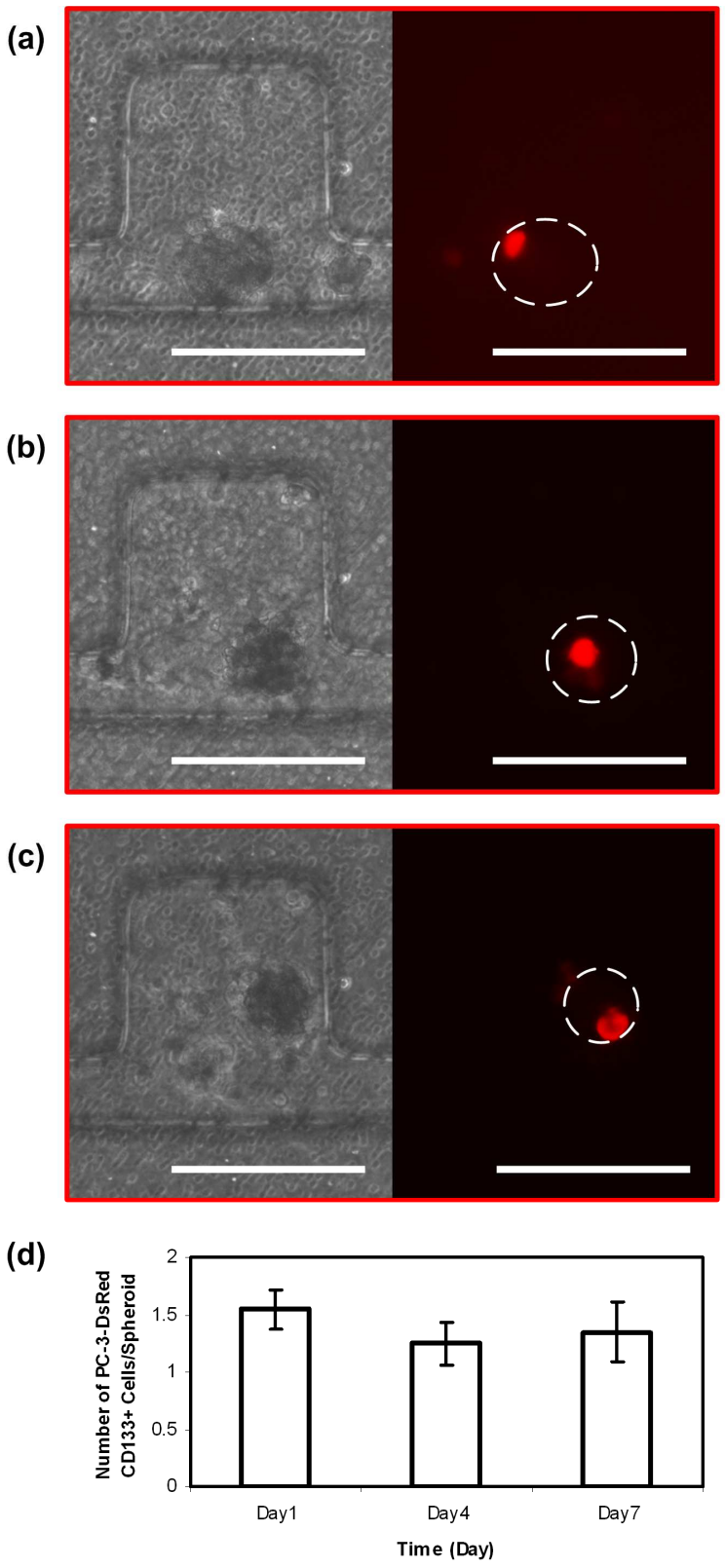
(a)
(b)
(c)
(d)
Number of PC-3-DsRed CD133+ Cells/Spheroid
2
1.5
1
0.5
0
Day1
Day4
Day7
Time (Day)

Figure 2.4

PC-3^{DsRed} Doubling Time Under Various Conditions				
2D Mono-culture (Dish)	**2D** Co-culture (Dish)	**3D** Mono-culture (Dish)	**3D** Co-culture (Dish)	**3D** Co-culture (Device)
24 hrs	29 hrs	36 hrs	205 hrs	212 hrs

Table 2.1. Summary of PC-3^{DsRed} doubling time under different culturing conditions

2.5 References

1. Abbott A. Cell culture: biology's new dimension. Nature 2003;424(6951):870-2.

2. Barrett JM, Mangold KA, Jilling T, Kaul KL. Bi-directional interactions of prostate cancer cells and bone marrow endothelial cells in three-dimensional culture. Prostate 2005;64(1):75-82.

3. Camps JL, Chang SM, Hsu TC, Freeman MR, Hong SJ, Zhau HE, et al. Fibroblast-mediated acceleration of human epithelial tumor growth in vivo. Proc Natl Acad Sci USA 1990;87(1):75-9.

4. Croker AK, Allan AL. Cancer stem cells: implications for the progression and treatment of metastatic disease. J Cell Mol Med 2008;12(2):374-90.

5. Dontu G, Liu S, Wicha MS. Stem cells in mammary development and carcinogenesis: implications for prevention and treatment. Stem Cell Rev 2005;1(3):207-13.

6. Franceschi RT, Iyer BS. Relationship between collagen synthesis and expression of the osteoblast phenotype in MC3T3-E1 cells. J Bone Miner Res 1992;7(2):235-46.

7. Franceschi RT, Iyer BS, Chi Y. Effects of ascorbic acid on collagen matrix formation and osteoblast differentiation in murine MC3T3-E1 cells. J Bone Miner Res 1994;9(6):843-54.

8. Friedrich J, Ebner R, Kunz-Schughart LA. Experimental anti-tumor therapy in 3-D: spheroids-old hat or new challenge. Int J Radiat Biol 2007;83(11-12):849-71.

9. Fukuda J, Khademhosseini A, Yeo Y, Yang X, Yeh J, Eng G, et al. Micromolding of photocrosslinkable chitosan hydrogel for spheroid microarray and co-cultures. Biomaterials 2006;27(30):5259-67.

10. Griffith LG, Swartz MA. Capturing complex 3D tissue physiology in vitro. Nat Rev Mol Cell Biol 2006;7(3):211-24.

11. Hotary KB, Allen ED, Brooks PC, Datta NS, Long MW, Weiss SJ. Membrane type I matrix metalloproteinase usurps tumor growth control imposed by the three-dimensional extracellular matrix. Cell 2003;114(1):33-45.

12. Huh D, Fujioka H, Tung YC, Futai N, Paine R III, Grotberg JB, et al. Acoustically detectable cellular-level lung injury induced by fluid mechanical stresses in microfluidic airway systems. Proc Natl Acad Sci USA 2007;104(48):18886-91.

13. Ingram M, Techy GB, Saroufeem R, Yazan O, Narayan KS, Goodwin T J, et al. Three-dimensional growth patterns of various human tumor cell lines in simulated

microgravity of a NASA bioreactor. In Vitro Cell Dev Biol Anim 1997;33(6):459-66.

14. Kelly K, Yin JJ. Prostate cancer and metastasis initiating stem cells. Cell Res 2008;18(5):528-37.

15. Kelm JM, Fussenegger M. Microscale tissue engineering using gravity-enforced cell assembly. Trends Biotechnol 2004;22(4):195-202.

16. Kelm JM, Sanchez-Bustamante CD, Ehler E, Hoerstrup SP, Djonov V, Ittner L, et al. VEGF profiling and angiogenesis in human microtissues. J Biotechnol 2005;118(2):213-29.

17. Kelm JM, Timmins NE, Brown CJ, Fussenegger M, Nielsen LK. Method for generation of homogeneous multicellular tumor spheroids applicable to a wide variety of cell types. Biotechnol Bioeng 2003;83(2):173-80.

18. Klob D, Fischer M, Rothermel A, Simon JC, Robitzki AA. Drug testing on 3D in vitro tissues trapped on a microcavity chip. Lab Chip 2008;8(6):879-84.

19. Korff T, Kimmina S, Martiny-Baron G, Augustin HG. Blood vessel maturation in a 3-dimensional spheroidal coculture model: direct contact with smooth muscle cells regulates endothelial cell quiescence and abrogates VEGF responsiveness. FASEB J 2001;15(2):447-57.

20. Kunz-Schughart LA, Freyer JP, Hofstaedter F, Ebner R. The use of 3-D cultures for high-throughput screening: the multicellular spheroid model. J Biomol Screen 2004;9(4):273-85.

21. Leclerc E, Sakai Y, Fujii T. Microfluidic PDMS (polydimethylsiloxane) bioreactor for large-scale culture of hepatocytes. Biotechnol Prog 2004;20(3):750-5.

22. Li F, Tiede B, Massague J, Kang Y. Beyond tumorigenesis: cancer stem cells in metastasis. Cell Res 2007;17(1):3-14.

23. Li L, Neaves WB. Normal stem cells and cancer stem cells: the niche matters. Cancer Res 2006;66(9):4553-7.

24. Li Y, Li CX, Ye H, Chen F, Melamed J, Yi P, et al. Decrease in stromal androgen receptor associates with androgen-independent disease and promotes prostate cancer cell proliferation and invasion. J Cell Mol Med 2008;12(6B):2790-8.

25. Lin RZ, Chang HY. Recent advances in three-dimensional multicellular spheroid culture for biomedical research. Biotechnol J 2008;3(9-10):1172-84.

26. Mori R, Sakai Y, Nakazawa K. Micropatterned organoid culture of rat hepatocytes and HepG2 cells J Biosci Bioeng 2008;106(3):237-42.

27. Mueller-Klieser W. Three-dimensional cell cultures: from molecular mechanisms to clinical applications. Am J Physiol 1997;273(4 Pt 1):C1109-23.

28. Nakanishi H, Mazda O, Satoh E, Asada H, Morioka H, Kishida T, et al. Nonviral genetic transfer of Fas ligand induced significant growth suppression and apoptotic tumor cell death in prostate cancer in vivo. Gene Ther 2003;10(5):434-42.

29. Singh AV, Xiao D, Lew KL, Dhir R, Singh SV. Sulforaphane induces caspase-mediated apoptosis in cultured PC-3 human prostate cancer cells and retards growth of PC-3 xenografts in vivo. Carcinogenesis 2004;25(1):83-90.

30. Shiozawa Y, Havens AM, Jung Y, Ziegler AM, Pedersen EA, Wang J, et al. Annexin II/Annexin II receptor axis regulates adhesion, migration, homing, and growth of prostate cancer. J Cell Biochem 2008;105(2):370-80.

31. Shiozawa Y, Havens AM, Pienta KJ, Taichman RS. The bone marrow niche: habitat to hematopoietic and mesenchymal stem cells, and unwitting host to molecular parasites. Leukemia 2008;22(5):941-50.

32. Shiozawa Y, Pedersen EA, Patel LR, Ziegler AM, Havens AM, Jung Y, et al. GAS6/AXL axis regulates prostate cancer invasion, proliferation, and survival in the bone marrow niche. Neoplasia 2010;12(2):116-27.

33. Sun YX, Fang M, Wang J, Cooper CR, Pienta KJ, Taichman RS. Expression and activation of $\alpha_v\beta_3$ integrins by SDF-1/CXC12 increases the aggressiveness of prostate cancer cells. Prostate 2007;67(1):61-73.

34. Taichman RS, Loberg RD, Mehra R, Pienta KJ. The evolving biology and treatment of prostate cancer. J Clin Invest 2007;117(9):2351-61.

35. Toh YC, Zhang C, Zhang, J, Khong YM, Chang S, Samper VD, et al. A novel 3D mammalian cell perfusion-culture system in microfluidic channels. Lab Chip 2007;7(3):302-9.

36. Torisawa Y, Chueh BH, Huh D, Ramamurthy P, Roth TM, Barald KF, et al. Efficient synchronous formation of uniform-sized embryoid bodies using a compartmentalized microchannel device. Lab Chip 2007;7(6):770-6.

37. Torisawa Y, Takagi A, Nahimoto Y, Yasukawa T, Shiku H, Matsue T. A multicellular spheroid array to realize spheroid formation, culture, and viability assay on a chip. Biomaterials 2007;28(3):559-66.

38. Torisawa Y, Takagi A, Shiku H, Yasukawa T, Matsue T. A multicelluar spheroid-based drug sensitivity test by scanning electrochemical microscopy. Oncol Rep 2005;13(6):1107-12.

39. Ungrin MD, Joshi C, Nica A, Bauwens C, Zandstra PW. Reproducible, ultra high-throughput formation of multicellular organization from single cell suspension-derived human embryonic stem cell aggregates. PLoS ONE 2008;3(2):e1565.

40. Wu LY, DiCarlo D, Lee LP. Microfluidic self-assembly of tumor spheroids for anticancer drug discovery. Biomed Microdev 2008;10(2):197-202.

41. Yamada KM, Cukierman E. Modeling tissue morphogenesis and cancer in 3D. Cell 2007;130(4):601-10.

42. Yang J, Fizazi K, Peleg S, Sikes CR, Raymond AK, Jamal N, et al. Prostate cancer cells induce osteoblast differentiation through a Cbfa1-dependent pathway. Cancer Res 2001;61(14):5652-9.

CHAPTER 3

High-throughput 3D Spheroid Culture and Drug Testing Using a 384 Hanging Drop Array

Culture of cells as three-dimensional (3D) aggregates can enhance *in vitro* tests for basic biological research as well as for therapeutics development. Such 3D culture models, however, are often more complicated, cumbersome, and expensive than two-dimensional (2D) cultures. This chapter describes a 384-well format hanging drop culture plate that makes spheroid formation, culture, and subsequent drug testing on the obtained 3D cellular constructs as straightforward to perform and adapt to existing high-throughput screening (HTS) instruments as conventional 2D cultures. Using this platform, we show that drugs with different modes of action produce distinct responses in the physiological 3D cell spheroids compared to conventional 2D cell monolayers. Specifically, the anti-cancer drug 5-fluorouracil (5-FU) has higher anti-proliferative effects on 2D cultures whereas the hypoxia activated drug commonly referred to as tirapazamine (TPZ) are more effective against 3D cultures. The multiplexed 3D hanging drop culture and testing plate provides an efficient way to obtain biological insights that are often lost in 2D platforms.

3.1 Introduction

Three-dimensional (3D) cell culture is motivated by the need to work with cellular models that better mimic physiological tissues. Cellular functions and responses that are present in tissues are often lost in conventional 'dish'-based two-dimensional (2D) cell cultures limiting predictive capability of drug assays and skewing cell biological research results (Pampaloni *et al*. 2007). Consequently, many researches have been devoted to develop *in vivo*-like 3D cell culture techniques. Spheroid formation is one of the most well characterized models for 3D culture and screening due to its simplicity, reproducibility, and similarity to physiological tissues compared to other methods involving extracellular matrix (ECM) scaffolds and hydrogel systems (Friedrich *et al*. 2009; Kunz-Schughart *et al*. 2004). Spheroids are self-assembled spherical clusters of cell colonies cultured in environments where cell-cell interactions dominate over cell-substrate interactions, and they naturally mimic avascular tumors with inherent metabolic (oxygen) and proliferative (nutrient) gradients (Friedrich *et al*. 2009; Kunz-Schughart *et al*. 2004). Therefore, spheroids serve as excellent physiologic tumor models known to provide more reliable and meaningful therapeutic readouts compared to 2D tests (Kunz-Schughart *et al*. 2004). Spheroids allow cellular self-organization of appropriate 3D ECM assembly with complex cell-matrix and cell-cell interactions that mimic functional properties of the corresponding tissue *in vivo* (Friedrich *et al*. 2009). Most importantly, spheroids can be monitored easily for practical daily observations. As a result, spheroid cultures have been valued as a physiologically relevant alternative to 2D cultures for decades (Ivascu and Kubbies 2006; Del Duca *et al*. 2004; Friedrich *et al*. 2007).

Although these advantages of spheroids have been widely recognized, it has been difficult to scale up spheroid culture in a high-throughput manner for screening and testing. Typical spheroid formation methods include hanging drops on the underside of culture plate lids, culture of cells on non-adherent surfaces, spinner flask cultures, and rotary cell culture systems (Friedrich *et al*. 2007). These traditional spheroid formation and culture systems, however, are often tedious, low-throughput, hard to handle, and produce variable size spheroids. Recently, various microfluidic (spheroids on a chip) devices have also been developed (Torisawa *et al*. 2007; Sakai and Nakazawa 2007; Ungrin *et al*. 2008; Lee *et al*. 2010; Torisawa *et al*. 2007; Wu *et al*. 2008; Toh *et al*. 2007; Fukuda *et al*. 2006) to increase spheroid formation efficiency, offer better control of spheroid sizes, as well as simplify handling procedures. Many of these techniques, however, still suffer from problems such as long-term culture and device compatibility with drugs. Most importantly, these techniques are often not compatible with existing liquid handling robots for performing high-throughput screening (HTS). In this chapter, we describe a 384-well format spheroid culture plate based on the scientifically proven but traditionally tedious hanging drop method. The developed hanging drop array platform allows for efficient formation of uniformly-sized spheroids, their long-term culture, and drug testing using existing HTS instruments (e.g. liquid handling robots and plate readers) (Figure 3.1d). Utilizing this platform, we show that drugs with different modes of action produce distinct responses in the physiological 3D cell spheroids compared to conventional 2D cell monolayers.

3.2 Materials and Methods

3.2.1 Plate Design, Fabrication, and Hanging Drop Formation

The hanging drop array plate is made of polystyrene, and fabricated by injection molding. To overcome the drawback in liquid handling and substrate inversion of the conventional hanging drop method, each cell culture site has an access hole (diameter = 1.6 mm) through the substrate with a plateau on the bottom surface (diameter = 3mm, height = 0.5 mm) (Figure 3.1a). These cell culture sites are arranged in the standard 384-well plate format (16 rows, 24 columns, and 4.5 mm apart in both directions as shown in Figure 3.1b). To alleviate the commonly encountered evaporation problem with the small volume hanging drops (tens of μl), a water reservoir is constructed around the periphery of the culture sites (Figure 3.1a, b, e).

Prior to usage, a hydrophilic coating (0.1%, Pluronic F108, BASF Co., Ludwigshafen, Germany) is applied onto the entire plate surface. The plate is subsequently UV sterilized before cell seeding. To form hanging drops, cell suspension solution is pipetted from the top side through the access holes with the end of each pipette tip inserted into the access hole to guide the sample liquid to the bottom surface (Figure 3.1c). The liquid or cell samples can also be removed from the drop through the access holes using pipettes or slot pins (V&P Scientific, Inc., San Diego, CA). The size of the hanging drop is confined by the diameter of the plateau on the bottom surface.

3.2.2 General Cell Culture

To investigate the stability of long-term hanging drop spheroid culture using the designed array plate, osmolality measurements were performed while culturing three types of cells: African green monkey kidney fibroblast cell (COS7), murine embryonic stem (mES) cell (ES-D3), and human epithelial carcinoma cell that stably express mesothelin (A431.H9) cell (Ho *et al*. 2005). Prior to performing hanging drop culture using the plate, ES-D3 cells were cultured in dishes coated with 0.1% w/v porcine gel (Sigma-Aldrich Co.) and maintained in medium consisting of Dulbecco's Modified Eagle's Medium (DMEM) (Gibco 11960, Invitrogen Co., Carlsbad, CA) with 15% v/v fetal bovine serum (FBS) (Gibco 10082, Invitrogen Co.), 4 mM L-glutamin (Invitrogen Co.), 0.1mM 2-mercapto-ethanol (Sigma-Aldrich Co.), 0.02% v/v sodium pyruvate (Sigma-Aldrich Co.), 100 U/ml penicillin (Invitrogen Co.), 100 U/ml streptomycin (Invitrogen Co.), and 1000 U/ml ESGRO (Invitrgoen Co.) which contains leukemia inhibitory factor (LIF). COS7 and A431.H9 cells were cultured in DMEM (Gibco 11965, Invitrogen Co.) with 10% v/v FBS (Gibco 10082, Invitrogen Co.), and 1% v/v antibiotic-antimicotic (Gibco 15240, Invitrogen Co.). All the cells were cultured in a humidified incubator (37^{o}C in an atomosphere of 5% CO_2). Cell suspensions for the hanging drop experiments were made by dissociating cells with 0.25% trypsin-EDTA (Gibco 25200, Invitrogen Co.), centrifugation of dissociated cells at 1000 rpm for 1 min at room temperature, and re-suspended in growth media. Cell density was estimated using a hemocytometer.

3.2.3 Hanging Drop Spheroid Culture, Culture Media Exchange, and Osmolality Measurement

On the spheroid culture plate, a 15 μl cell suspension was dispensed into the access hole at each cell culture site to form a hanging drop (Figure 3.1c). In order to prevent evaporation, 4 ml of distilled water was added into the peripheral water reservoir. In addition, the plate was sandwiched by a well-plate lid and a 96-well plate filled with distilled water, and wrapped using Parafilm (Figure 3.1e). The growth media was exchanged every other day by taking 5 μl of solution from a drop, and adding 7 μl of fresh growth media into a drop to account for minor evaporation of the original drop. For the osmolality measurement, 10 μl sample solution was pipetted out from a drop and transferred to a vapor pressure osmometer (Vapro Model 5520, Wescor Inc., Logan, UT) for analysis.

3.2.4 Anti-Cancer Drug Sensitivity Testing

For demonstration of anti-cancer drug sensitivity testing, A431.H9 spheroids at three different sizes (300, 1500, and 7500-cell spheroids) were tested under the effect of two types of drug—tirapazamine (TPZ) (Toronto Research Chemicals Inc., Ontario, Canada) and 5-fluorouracil (5-FU) (Sigma-Aldrich Co., St. Louis, MO). According to the procedure mentioned above, A431.H9 spheroids at the specified cell numbers were formed, and their growth media were exchanged every other day. TPZ and 5-FU stock solutions of four times the final testing concentrations (0, 0.1, 1, 10, 100, 1000, 5000 μM)

were initially prepared in Dulbecco's phosphate buffered saline (D-PBS) (Gibco 14190, Invitrogen Co.). On day 2 of A431.H9 spheroid culture, 5 μl of the appropriate concentration of TPZ (or 5-FU) stock solutions was subsequently added to each of the 15 μl A431.H9 cell hanging drop droplets to generate 20 μl hanging drops of cells with drugs. Cellular viability was monitored at 24, 48, 72, and 96 hours of drug incubation using alamarBlue (DAL1025, Invitrogen Co.). Following manufacturer's protocol, 2 μl (one-tenth of each hanging drop sample volume) of alamarBlue was added to each A431.H9 hanging drop spheroid sample and incubated for 2 hours. Following incubation, each A431.H9 hanging drop spheroid sample plate was read using a plate reader (FLx800 Fluorescence Microplate Reader, BioTek Instruments Inc., Winooski, VT) at 525 nm excitation and 590 nm emission to obtain fluorescence intensity readouts. As the fluorescence intensity of alamarBlue is directly proportional to cell number (Figure 3.3c), the average percent cell viability for each drug concentration could be calculated by normalizing to the 0 μM untreated spheroid control. The viability results achieved by the alamarBlue assay were also compared to the viability results obtained by fluorescence microscopy imaging using conventional live/dead stain (LIVE/DEAD Viability/Cytotoxicity Kit for mammalian cells, L3224, Invitrogen Co.). The detailed method of the comparison is shown in the following section with results highlighted in Figure 3.3. Anti-cancer drug sensitivity experiments under 2D control conditions were performed in standard tissue culture treated 96-well plates (Corning Costar 3596, Corning Inc., Lowell, MA), with everything else being the same as the 3D spheroid experiments.

3.2.5 Validation of alamarBlue Viability Assay

In order to confirm the viability results achieved by the alamarBlue assay used in anti-cancer drug sensitivity testing (mentioned above), we compared the results to the viabilities obtained by fluorescence microscopy imaging using conventional live/dead stain. A431.H9 spheroids (initially 1500 cells/spheroid) treated with 5-FU at various concentrations for 48 hrs were stained using LIVE/DEAD Viability/Cytotoxicity Kit for mammalian cells (L3224, Invitrogen). The kit measures the cell viability based on the integrity of cell membranes. The live cells are stained by calcein AM, which emit green fluorescence light (517 nm) when excited by blue light (494 nm); while the dead cells are stained by ethidium homodimer-1, which emit red fluorescence light (617 nm) when excited by green light (528 nm).

To estimate the viabilities from the fluorescence images of 3D spheroids, we captured the fluorescence images at 10 different focal planes spaced 20 μm apart. The images were then reconstructed by stacking focused parts of each figure into a single image using an image processing and analysis software ImageJ developed by NIH with a plug-in, Stack Focuser, which is developed by Michael Umorin (http://rsbweb.nih.gov/ij/plugins/stack-focuser.html). The percentage of live (green) and dead (red) cells for each spheroid can subsequently be determined from the processed images and compared to the untreated control.

Moreover, we tested the linearity of the alamarBlue assay for 3D spheroids viability measurements. Uniformly sized 1500-cell A431.H9 spheroids were transferred

into 96-well plates at various numbers of spheroids per well, and performed alamarBlue assay (6 hr-incubation) for the wells with different spheroid numbers. The linearity of the alamarBlue fluorescent intensity versus the number of spheroids per well was subsequently confirmed on a graph.

3.3 Results and Discussion

3.3.1 Formation of Hanging Drops for Spheroid Culture

A schematic of the 384 hanging drop array plate is shown in Figure 3.1a and an actual picture of the plate containing 192 hanging drops arranged in an alternating fashion is shown in Figure 3.1b. The hanging drop spheroid culture sites are arranged in the standardized 384-well plate format with 16 rows and 24 columns separated by 4.5 mm apart in both directions. A water reservoir designed in the outer ring of the plate further holds up to 4 ml of water to alleviate evaporation problem (Figure 3.1a, b, e). The enlarged cartoon in Figure 3.1a further shows the access hole on the top surface of the plate with a liquid droplet hanging and confined by the diameter of the plateau on the bottom surface. As a result, the geometry of the hanging drop can be kept consistent during the culturing process without spreading out, which leads to more robust and stable culturing conditions not possible on conventional flat hanging drop substrates. Figure 3.1c illustrates the droplet and spheroid formation process in the 384 hanging drop array plate. After a cell suspension droplet is successfully formed, cells slowly aggregate in the

bottom center of the droplet and eventually form into spheroid. The access holes allow direct manipulation of the droplets from the top, thus greatly simplifying the initial droplet formation and subsequent media exchange procedures by eliminating the tedious hanging drop culture dish inversion required in the conventional hanging drop method. Figure 3.1d is a snapshot of the hanging drop formation process in the 384 hanging drop array plate by a commercially available liquid handler (CyBi-Well, CyBio Inc.).

3.3.2 Long-term Culture of Spheroids in Hanging Drops

In order to culture spheroids over long periods of time, the osmolality of the cell culture media in the hanging drops must be kept stable. Due to the small volume nature of the hanging drops, evaporation is inherently rapid and can cause large osmolality shifts in the culture media. In order to prevent this during spheroid culture, the 384 hanging drop array plate was sandwiched by a well-plate lid and a 96-well plate filled with distilled water, and the whole setup subsequently wrapped in parafilm (Figure 3.1e). The water-filled 96-well plate directly on the bottom of the hanging drops provides significant humidification to the hanging drops. In addition, the water reservoir (Figure 3.1a, b, e) in the periphery of the plate further prevents serious evaporation from the hanging drops near the edges of the plate where droplets are more prone to evaporation. To investigate the long-term stability of the hanging drop spheroid cultures, osmolality measurements were performed. Figure 3.2a shows a plot of the average osmolality of the COS7, mES, and A431.H9 cell culture media versus time over 7 to 12 days. With exchange of approximately 30% of the culture media every other day, the osmolality of the media was

kept in the optimal culture range of 300 to 360 mmol/kg (Ozturk and Palsson 1991; Zhou *et al*. 1997; Takagi *et al*. 2000). Figure 3.2b shows the live/dead images of the COS7 and mES cell spheroids, indicating that most cells (>90%) were still alive after 12 days of culture. Figure 3.2c shows that A431.H9 spheroids of various initial sizes are still proliferating over a 7-day culture period. The ease of media exchange and stability of the drop geometry enabled by the inverted plateau structures of the custom 384 drop plate allow for convenient long-term spheroid culture in ways not possible with the conventional hanging drop culture method.

3.3.3 Viability Assays for 3D Spheroids

Routine analysis of cell survival in 3D culture systems is often difficult due to various diffusion and transport limitations in the complex 3D cellular structures. In order to confirm the viability results achieved by the alamarBlue assay used in anti-cancer drug sensitivity testing, we compared the results obtained from alamarBlue assay to the viabilities obtained by fluorescence microscopy imaging using conventional live/dead stain. Figure 3.3a shows the comparison between the two methods, and Figure 3.3b shows the reconstructed fluorescence images. For the four concentrations tested in the experiments, the viabilities obtained from the two methods have discrepancies less than 10%, except for the 1 μM 5-FU case. Such viability discrepancy may be caused by the different principles for estimating the cell viability in these two methods. In addition, due to the 3D structures of the spheroids, it is usually challenging to image an intact spheroid. Also, fluorescence dye may not be able to freely diffuse into an intact spheroid.

In addition to validating the alamarBlue assay by comparison with live/dead staining, the linearity of the alamarBlue assay for 3D spheroids viability measurements was also tested directly. The alamarBlue fluorescence intensities for different amount of spheroids were measured on a plate reader after incubation. Figure 3.3c shows the measurement results, which suggests the excellent linearity of the assay. In summary, precisely estimating cell viability for 3D cultures in a high throughput manner is still a challenging task, and alamarBlue assay demonstrated in this chapter provides a reasonable solution to routine analysis of cell viability.

3.3.4 Anti-cancer Drug Sensitivity Testing

To analyze cell-based assay capability, an anti-cancer drug sensitivity test was performed using 2 drugs with distinctly different activity profiles: a conventional anti-cancer drug 5-fluorouracil (5-FU, Sigma-Aldrich Co., St. Louis, MO) that inhibits cellular proliferation (Valeriote and Santelli 1984), and a hypoxia-triggered cytotoxin tirapazamine (TPZ, Toronto Research Chemicals Inc., Ontario, Canada) that causes DNA damage (Peters *et al*. 2001), on A431.H9 cells under both 2D and 3D spheroid culture conditions. Figure 3.4a shows cell viability at 10 μM 5-FU 96 hours after drug treatment for 7500-cell A431.H9 spheroids and 2D culture condition. At the same 5-FU concentration, there is only 5% viability relative to untreated control for 2D cultures, but still 75% viability relative to control for 3D spheroids. This clearly shows that A431.H9 cells are more resistant to 5-FU in 3D than 2D cultures. Figure 3.5a and b further show

that the IC_{50} of A431.H9 cells cultured in 2D condition is about 0.1 μM, while the IC_{50} of the A431.H9 3D spheroids is more resistant with an IC_{50} of 1 to 100 μM. Due to the 3D integrity of spheroids, it is more difficult for 5-FU to diffuse and penetrate into the center cell mass. Furthermore, 5-FU specifically targets proliferating cells, and thus would not kill the quiescent cells in the spheroids. Whereas in 2D monolayer cultures, cells proliferate at a faster rate and thus 5-FU inhibits cellular growth more effectively.

In contrast, TPZ is a hypoxia-activated cytotoxin. Figure 3.4a shows that at 10 μM TPZ 96 hours after drug treatment, there is still 75% viability relative to control for 2D cultures, but only 40% viability for 7500-cell A431.H9 spheroids. The IC_{50} of A431.H9 cells cultured in 2D is about 50 μM, while the IC_{50} of the A431.H9 3D spheroids for all 3 sizes is about 8 μM (Figure 3.5c, d). Here, A431.H9 cells are more resistant to TPZ when cultured under 2D rather than 3D conditions. This is likely because TPZ is activated more in spheroids where active oxygen consumption by cells and limits in diffusive oxygen transport creates a hypoxic core similar to actual solid tumors (Sutherland 1988). Such distinct cellular responses from the same cells to the same drugs tested under 2 different culture conditions highlights the importance of using 3D models in drug screening and testing. Statistical analysis ANOVA followed by pairwise comparisons between the culture conditions (spheroid sizes or 2D) using Holm-Sidak tests were performed for each 5-FU and TPZ concentration groups. The statistically significantly different groups are shown in Figure 3.5a and c.

Finally, we performed combination drug treatment (5-FU and TPZ) on the 7500-cell A431.H9 spheroids. The combined treatment has an additive trend. The viability is 75% and 40% for spheroids treated with 10 μM of 5-FU and 10 μM of TPZ, respectively (Figure 3.4a). But the viability decreased to only 20% when the spheroids were under combined treatment of 10 μM 5-FU and 10 μM TPZ (Figure 3.5e). The additive effect is reasonable since 5-FU is an anti-proliferation drug that targets proliferating cells in the peripheral layers of spheroids and TPZ is a hypoxic drug that kills cells in the hypoxic core of spheroids.

3.4 Conclusion

We describe the design and fabrication of a high-throughput and versatile 384 hanging drop array plate for cellular spheroid formation, culture, and drug testing. The platform greatly simplifies the proven but traditionally inconvenient hanging drop culturing method in a format that is compatible with existing liquid handling robots. Anti-cancer drug sensitivity testing on A431.H9 cells show that cytotoxicity can be drastically different in the physiological 3D spheroids formed in the 384 hanging drop array plates compared to 2D monolayer cultures in conventional multiwell plates. Although this study focused on response of cancer spheroids, the user-friendly high-throughput 3D culture system is applicable to multiple cell types. We believe the platform will be valuable in a wide range of studies where 3D spheroid cultures and high-throughput multiplexing is needed.

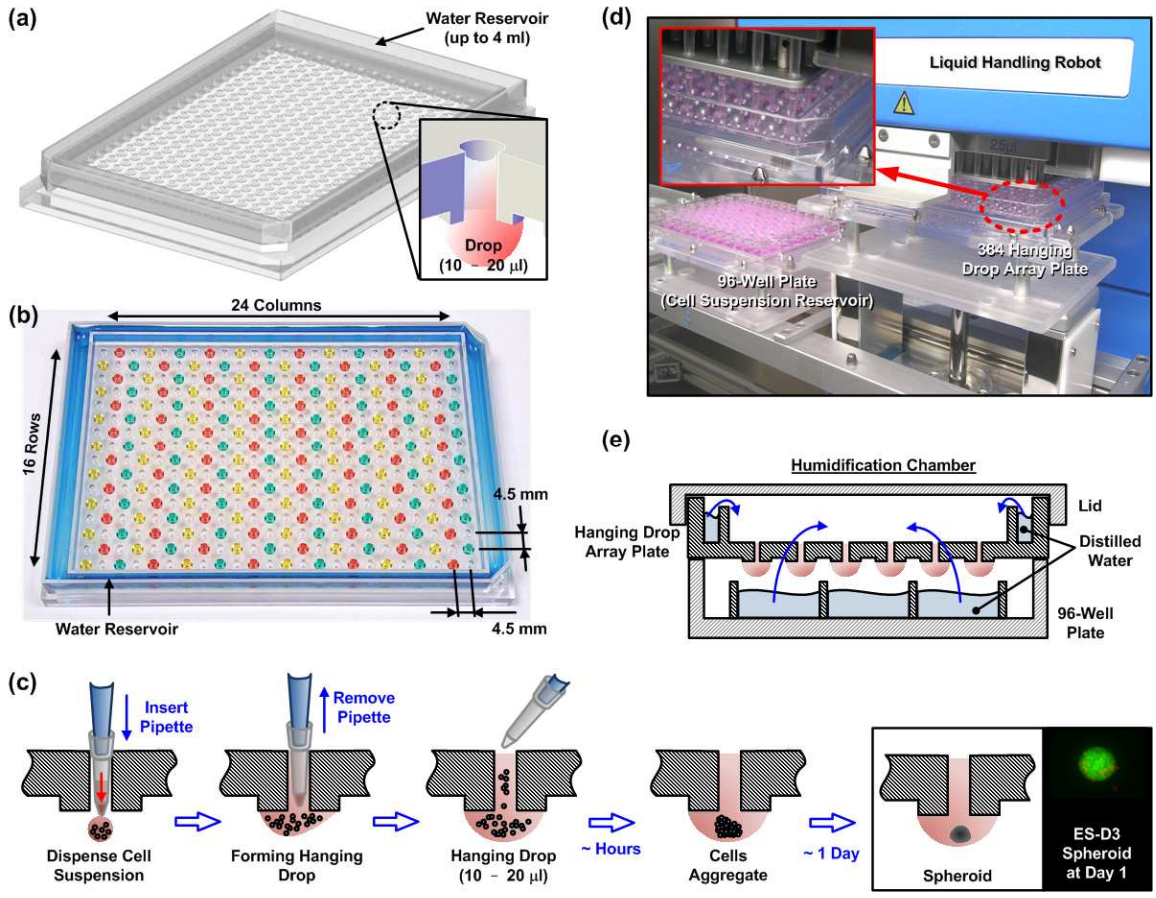

Figure 3.1. **(a)** Illustration of the designed 384 hanging drop spheroid culture array plate, and its cross-sectional view. **(b)** Photo and key dimensions of the array plate. **(c)** Cartoon of the hanging drop formation process in the array plate. The pipette tip is first inserted through the access hole to the bottom surface of the plate, and cell suspension is subsequently dispensed. Cell suspension is quickly attracted to the hydrophilic plate surface and a hanging drop is quickly formed and confined within the plateau. Within hours, individual cells start to aggregate and eventually form into a single spheroid around 1 day. **(d)** Photo of the 384 hanging drop array plate operated with liquid handling robot capable of simultaneously pipetting 96 cell culture sites. **(e)** Cartoon of the final humidification chamber used to culture 3D spheroids in the hanging drop array plate. The 384 hanging drop array plate is sandwiched between a 96-well plate filled with distilled water and a standard-sized plate lid. Distilled water from the bottom 96-well plate and the peripheral water reservoir prevent serious evaporation of the small volume hanging drops.

Figure 3.2. **(a)** Osmolality of the culture media from the hanging drops of COS7, mES, and A431.H9 cell spheroids with various cell populations over a 7- and 12-day culture period. Data are expressed as the mean ± s.e.m. **(b)** Fluorescence images of live/dead stained COS7 and mES cell spheroids over a 12-day culture. **(c)** Volume of A431.H9 spheroids over a 7-day culture for various initial cell numbers per spheroid. n = 14 for each initial cell number condition. Data are expressed as the mean ± s.e.m.

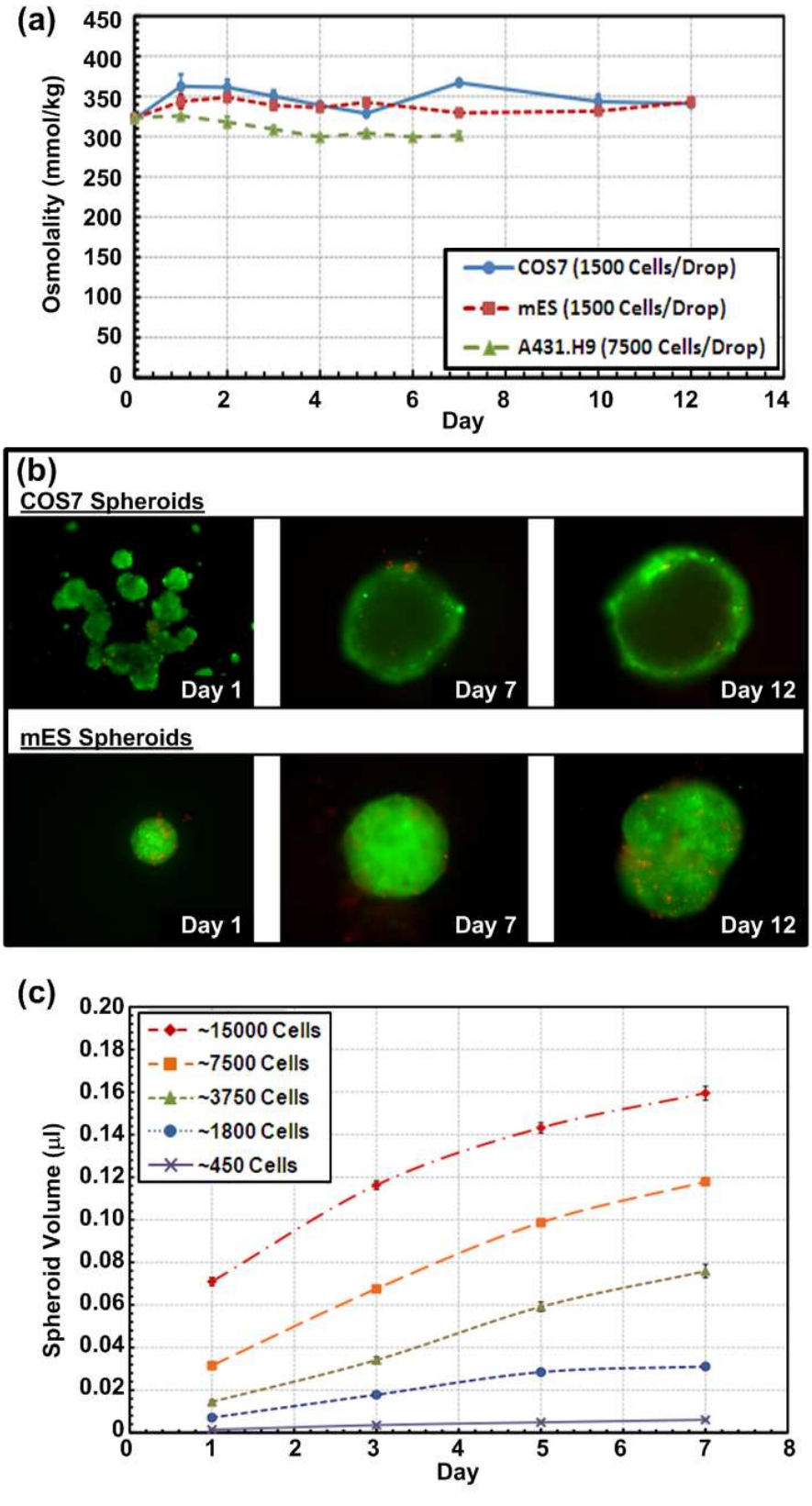
(a)
Osmolality (mmol/kg)
Day
COS7 (1500 Cells/Drop)
mES (1500 Cells/Drop)
A431.H9 (7500 Cells/Drop)
(b)
COS7 Spheroids
Day 1
Day 7
Day 12
mES Spheroids
Day 1
Day 7
Day 12
(c)
Spheroid Volume (µl)
Day
~15000 Cells
~7500 Cells
~3750 Cells
~1800 Cells
~450 Cells

Figure 3.2

Figure 3.3. (a) Comparison of cell viability of A431.H9 spheroids based on alamarBlue assay and fluorescence microscopy imaging with live/dead stain. **(b)** Fluorescence images of the A431.H9 spheroids treated with different concentrations of 5-Fu. **(c)** Alamar Blue assay linearity characterization: fluorescence intensity measurements in the Alamar Blue assay for different numbers of A431.H9 spheroids. n = 5 for each 5-FU concentration in **(a)**, and n = 5 for each spheroid number group in **(c)**. Data are expressed as the mean ± standard deviation.

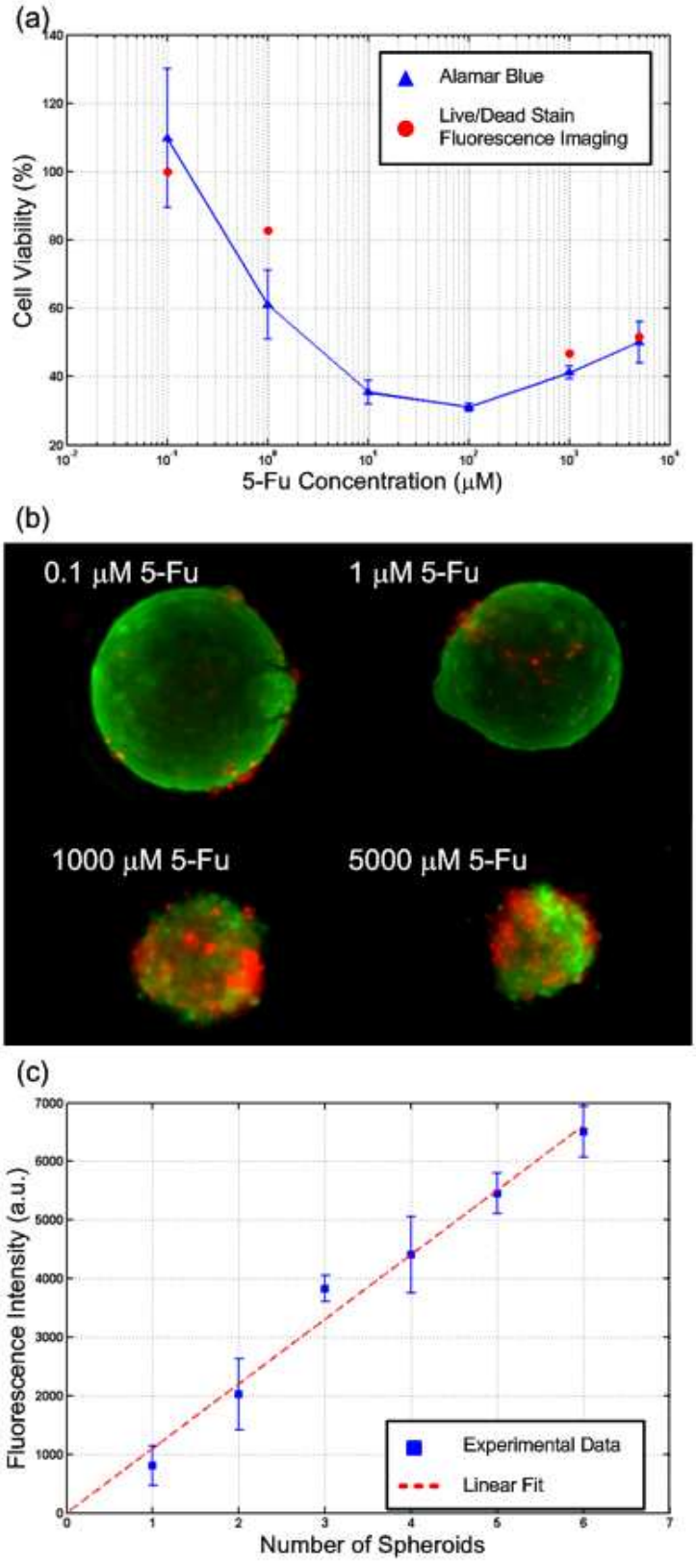
(a)
Alamar Blue
Live/Dead Stain
Fluorescence Imaging
Cell Viability (%)
5-Fu Concentration (μM)
(b)
0.1 μM 5-Fu
1 μM 5-Fu
1000 μM 5-Fu
5000 μM 5-Fu
(c)
Fluorescence Intensity (a.u.)
Experimental Data
Linear Fit
Number of Spheroids

Figure 3.3

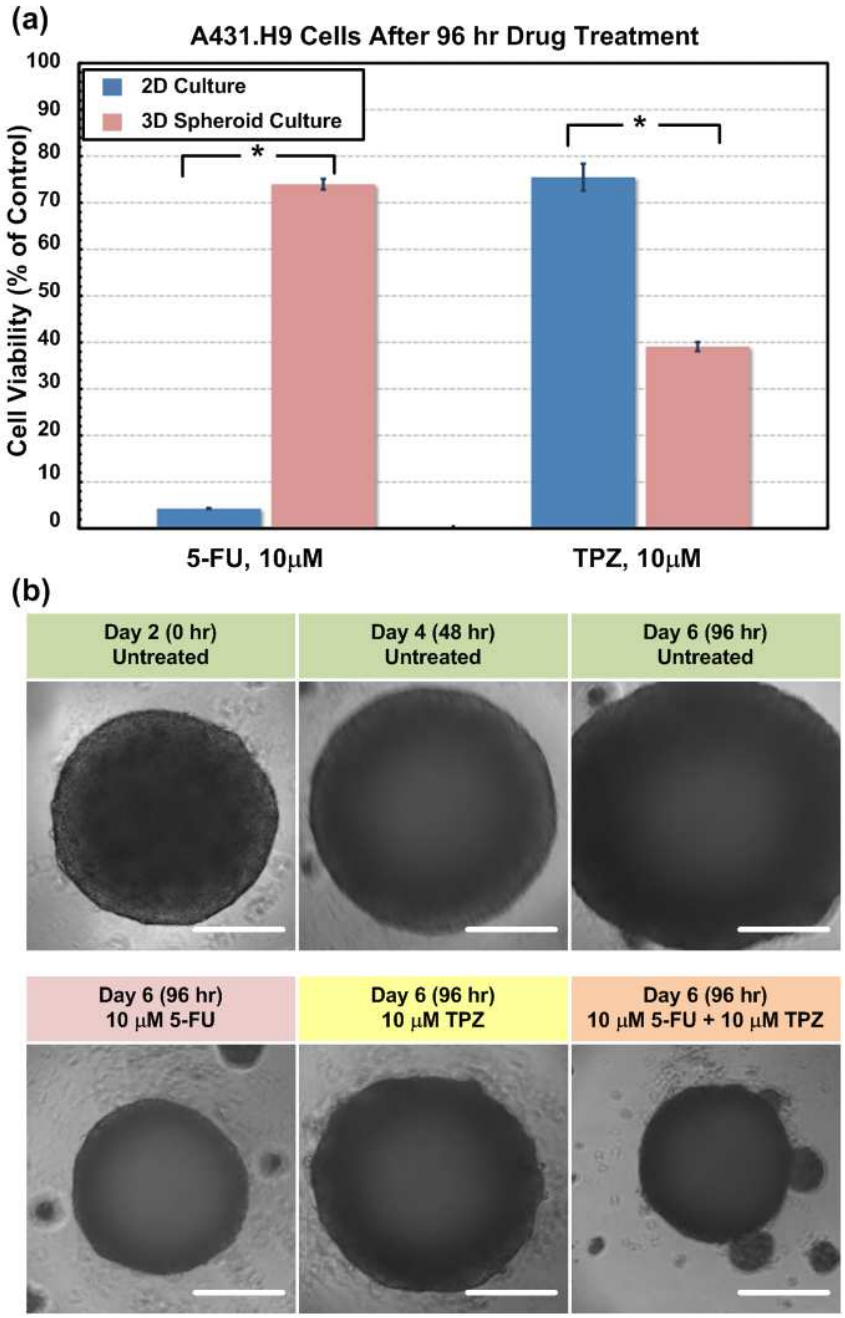

Figure 3.4. **(a)** Bar graph of the cell viability at 10 μM 5-FU, and 10 μM TPZ 96 hours after drug treatment for 2D A431.H9 monolayer culture and 7500-cell A431.H9 3D spheroid culture conditions. For both drugs, the viability of A431.H9 cells was statistically different between 2D monolayer and 3D spheroid culture conditions. Statistical significance is determined by two-tailed Student's t-Test (*, $P < 0.01$) $P = 1.75 \times 10^{-16}$ for 5-FU, $P = 1.22 \times 10^{-6}$ for TPZ. $n = 8$ for 2D culture condition and $n = 14$ for 3D spheroid culture condition. Data are expressed as the mean ± s.e.m. **(b)** Time-lapse images of control untreated 7500-cell A431.H9 spheroid, and spheroids treated with 10 μM 5-FU, 10 μM TPZ, and 10 μM 5-FU + 10 μM TPZ 96 hours after treatment. Scale bar is 200 μm.

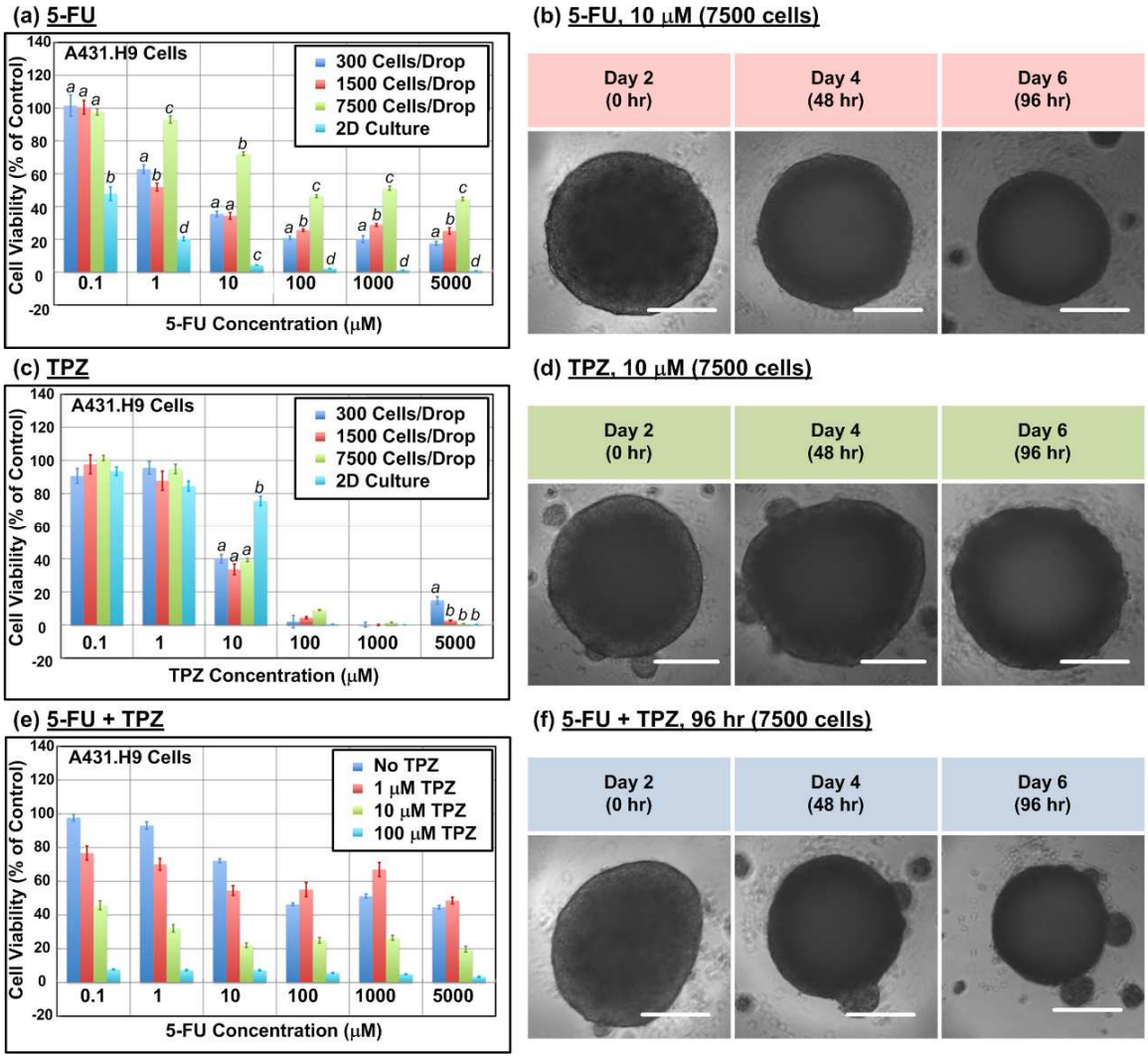

Figure 3.5. **(a)** Bar graph of the cell viability at various 5-FU concentrations 96 hours after drug treatment for 300, 1500, and 7500-cell A431.H9 3D spheroids and 2D culture condition. Different letters between culture conditions (spheroid size or 2D) within a 5-FU concentration represent a significant difference between the spheroid sizes or 2D (a, b, c, d = $p < 0.01$). **(b)** Time-lapse images of 7500-cell A431.H9 spheroids treated with 10 μM 5-FU. **(c)** Bar graph of the cell viability at various TPZ concentrations 96 hours after drug treatment for 300, 1500, and 7500-cell A431.H9 spheroids and 2D culture condition. Different letters between culture conditions (spheroid size or 2D) within a TPZ concentration represent a significant difference between the spheroid sizes or 2D (a, b = $p < 0.01$). **(d)** Time-lapse images of 7500-cell A431.H9 spheroids treated with 10 μM TPZ. **(e)** Bar graph of the cell viability at various 5-FU concentrations 96 hours after drug treatment for 7500-cell A431.H9 spheroids with 0, 1, 10, and 100 μM TPZ. **(f)** Time-lapse images of 7500-cell A431.H9 spheroids treated with 10 μM 5-FU + 10 μM TPZ. Statistical analysis was performed by ANOVA followed by Holm-Sidak tests. Spheroid size or 2D groups that are statistically significantly different are designated with different letters (a, b, c, d). n = 8 for 2D culture condition and n = 14 for 3D spheroid culture condition. Data are expressed as the mean ± s.e.m. Scale bar is 200 μm.

3.5 References

1. Del Duca D, Werbowetski T, Del Maestro RF. Spheroid preparation from hanging drops: characterization of a model of brain tumor invasion. J Neurooncol 2004;67(3):295-303.

2. Friedrich J, Ebner R, Kunz-Schughart LA. Experimental anti-tumor therapy in 3-D: spheroids-old hat or new challenge. Int J Radiat Biol 2007;83(11-12):849-71.

3. Friedrich J, Seidel C, Ebner R, Kunz-Schughart LA. Spheroid-based drug screen: considerations and practical approach. Nat Protoc 2009;4(3):309-24.

4. Fukuda J, Khademhosseini A, Yeo Y, Yang X, Yeh J, Eng G, et al. Micromolding of photocrosslinkable chitosan hydrogel for spheroid microarray and co-cultures. Biomaterials 2006;27(30):5259-67.

5. Ho M, Hassan R, Zhang J, Wang QC, Onda M, Bera T, et al. Humoral immune response to mesothelin in mesothelioma and ovarian cancer patients. Clin Cancer Res 2005;11(10):3814-20.

6. Ivascu A, Kubbies, M. Rapid generation of single-tumor spheroids for high-throughput cell function and toxicity analysis. J Biomol Screening 2006;11(8):922-32.

7. Kunz-Schughart LA, Freyer JP, Hofstaedter F, Ebner R. The use of 3-D cultures for high-throughput screening: the multicellular spheroid model. J Biomol Screen 2004;9(4):273-85.

8. Lee WG, Ortmann D, Hancock MJ, Bae H, Khademhosseini A. A hollow sphere soft lithography approach for long-term hanging drop methods. Tissue Eng Part C Methods 2010;16(2):249-59.

9. Ozturk SS, Palsson O. Effect of medium osmolarity on hybridoma growth, metabolism, and antibody production. Biotechnol Bioeng 1991;37(10):989-93.

10. Pampaloni F, Reynaud EG, Stelzer EHK. The third dimension bridges the gap between cell culture and live tissue. Nat Rev Mol Cell Bio 2007;8(10):839-45.

11. Peters KB, Wang H, Brown JM, Iliakis G. Inhibition of DNA replication by tirapazamine. Cancer Res 2001;61(14):5425-31.

12. Sakai Y, Nakazawa K. Technique for the control of spheroid diameter using microfabricated chips. Acta Biomater 2007;3(6):1033-40.

13. Sutherland RM. Cell and environment interactions in tumor microregions: the multicell spheroid model. Science 1988;240(4849):177-84.

14. Takagi M, Hayashi H, Yoshida H. The effect of osmolarity on metabolism and morphology in adhesion and suspension chinese hamster ovary cells producing tissue plasminogen activator. Cytotechnology 2000;32(3):171-9.

15. Toh YC, Zhang C, Zhang, J, Khong YM, Chang S, Samper VD, et al. A novel 3D mammalian cell perfusion-culture system in microfluidic channels. Lab Chip 2007;7(3):302-9.

16. Torisawa Y, Chueh BH, Huh D, Ramamurthy P, Roth TM, Barald KF, et al. Efficient synchronous formation of uniform-sized embryoid bodies using a compartmentalized microchannel device. Lab Chip 2007;7(6):770-6.

17. Torisawa Y, Takagi A, Nahimoto Y, Yasukawa T, Shiku H, Matsue T. A multicellular spheroid array to realize spheroid formation, culture, and viability assay on a chip. Biomaterials 2007;28(3):559-66.

18. Ungrin MD, Joshi C, Nica A, Bauwens C, Zandstra PW. Reproducible, ultra high-throughput formation of multicellular organization from single cell suspension-derived human embryonic stem cell aggregates. PLoS ONE 2008;3(2):e1565.

19. Valeriote F, Santelli G. 5-Fluorouracil (FUra). Pharmacol Ther 1984;24(1):107-32.

20. Wu LY, DiCarlo D, Lee LP. Microfluidic self-assembly of tumor spheroids for anticancer drug discovery. Biomed Microdev 2008;10(2):197-202.

21. Zhou W, Chen CC, Buckland B, Aunins J. Fed-batch culture of recombinant NS0 myeloma cells with high monoclonal antibody production. Biotechnol Bioeng 1997;55(5):783-92.

CHAPTER 4

384 Hanging Drop Array Plate Characterization, Modification, and Biomedical Applications

The previous chapter describes the development of a simple, user-friendly, and versatile 384 hanging drop array plate for 3D spheroid culture and the importance of utilizing 3D cellular models in anti-cancer drug sensitivity testing. While the 384 hanging drop array plate allows for high-throughput capabilities and offers significant improvements over existing 3D spheroid culturing methods, various issues remain to be addressed to improve the usability and enable broader use of the plate for practical long-term 3D spheroid culture. In this chapter, we describe efforts to characterize the robustness of the 384 hanging drop array plate in terms of assay performance and long-term stability of the hanging drops, and show the versatility of the plate. We find that the original 384 hanging drop array plate performance is very robust in fluorescence- and colorimetric-based assays. We subsequently moved on to modify the plate to further optimize for long-term stability of the hanging drops. Finally, we demonstrate different plate capabilities and applications, including: spheroid transfer and retrieval for Janus spheroid formation and analysis, sequential addition of reagents or cells for sequential drug treatment and concentric layer patterning of different cell types, and culture of a wide variety of cell types. Collectively, these results prove that the versatile and robust

384 hanging drop array plate for 3D spheroid culture is as practical and user-friendly as conventional multi-well plates for routine 2D cell culture.

4.1 Introduction

4.1.1 Need for High-throughput 3D Cell Assays

High-throughput 3D cell culture is motivated by the need to work with accurate *in vitro* models in drug discovery and therapy test programs. *In vitro* tumor models where cells are cultured outside living systems are central to the development of novel drugs and therapeutics. However, typical *in vitro* models where cells are cultured in conventional 2D petri-dishes do not faithfully recapitulate the physiological environments *in vivo*. Various cell types have been shown to behave differently when cultured under 2D vs. 3D (Yamada and Cukierman 2007). With increasing realization that the surrounding environment is critical to cells, various 3D culture systems that better mimic physiological tissues have been valued as important research tools. Spheroids, which are spherical clusters of cells formed by self-assembly, stand out as one of the best models for 3D culture (Kunz-Schughart *et al*. 2004; Friedrich *et al*. 2009). Currently, however, most initial studies in drug development are still based on 2D cell assays, which often skew research results and have limited predictive power in clinical efficacy (Hirschhaeuser *et al*. 2010). Since the time and costs of drug development increase substantially during the animal models phase and even more in the subsequent clinical trials, it is crucial to identify promising candidates accurately in the early developmental stages. Implementation of high-throughput 3D cell culture screening assays is anticipated as a potent tool to expedite and accurately select key molecules in drug development. Although the advantages of spheroids are widely known, it has been

difficult to scale up spheroid culture. Typical spheroid culture methods are often tedious, low-throughput, difficult to handle, and produce non-uniform samples. Various such complications have thus hindered more researchers from adapting the more accurate 3D spheroid cultures into routine use. To promote wider usage of 3D spheroid cultures in research and pharmaceutical development, we have successfully developed the 384 hanging drop array platform for high-throughput spheroid culture that offers simplified liquid handling procedures and compatibility with high-throughput screening (HTS) instruments (such as plate readers and liquid handling robots) as mentioned in the last chapter.

4.1.2 Z'-factor and Z-factor

HTS is an essential initial step in drug discovery. The ability to identify true active compounds ("hits") depends greatly on the quality of assays and proper analysis of data (Zhang *et al*. 1999 Sui and Wu 2007). Therefore, high-throughput 3D cell culture needs reliable assays for endpoint analysis to obtain accurate readouts. Assays for HTS not only need to be miniaturized in sample volume, high-throughput, and robust, but also require adequate sensitivity, reproducibility, and accuracy in order to discriminate among a large pool of compounds that produce a huge range of activity (Zhang *et al*. 1999). In most HTS experiments, because each compound is only tested in singlet or duplicate, a high degree of accuracy and sensitivity in the assay is critical for identifying hits (Zhang *et al*. 1999). Since practically all assay methodologies contain instrumental and human-associated errors and perturbations, all of the measurements from an assay contain some

degree of variability. Real hits need to be identified despite such signal measurement variation. As a result, assessment of the screening data variability is critical in determining whether an assay can identify hits with confidence in the design and validation of HTS assays. A high quality HTS assay must be able to identify the few compounds with desired biological activity with high confidence. Previously, signal-to-noise ratios (S/N) and signal-to-background ratios (S/B) have been used to evaluate the performance of HTS assays (Sittampalam *et al*. 1997). These concepts are constructive and useful; however, they still lack uniformity and simplicity in analysis of the relevant parameters. Over the past decade, researchers from the HTS community have used the Z-factor (Zhang *et al*. 1999) as a widely accepted standard to evaluate the quality of a HTS assay.

Z'- or Z- factor is an assay performance measurement that provides an easy and useful summary of assay quality and robustness (Zhang *et al*. 1999; Sui and Wu 2007; Birmingham *et al*. 2009). Z'-factor is typically used in assay optimization as it is based on controls, whereas Z-factor is often used during screening to assess performance of the screen on actual samples (Zhang *et al*. 1999; Birmingham *et al*. 2009). Z'- and Z-factors are defined as follows (Zhang *et al*. 1999):

$$\text{Z'-factor} = 1 - (3\sigma_{hc} + 3\sigma_{lc}) / \left| \mu_{hc} - \mu_{lc} \right|$$

$$\text{Z-factor} = 1 - (3\sigma_{s} + 3\sigma_{c}) / \left| \mu_{s} - \mu_{c} \right|$$

μ indicates mean, σ indicates standard deviation, "hc" indicates the high-value control (positive control), "lc" indicates the low-value control (negative control), "s" indicates sample value, and "c" indicates negative control. The range of both measure is from

negative infinity to 1, with > 0.5 as a very good assay, > 0 an acceptable assay, and < 0 an unacceptable assay (Zhang *et al*. 1999; Birmingham *et al*. 2009). Table 4.1 (Zhang *et al*. 1999; Birmingham *et al*. 2009) summarizes the meaning of Z'- and Z-factors in more detail. To characterize the performance of our 384 hanging drop plate for fluorescence- and colorimetric-based assays, we utilized various concentrations of fluorescein and yellow food color liquid as sample drops to calculate the Z'- and Z-factors. For both fluorescence-and colorimetric-based assays, we show that the Z'- and Z-factors calculated for the 384 hanging drop plate are comparable to those values obtained from commercially-available clear 384-well plates.

4.1.3 Original Design of the 384 Hanging Drop Array Plate

The current 384 hanging drop array plate (Figure 4.2a) as described in Chapter 3 offers considerable advancements to the current 3D spheroid culture standards. It not only offers high-throughput capability suitable for the pharmaceutical industry, but is also designed in a simple, convenient multi-well plate format already familiar to researchers in academia. Nevertheless, to further improve the usability and versatility of the plate to benefit more users and allow for a wider range of applications, the current plate must be optimized for stable long-term culture. Specifically, the long-term stability of the droplets hanging from the access holes of the current plate must be addressed. The original plate design is limited by the spontaneous spreading out of droplets over time, and its easy susceptibility to spread out upon sudden accelerations such as shocks and strikes. Droplets formed in the original version of the plate have been found to be prone

to spreading out from the bottom of the plate in incubator cultures of more than 7 days (Figure 4.2b). Unexpected collisions or other physical disturbances on the hanging drops further exacerbate the droplet instability issue and lead to coalesce of droplets. In addition, during routine fluid manipulations, once wet pipette tips come in contact with the top flat surface of the plate (not directly inside the access holes), existing or subsequently formed droplets tend to merge with the undesired liquid remnant left on the top surface (Figure 4.2b). These unwanted conditions altogether render the ruined hanging drops inappropriate for further spheroid culture and monitoring. Therefore, there is a need to refine the current design of the 384 hanging drop plate to ensure that the hanging drops would be robust against sudden shocks and stable over time. A recent publication by Kalinin et al. offers useful insights to enhance droplet stability using micro-topographical rings (Kalinin *et al*. 2008). Here, we addressed these issues by modifying the original 384 hanging drop plate with the addition of extra micro-feature rings around the top surface access hole openings and the bottom surface plateaus (Figure 4.2c, d). We show that hanging drops formed in the newly modified plates are stable without the issue of droplets spreading out for up to 24 days of incubator culture.

4.1.4 Techniques and Applications of Spheroid Cultures

Many types of mammalian cells spontaneously aggregate into 3D spheroids when cultured in environments where cell-cell interactions dominate over cell-substrate interactions (Lin and Chang 2008; Hirschhaeuser *et al*. 2010; Friedrich *et a*l. 2009). Recent realization of the importance of 3D cell culture has attracted more researchers to

adapt 3D spheroid cultures into biological studies. Compared to conventional 2D monolayer cultures, 3D spheroids resemble physiological tissues and tumors much better in terms of structural and functional properties (Lin and Chang 2008). Various primary or progenitor-like cell types also show significantly enhanced viability and functions when grown as spheroids (Lin and Chang 2008). Recently, spheroid research has been devoted to various areas in biology including cancer biology, developmental biology, tissue engineering, and other disciplines. Specifically, spheroids serve as excellent models for solid tumors, components in bioartificial livers (Lin and Chang 2008), cellular building blocks in tissue engineering, and embryoid bodies. Tumor spheroids can be used to study various types of cancers that are found growing as spherical aggregates *in vivo*, such as the ascites in ovarian cancer (Shield *et al*. 2009). They have also been used widely as models to study cancer stem cells, cancer metastasis, invasion, and for therapeutic screening (Lin and Chang 2008; Hirschhaeuser *et al*. 2010). In addition, spheroids can also be applied to study cellular migration and tumor dissemination from 3D constructs, signaling and cross-talks between cells cultured in 3D environments (secreted autocrine and paracrine factors from 3D constructs with inherent metabolic profiles and diffusion/transport limitations), 3D cell-cell interactions and confrontational studies, differentiation of stem cells from co-cultures of different cell types or addition of factors, and 3D patterning for tissue engineering purposes. However, many of these studies require sophisticated manipulation and analysis techniques not commonly attainable through conventional spheroid formation platforms, such as formation of uniform pool of spheroids, formation of multi-cell type mixed co-culture spheroids, sequential addition of reagents, and retrieval and addition of single cell suspensions or

spheroids. Here, we demonstrate the versatility of our plate with biomedical applications in the formation of a wide variety of spheroids from different cell types, concentric layer patterning of different cell types into spheroids, mixed co-culture spheroid formation, and spheroid transfer for 3D cell confrontations.

4.2 Materials and Methods

4.2.1 Z'-factor and Z-factor Calculations

To calculate the Z'-factor and Z-factor of the 384 hanging drop array plate for fluorescence- and colorimetric-based assays, we formed 15 μl hanging drops in all 384 sites of the plate from various concentrations of fluorescein (sodium salt, F6377, Sigma-Aldrich Co.) and yellow food color, respectively, according to the concentration maps shown in Figure 4.1a, c.

For fluorescence-based assay, 1mg/mL stock solution of fluorescein was first prepared and dissolved in PBS (Phosphate-Buffered Saline, Gibco 10010, Invitrogen Co.). The stock solution was subsequently serially diluted to all the concentrations listed in the map (Figure 4.1a, range from PBS only—negative control to 50μg/mL—positive control). 384 15 μl hanging drops were then formed in the 384 hanging drop plate from all the concentrations of fluorescein solutions using a robotic liquid handler (CyBi-Well, CyBio Inc.). The plate was then read on a microplate reader (PHERAStar FS, BMG Labtech),

with 485 nm excitation, 520 nm emission and reading from the bottom of the plate to obtain fluorescence intensity readouts. Z'-factor and Z-factors at each fluorescein concentration was then calculated from the fluorescence intensity readings according to the formulas mentioned above.

For colorimetric-based assay, 100% solution of yellow food color was first prepared by adding 175 μL of stock yellow food color (McCormick & Company, Inc.) into 100 mL of distilled water (Gibco 15230, Invitrogen Co.). A percentage dilution, beginning with the 100% solution of yellow food color, was then performed to make all the percentages listed in the map (Figure 4.1c, range from distilled water only—negative control to 100% yellow food color solution—positive control). 384 15 μl hanging drops were then formed in the 384 hanging drop plate from all the percentages of yellow food color solutions using a robotic liquid handler (CyBi-Well, CyBio Inc.). The plate was then read on a microplate reader (PHERAStar FS, BMG Labtech) to determine the absorbance of each yellow food color percentage at 405nm. Z'-factor and Z-factors at each yellow food color percentage was then calculated from the absorbance readouts according to the formulas mentioned above.

The same fluorescein and yellow food color solutions were also pipetted into standard clear, polystyrene 384-well plates (Corning COSTAR 3701) at 2 volumes (15 μl and 50 μl) using a robotic liquid handler (CyBi-Well, CyBio Inc.) in the same concentration pattern as the 384 hanging drop plates (Figure 4.1a, c). The plates were subsequently read on a microplate reader (PHERAStar FS, BMG Labtech) using the

same settings as for the 384 hanging drop plates to obtain fluorescence intensity and absorbance readouts. Z'-factor and Z-factors at each yellow food color percentage was then calculated from the fluorescence intensity and absorbance readouts according to the formulas mentioned above for comparison with the data from the 384 hanging drop plates.

4.2.2 Modifications to the Original 384 Hanging Drop Array Plate

To enhance the long-term stability of the hanging drops in the 384 hanging drop plates, extra micro-topographical ring-like structures were proposed to be added to the bottom surface of the plate around the plateaus (Figure 4.2d). In addition to the original bottom plateau design of the plate, a bottom trench design was also considered (Figure 4.2d). The proposed extra bottom ring structure would subsequently be added to either the original bottom 0.5 mm height plateau design or the new 0.5 mm deep trench design (Figure 4.2d), depending on droplet stability test results. In order to determine the best ring dimensions to enhance droplet stability, varying dimensions of the extra bottom ring structures (Table 4.2) were compared. Rapid prototype plates each with multiple different design features and dimensions (Table 4.2) were fabricated by a stereolithography machine (SLA Viper si2, 3D Systems, Inc.). A piece of glass slide was attached to the bottom of each prototype plate (Figure 4.3a). 15 μL cell culture media (GIBCO 11965 DMEM + 10% FBS (number) + 1% Anti-Anti (number)) droplets were formed in 2 hanging drop sites located at 2 different radii (R_1 and R_2) for each design. The rapid prototype plates were each subsequently placed on a spin coater (Cee 200X, Brewer Science, Inc., Rolla, MO) and spun at increasing speeds (with 4 seconds of ramp

time and 20 seconds of total spin time), starting at 210 rpm with 30rpm increments until the media droplets spread out. The maximum speed at which each of the droplets spread out was recorded and characterized for droplet stability design characterization. The rationale is that depending on the distance (R_1 or R_2) of the droplets to the center of the spindle, each droplet will experience different centripetal acceleration. The best design is determined to be the one that is able to maintain the droplet stable at the highest centripetal acceleration. The centripetal acceleration is calculated using the following formula:

$$a_c = v^2/r = (\omega r)^2/r = \omega^2 r$$

a_c is the centripetal acceleration, v is the linear velocity, r is the radius, ω is the angular velocity.

To prevent droplets from merging with undesired liquid remnants unintentionally left on the top surface of the plate, both extra micro-topographical ring-like and trench-like structures were proposed to be added to the top surface of the plate around the openings of the access holes. Four different dimensions were compared for the extra ring and trench designs (Table 4.3). A rapid prototype plate with a total of 8 design features and dimensions (Table 4.3) was fabricated by a stereolithography machine (SLA Viper si2, 3D Systems, Inc.). 15 μL cell culture media (Gibco 11965 DMEM + 10% FBS (number) + 1% Anti-Anti (number)) droplets were formed by manually pipetting in 192 access holes at staggered positions. The plate was subsequently sandwiched between a 96-well plate lid and plate filled with distilled water, and incubated in a humidified incubator (37^{o}C in an atomosphere of 5% CO_2) for a total of 8 days. Cell culture media

was exchanged every other day using a multi-channel pipettor (remove 5 μL out and add back 7 μL in), and the number of droplets spreading out on the top surface of the plate was recorded for each design. The best design was determined to be the one with the least number of droplets spreading out from the top surface.

4.2.3 Testing the Stability and Robustness of Hanging Drops in the Modified 384 Hanging Drop Array Plate

Unfortunately, due to the original injection mold manufacturing limitations (Xcentric Mold & Engineering, Inc., Chesterfield, MI), the desired design cannot be fabricated precisely as the proposed ring features were too small (both top and bottom rings with 0.25 mm width and 0.50 mm height) (Figure 4.2e). Therefore, the final design was compromised to ring features with 0.5 mm width and 0.50 mm height (Figure 4.2e). The new refined plates were also fabricated by injection molding in the same clear polystyrene material as the original plates.

To compare the hanging drop stability in both the original and new design plates, 384 15μL hanging drops were formed in both the original and new plates by a liquid handling robot (CyBi-Well, CyBio Inc.). The plates were not coated in 0.1% Pluronic F108 (BASF Co., Ludwigshafen, Germany) solution as described in Chapter 3, but directly UV sterilized in a UV oven chamber for 30 minutes prior to use. After forming handing drops, the plates were sandwiched between a 96-well plate lid and plate filled with distilled water, and incubated in a humidified incubator (37^{o}C in an atomosphere of 5% CO_2) for 14 days. Cell culture media was exchanged every other day using the liquid

handling robot (remove 5 μL out and add back 7 μL in). Right after media exchange, each plate was then placed through 20 cycles of up and down, left and right motions on the liquid handling robot stage at the maximum speeds allowed by the liquid handler settings. The number of droplets spreading out from both the top and bottom surfaces of the plate was recorded for each plate after the cycles.

4.2.4 General Cell Culture

Murine embryonic stem (mES) cells (ES-D3) cells were cultured in dishes coated with 0.1% w/v porcine gel (Sigma-Aldrich Co.) and maintained in medium consisting of Dulbecco's Modified Eagle's Medium (DMEM) (Gibco 11960, Invitrogen Co., Carlsbad, CA) with 15% v/v fetal bovine serum (FBS) (Gibco 10082, Invitrogen Co.), 4 mM L-glutamin (Invitrogen Co.), 0.1mM 2-mercapto-ethanol (Sigma-Aldrich Co.), 0.02% v/v sodium pyruvate (Sigma-Aldrich Co.), 100 U/ml penicillin (Invitrogen Co.), 100 U/ml streptomycin (Invitrogen Co.), and 1000 U/ml ESGRO (Invitrgoen Co.) which contains leukemia inhibitory factor (LIF). HepG2 hepatocellular carcinoma cell line was cultured in DMEM (Gibco 11965, Invitrogen Co.) with 10% v/v FBS (Gibco 10082, Invitrogen Co.), and 1% v/v antibiotic-antimicotic (Gibco 15240, Invitrogen Co.). DU145 and PC-3^{DsRed} prostate cancer cell were cultured in RPMI-1640 (Gibco 61870, Invitrogen Co.) with 10% v/v FBS (Gibco 10082, Invitrogen Co.), and 1% v/v antibiotic-antimicotic (Gibco 15240, Invitrogen Co.). HFOB human fetal osteoblasts were cultured in D-MEM/F-12 (Gibco 10565, Invitrogen Co.) with 10% v/v FBS (Gibco 10082, Invitrogen Co.), and 1% v/v antibiotic-antimicotic (Gibco 15240, Invitrogen Co.). MC3T3-E1

murine pre-osteoblasts were cultured in α-MEM (Alpha Minimum Essential Medium; Gibco A10490, Invitrogen Co.) supplemented with 15% (v/v) FBS (Gibco 10082, Invitrogen Co.), and 1% v/v antibiotic-antimicotic (Gibco 15240, Invitrogen Co.). Differentiation of MC3T3-E1 cells into osteoblasts was only induced when cultured as spheroids by addition of 50 μg/ml ascorbic acid. HUVEC human umbilical vein endothelial cells (Lonza) passage number 2-6 were cultured in endothelial growth medium-2 (EGM-2, Lonza). All the cells were cultured in a humidified incubator (37^{o}C in an atomosphere of 5% CO_2). Cell suspensions for the hanging drop experiments were made by dissociating cells with 0.25% trypsin-EDTA (Gibco 25200, Invitrogen Co.), centrifugation of dissociated cells at 1000 rpm for 5 minutes at room temperature, and re-suspended in growth media. Cell density was estimated using a hemocytometer.

4.2.5 Spheroid Formation, Co-culture Spheroid Formation, Concentric Layer Patterning, and Spheroid Transfer in the 384 Hanging Drop Array Plate

General mono-culture spheroid formation was performed as previously described in Chapter 3. Mixed co-culture spheroids were generated by first preparing mixed cell suspensions from the desired cell types at the specified ratios followed by the same hanging drop formation protocol for mono-culture spheroids. Concentric layer patterning of different cell types within a spheroid was achieved by initially forming a mono-culture spheroid of one cell type as the inner core. After one day, once the initial cell type aggregates, the single cell suspension of the second cell type was subsequently added to the existing hanging drop to form an exterior coating around the inner core. Spheroid transfer within the hanging drop plate for Janus spheroid (Torisawa *et al*. 2009) formation

or 3D cellular confrontation was achieved by direct pipetting to retrieve spheroid from the top of an access hole and then gently pipette into another existing hanging drop containing spheroid just like the removal and addition of liquid. Such spheroid transferring process was demonstrated by both manual pipetting and a liquid handling robot (CyBi-Well, CyBio Inc.).

4.3 Results and Discussion

4.3.1 Z'-factor and Z-factor of the 384 Hanging Drop Array Plate

Since one of the best applications of the 384 hanging drop plate is HTS for drug screening purposes, it is important to know the quality of various assays performed in the hanging drop plate. We adapted the calculation of Z'- and Z-factors as assay performance measures to validate the robustness of fluorescence- and colorimetric-based assays in the 384 hanging drop plate. Figure 4.1b and d summarize the Z'- and Z-factor calculations and comparisons for both the 384 hanging drop plate and the standard clear 384-well plate.

For fluorescence-based assays, Z-factors are all well-above 0.5 at all the fluorescein concentrations tested in the 384 hanging drop plate. This indicates that the fluorescence-based assays performed in the 384 hanging drop plate are excellent within the range of concentrations tested (Table 4.1). In addition, the Z-factors for the 384

hanging drop plate are all better or comparable to the Z-factors for the commercially available, standard, clear 384-well plate. The Z-factors are anticipated to be even better if the 384 hanging drop plates are made of solid black polystyrene with solid walls around each hanging drop access hole to segregate each drop. Typical fluorescence-based assays are performed in solid black polystyrene multi-well plates as the black walls can reduce well-to-well crosstalk and background for fluorescent assay. Nevertheless, the ability to conduct microscopy imaging would be compromised if the 384-well plates are made of solid black material. Various design considerations and complications must be carefully reviewed before making such a step.

For colorimetric-based assays, with the exception of the lowest two yellow food color percentages, all the other percentages have Z-factors above 0.5 in the 384 hanging drop plate. This indicates that the colorimetric-based assays performed in the 384 hanging drop plate are excellent within the 30% to 100% yellow food color solutions tested (Table 4.1). The plate reader might not be sensitive enough to read the absorbance at 10% and 20% yellow food color. As a result, a huge variation is generated in these low-value readouts, leading to low and even negative Z-factors. Caution must be used when performing colorimetric-assays in the plates involving such low absorbance values. Nevertheless, the Z-factors for the 384 hanging drop plate are still comparable to the Z-factors for the standard, clear 384-well plate at most yellow food color percentages tested.

It should also be noted that because the detection sensitivity, amount of cross-talk, and positional effects reflected in the plate reader readouts greatly depends on the make

and model of the microplate readers, the calculated Z'- and Z-factors will also change depending on the specific microplate reader used. One should be consistent (and careful in choosing) in plate reader usage throughout the entire experiment from the initial evaluation of the robustness of the assays (Z'- and Z-factor calculations) to performing the actual assays in HTS.

4.3.2 Droplet Stability in the Modified 384 Hanging Drop Array Plate

In order to culture spheroids over long periods of time, the hanging drops in the 384 hanging drop array plate must be kept stable over extended periods and should be robust against sudden perturbations. In the original 384 hanging drop array plate, hanging drops tend to spread out over time and drops tend to spread out upon experiencing disturbing sharp accelerations due to abrupt impulses. Once a droplet spreads out, the droplet becomes much more vulnerable to coalesce with neighboring drops. Recent works by Kalinin *et al*. (2008) showed that micro-topographical ring structures greatly enhance the stability of droplets without spreading out. Therefore, we tested the ability of different ring features added around existing bottom plateaus or the new trench designs (Table 4.2) to resist droplet spreading due to centripetal acceleration. Figure 4.3b summarizes the result. A bottom trench design with extra ring feature of 0.25 mm width and 0.50 mm height (Table 4.2, Design 20) was able to sustain the highest centripetal acceleration without droplet spreading out. It is interesting to note that a bottom trench design alone without a ring feature (Table 4.2, Design 11) is the worst in terms of preventing droplets from spreading out (Figure 4.3b). However, with the

addition of a ring structure around the trench (Designs 12 to 20), the stability of the hanging drops were greatly enhanced. Without the ring structure, droplets inside the trench easily spread out to the neighboring bottom surface of the plate. Whereas the ring structures provides a physical wall around the hanging drops to keep them stable. The combination of a trench design and ring structure further physically allows for a bigger volume of liquid to be held in the hanging drop and remain stable in place (as compared to the plateau design).

To prevent droplets from spreading out on the top surface of the plate, extra ring (extrusion) and trench (dent) design modifications around the top surface of the access holes were tested against droplet spreading out. Upon routine cell culture media exchange over the 8 days of incubation, some droplets will merge with undesired liquid remnants left by the pipette tips during media pipetting. Figure 4.3c shows the initial and final images of the actual test prototype plate. It is clear that the extra ring design out performs the trench design with no droplets spreading out on the top surface while the trench design has several droplets spreading out since initial droplet formation on Day 0. It is also intuitive that since there is no physical barrier around the trench designs, liquid tends to merge easily with remnants on the neighboring top surface once the surface becomes hydrophilic with the wetting of the pipette tips. While the extra ring design contrasts with the trench design by providing a wall to guide pipette tips directly into the access holes and preventing the hanging drop from merging with liquid remnants on the top surface. No significant difference was found between the different top ring dimensions. As the modified design parameters were finalized, the original plate mold

was refined to add additional ring structures to the top and bottom surfaces of the plate. However, due to the mold manufacture limitations, the final ring dimensions have to be compromised to 0.5 mm width and 0.5 mm height for both the top and the bottom in the original plateau structure (Figure 4.2e). It should also be noted that because the material used in the rapid prototypes is different from the clear polystyrene material used in the actual 384 hanging drop plates, the surface properties might be slightly different. This could lead to minor differences in the test results from the rapid prototypes and the actual plate.

The modified plate design with the added top and bottom ring features was manufactured by injection molding using the same clear polystyrene material as the original plates. The original plate was compared to the modified plate for droplet stability during routine cell culture and media exchange procedures. Figure 4.3d shows a summary of the number of droplets spread out in each plate over 14 days. The modified plate performs exceedingly better than the original plate in preventing droplets from spreading out. The modified plate has no droplets spreading out over the 14 days of culture, while the original plate already has 7 droplets spreading out from the top surface during initial hanging drop formation on Day 0. This demonstrates that the modified new plates are significantly enhanced in preventing droplets from spreading out in both the top and bottom surfaces. It is also interesting to note that between Day 6 and Day 8, there is a sharp increase in the number of droplets that have spread out in the original plate. This is most likely due to the coalescing of droplets leading to a chain effect. Because the 384 hanging drops are so closely spaced together, once a droplet spreads out,

it becomes very vulnerable to merge with neighboring drops, creating a larger droplet that is even more unstable. The modified plate with the extra ring structure around the bottom plateaus greatly prevents the initial drop from spreading out, thus enhancing the overall stability of the plate. The modified plate was subsequently shown to be stable with no droplets spreading out until Day 24 when 33 drops spread out. Additional four modified plates were also used in actual 3D spheroid culture experiments and were shown to be stable with no droplets spreading out throughout the extent of the 14-day experiment. In addition to enhancing droplet stability, each access hole in the modified plates also holds more liquid due to the extra volume generated from the extra top ring. This allows for bigger droplets to be more robust against physical perturbations, evaporation, and media osmolality shifts.

4.3.3 Biomedical Applications of the 384 Hanging Drop Array Plate

To allow more researchers to adapt the 384 hanging drop array plate for 3D spheroid culture, the platform must be versatile and applicable to a wide variety of studies. Here, we demonstrate several useful techniques made possible by the 384 hanging drop plate that would otherwise be difficult to perform utilizing other spheroid formation and culturing methods. We first demonstrate that 384 hanging drop array plate can be used to generate uniform mono-culture spheroids at various defined sizes from mouse embryonic stem (mES) cells (Figure 4.4a), HepG2 cells (Figure 4.4b), DU145 prostate cancer cells (Figure 4.5a), and HFOB human fetal osteoblasts (Figure 4.5b). Uniform pool of spheroids and spheroid sizes are controlled by introducing defined

numbers of cells to each hanging drop. Such uniformity control feature is often very tedious or not possible in conventional spheroid formation methods. Emerging micro-technologies for spheroid formation (Fukuda *et al*. 2006; Lee *et al*. 2010; Sakai and Nakazawa 2007; Toh *et al*. 2007; Torisawa *et al*. 2007; Ungrin *et al*. 2008; Wu *et al*. 2008) generally offer considerable improvements for spheroid uniformity control, but such custom-made delicate devices are often tedious to fabricate and requires specialized trainings to operate, and thus not readily available to the research community. The 384 hanging drop plate delivers the same advantage in a user-friendly manner.

Next, we show the ability of the hanging drop plate to form mixed co-culture spheroids with randomly-distributed cell types. Figure 4.6a shows the image of a mixed co-culture spheroid containing PC-3^{DsRed}, HUVEC, and MC3T3-E1 cell at 1:50:50 ratio. Formation of co-culture spheroids using conventional rotating bioreactors, non-adherent surfaces, or even sophisticated micro-wells does not ensure uniform incorporation of all co-culture cell types into the spheroids. Many times multiple types of spheroids comprised primarily of just one of the co-culture cell types rather than mixed co-culture spheroids were formed. The hanging drop method overcomes this issue by forcing all cell types to aggregate into single spheroid by gravity, making formation of mixed co-culture spheroids as simple as mono-culture spheroids. In addition, co-culture spheroids can also be patterned in concentric layers. Figure 4.6b demonstrates a PC-3^{DsRed} and MC3T3-E1 co-culture spheroid at 1:100 ratio with PC-3^{DsRed} cells preferentially patterned in the center core of the spheroid, as the exterior outside coating of the spheroid, or randomly distributed within the spheroid. Such concentric patterning of spheroids can

easily be manipulated using the 384 hanging drop plate by varying the timing and order of seeding the different cell type suspensions into the hanging drops.

Finally, we demonstrate that spheroids cultured in the 384 hanging drop plates can be easily retrieved and transferred to another existing hanging drop (Figure 4.6c). Figure 4.6d shows the before and after images of a green MC3T3-E1 spheroid being transferred to a red MC3T3-E1 spheroid. This process can be easily performed on the hanging drop plate by simple manual pipetting or pipetting by a robotic liquid handler from the top side of the plate. Such technique is useful in 3D confrontational studies or formation of Janus spheroids (given enough time for the two spheroids to merge) where cell-cell-interactions in 3D can be studied. In addition, spheroid transfer allows for 3D side-by-side patterning for tissue engineering purposes as well as differentiation studies of embryoid bodies co-cultured next to a second cell type. Furthermore, since spheroid retrieval from the plate is such a simple process, specific spheroids can also be harvested for subsequent analysis by histology, flow cytometry, Q-PCR, Western blot, and other molecular and cellular analysis.

4.4 Conclusion

We describe the characterization, improvements, and versatility of the 384 hanging drop array plate for HTS, long-term culture, and biomedical studies. The 3D spheroid culture platform offers excellent and robust assay performance required by HTS

in drug discovery and therapeutic development industries. The modified plate allows for extended long-term 3D spheroid culture in stable hanging drops. The 384 hanging drop plate is also compatible with a wide variety of cell types. Special spheroid manipulation techniques enabled by the platform to create different types of co-culture spheroids open up novel ways to study cancer biology, developmental biology, and tissue engineering in 3D. We believe the high-throughput hanging drop platform will be a valuable tool capable of revolutionizing current 3D cell culture standards in a wide range of disciplines.

Figure 4.1. **(a)** Concentration map in 384-format plate for fluorescein solution. **(b)** Bar graph showing the summary of Z-factors for fluorescence-based assay at various fluorescein concentrations. **(c)** Concentration map 384-format plate for yellow food color solution. **(d)** Bar graph showing the summary of Z-factors for colorimetric-based assay at various percentages of yellow food color.

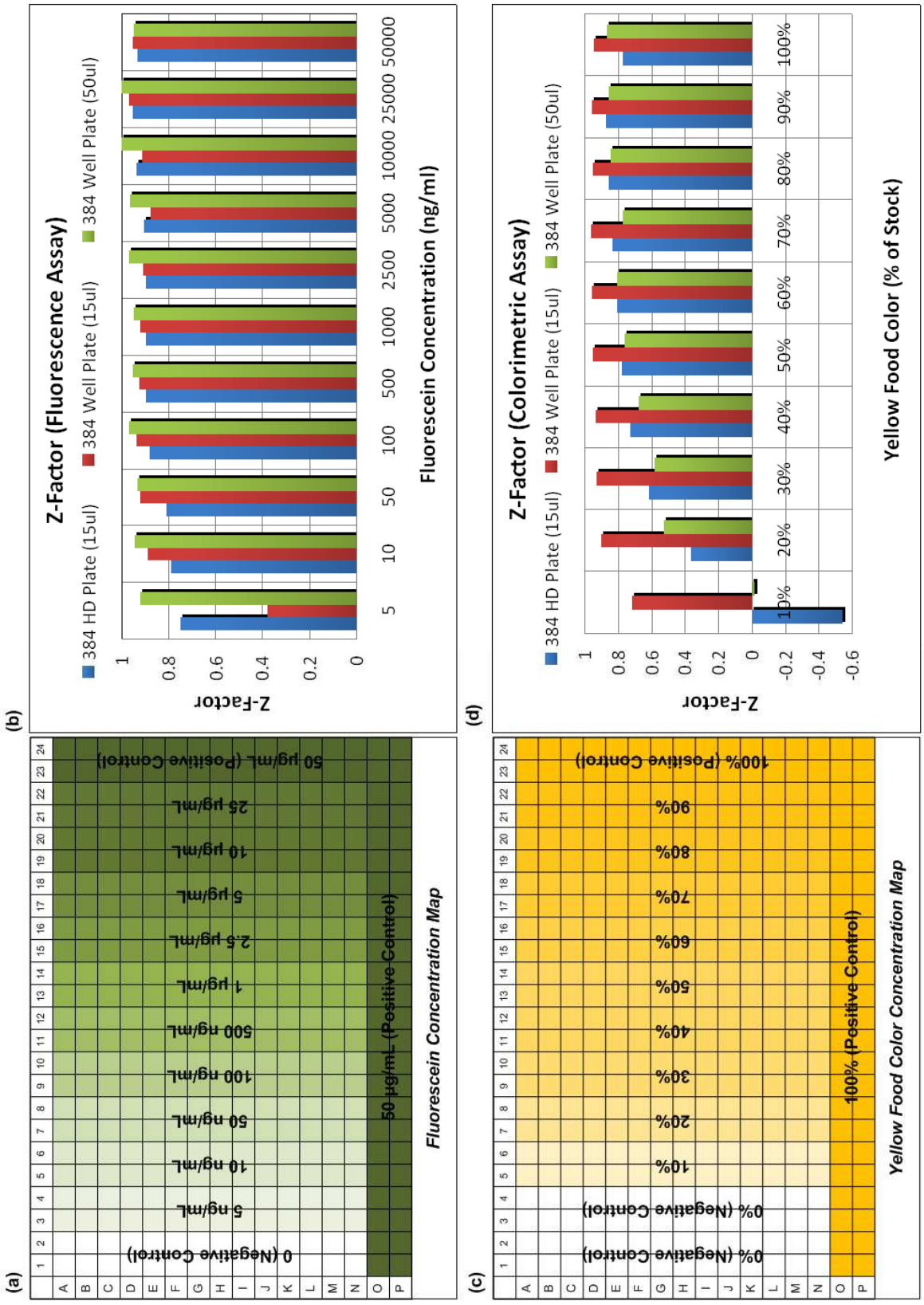
(a)
Fluorescein Concentration Map
0 (Negative Control)
5 ng/mL
10 ng/mL
50 ng/mL
100 ng/mL
500 ng/mL
1 µg/mL
2.5 µg/mL
5 µg/mL
10 µg/mL
25 µg/mL
50 µg/mL (Positive Control)
50 µg/mL (Positive Control)
(b)
Z-Factor (Fluorescence Assay)
384 HD Plate (15ul)
384 Well Plate (15ul)
384 Well Plate (50ul)
Z-Factor
Fluorescein Concentration (ng/ml)
(c)
Yellow Food Color Concentration Map
0% (Negative Control)
0% (Negative Control)
10%
20%
30%
40%
50%
60%
70%
80%
90%
100% (Positive Control)
100% (Positive Control)
(d)
Z-Factor (Colorimetric Assay)
384 HD Plate (15ul)
384 Well Plate (15ul)
384 Well Plate (50ul)
Z-Factor
Yellow Food Color (% of Stock)

Figure 4.1

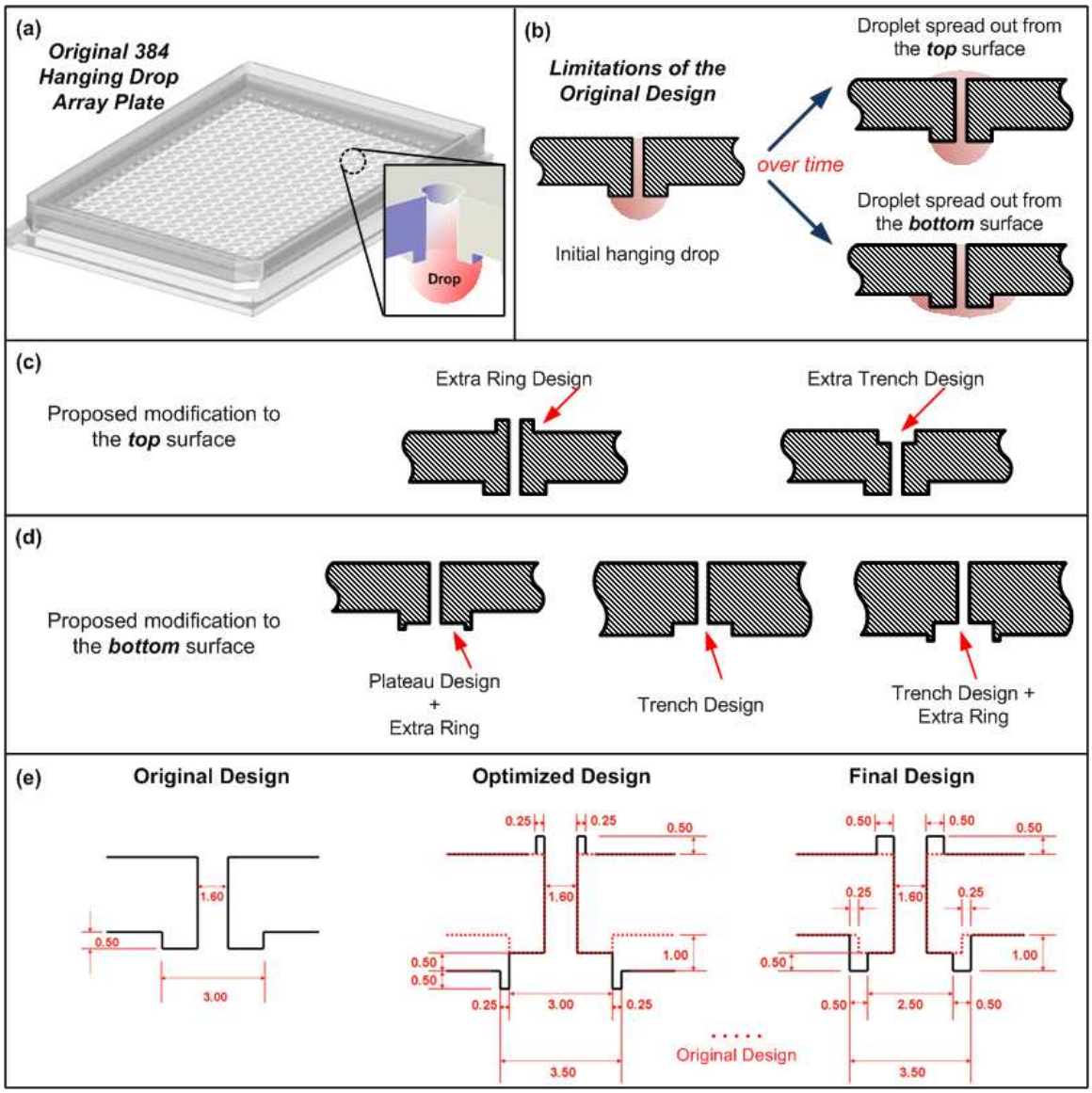

Figure 4.2. **(a)** Cartoon of the original 384 hanging drop array plate and its cross-sectional view with a hanging drop schematic drawing. **(b)** Illustration of a cross-sectional view of a hanging drop in an access hole of the 384 hanging drop plate and how the droplet spreads out from the top and bottom surfaces of the plate over time. **(c)** Cartoon showing the cross-sectional views of the proposed modifications to the top surface of the plate—an extra ring structure or a trench structure around the access hole. **(d)** Cartoon showing the cross-sectional views of the proposed modifications to the bottom surface of the plate—an extra ring structure to the existing plateau, a new trench structure, or a new trench with an extra ring structure. **(e)** Cross-sectional schematics of the original design, the optimized design, and the final modified design of a hanging drop site in the 384 hanging drop array plate with the key dimensions shown in millimeters (mm).

Figure 4.3. **(a)** Schematic of how the 384 hanging drop array prototype plates are tested on the spin coater with a glass slide attached to the underside of the plate to achieve a flat surface. Representative hanging drops and their corresponding radii to the center of the spindle are also illustrated. **(b)** Bar graph summarizing the maximum centripetal force a hanging drop could withstand before spreading out under different plate designs. **(c)** Day 0 and Day 8 (final day) photos of the top surface of the 384 hanging drop array prototype plate with different dimensions of the extra ring and trench designs. The enlarged Day 8 photo highlights droplets spreading out in the trench designs but not the ring designs. **(d)** Graph of cell culture media hanging drops spreading out condition in the original and the newly modified (additional top and bottom rings) 384 hanging drop array plate over time.

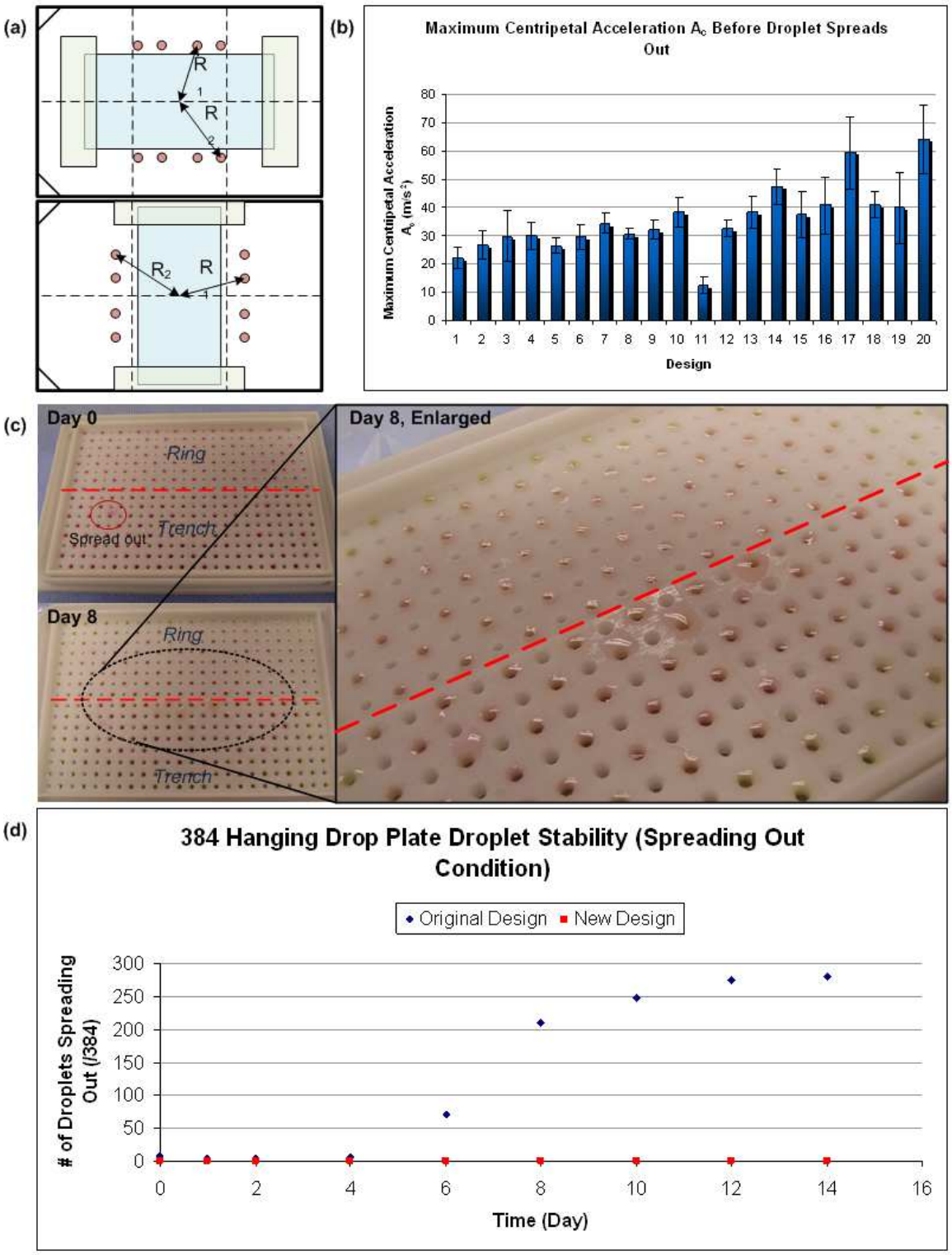
(a)
R
1
R
2
R2
R
1
(b)
Maximum Centripetal Acceleration Ac Before Droplet Spreads Out
Maximum Centripetal Acceleration Ac (m/s2)
0
10
20
30
40
50
60
70
80
1 2 3 4 5 6 7 8 9 10 11 12 13 14 15 16 17 18 19 20
Design
(c)
Day 0
Ring
Trench
Spread out
Day 8
Ring
Trench
Day 8, Enlarged
(d)
384 Hanging Drop Plate Droplet Stability (Spreading Out Condition)
Original Design
New Design
# of Droplets Spreading Out (/384)
0
50
100
150
200
250
300
0 2 4 6 8 10 12 14 16
Time (Day)

Figure 4.3

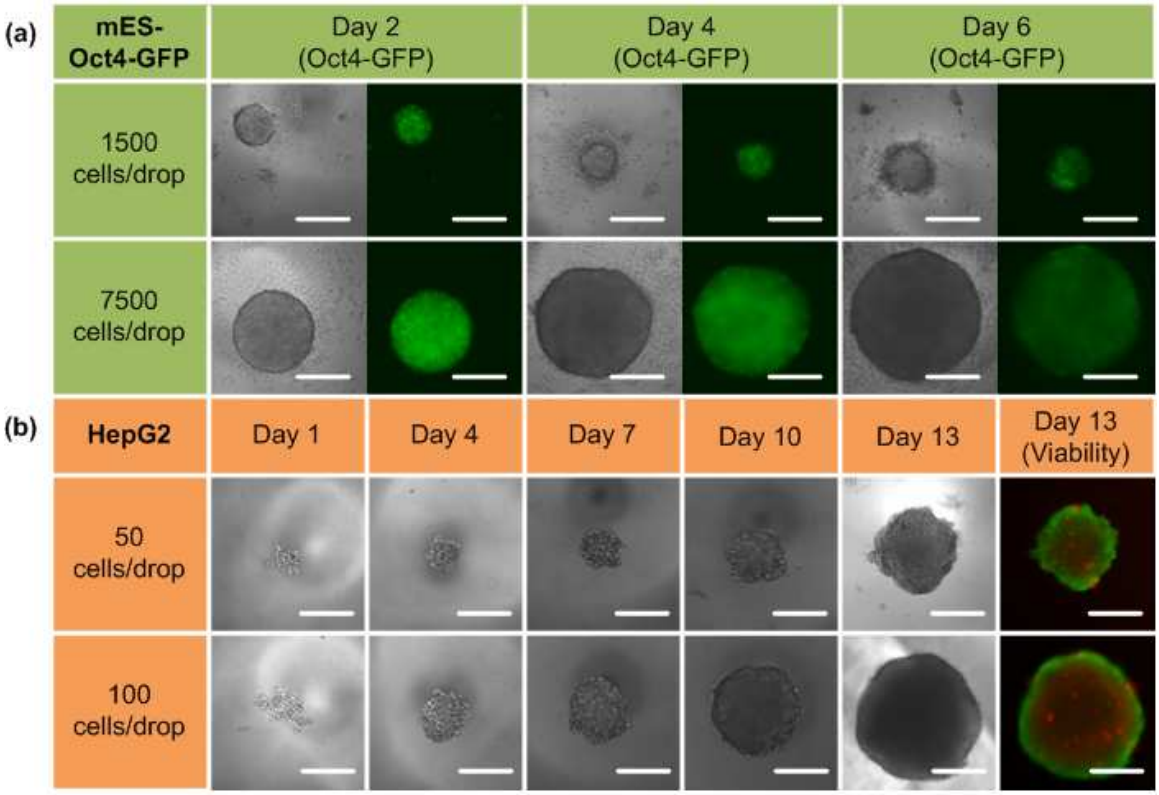

Figure 4.4. **(a)** Time-lapse images of mES-Oct4-GFP cell embryoid bodies cultured in the 384 hanging drop array plate at two initial seeding densities. **(b)** Time-lapse images of HepG2 cell spheroids cultured in the 384 hanging drop array plate at two initial seeding densities. Scale bare is 200 μm.

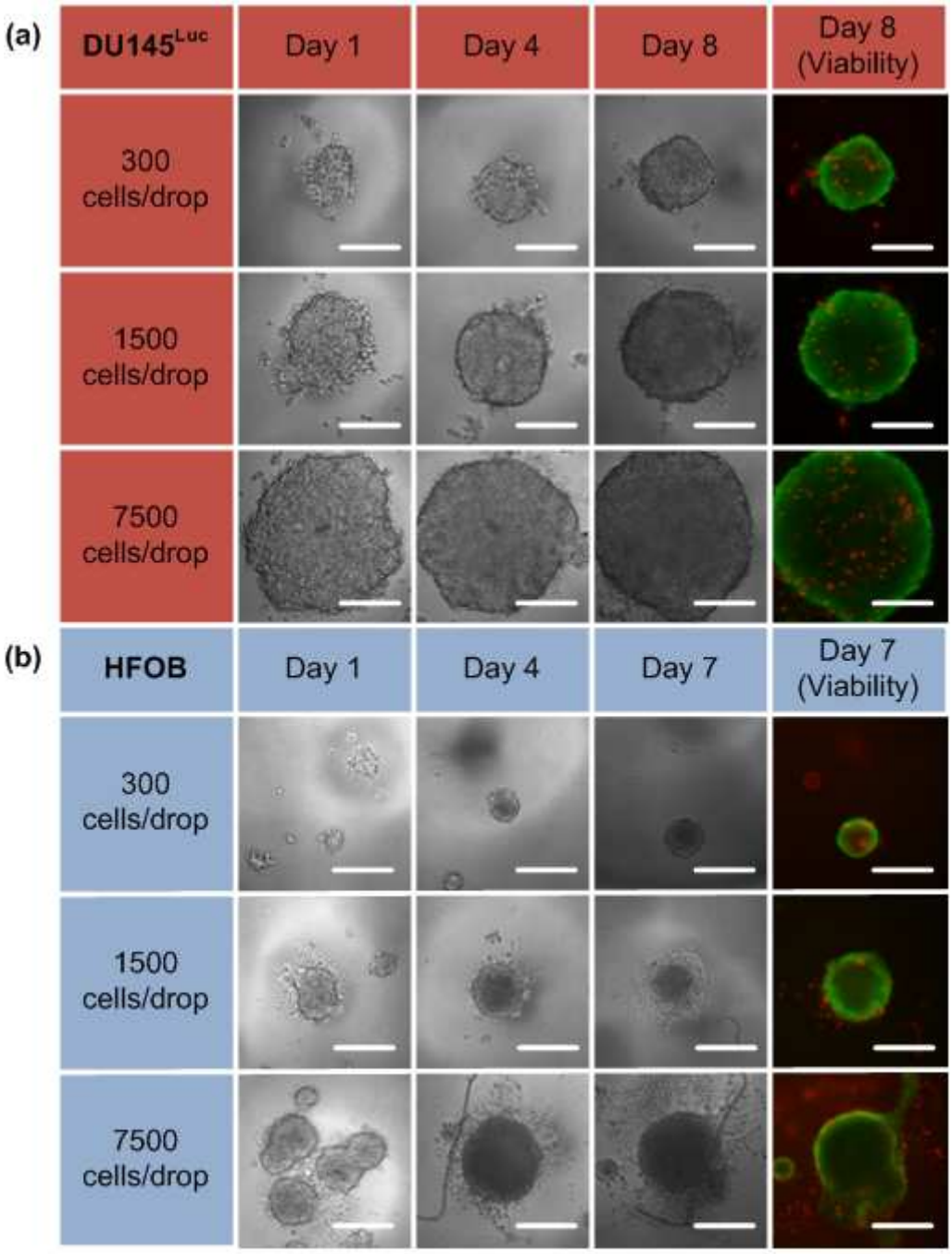

Figure 4.5. (a) Time-lapse images of DU145^{Luc} prostate cancer spheroids cultured in the 384 hanging drop array plate at three initial seeding densities. **(b)** Time-lapse images of HFOB spheroids cultured in the 384 hanging drop array plate at three initial seeding densities. Scale bare is 200 μm.

Figure 4.6. **(a)** Phase and fluorescent images of a PC-3^{DsRed}, HUVEC, MC3T3-E1 (1:50:50 ratio) mixed co-culture spheroid. **(b)** Images of PC-3^{DsRed} and MC3T3-E1 (1:100 ratio) co-culture spheroids with PC-3^{DsRed} cells preferentially patterned in the center, exterior, or randomly distributed. **(c)** Cartoon illustrating the process of spheroid transfer between hanging drops in the 384 hanging drop array plate. **(d)** Actual images of CellTracker Red- and Green-labeled MC3T3-E1 spheroids before and after transfer between hanging drops in the 384 hanging drop array plate. Scale bare is 200 μm.

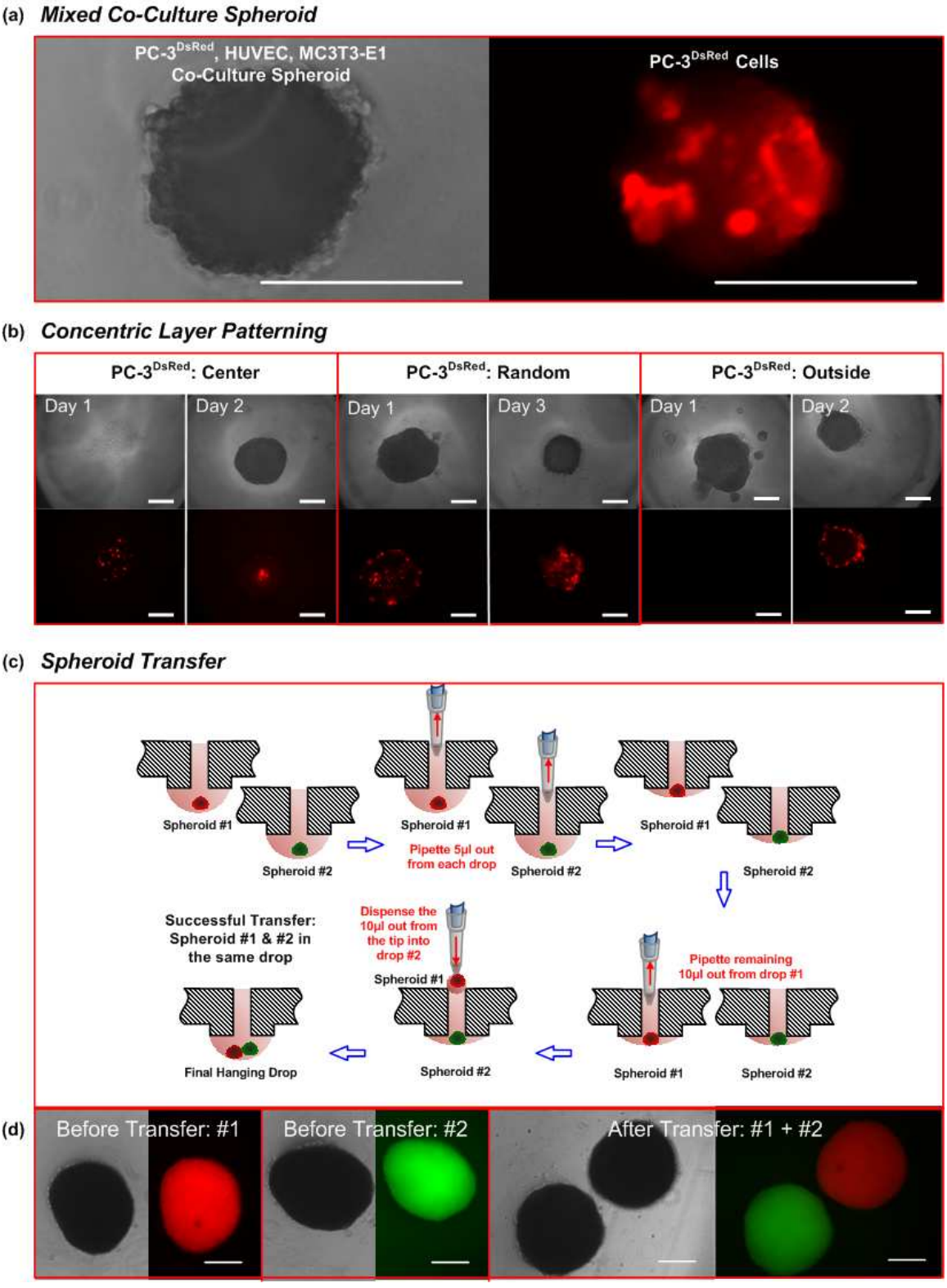
(a) Mixed Co-Culture Spheroid
PC-3DsRed, HUVEC, MC3T3-E1 Co-Culture Spheroid
PC-3DsRed Cells
(b) Concentric Layer Patterning
PC-3DsRed: Center
PC-3DsRed: Random
PC-3DsRed: Outside
Day 1
Day 2
Day 1
Day 3
Day 1
Day 2
(c) Spheroid Transfer
Spheroid #1
Spheroid #2
Pipette 5µl out from each drop
Spheroid #1
Spheroid #2
Spheroid #1
Spheroid #2
Successful Transfer: Spheroid #1 & #2 in the same drop
Dispense the 10µl out from the tip into drop #2
Spheroid #1
Pipette remaining 10µl out from drop #1
Final Hanging Drop
Spheroid #2
Spheroid #1
Spheroid #2
(d)
Before Transfer: #1
Before Transfer: #2
After Transfer: #1 + #2

Figure 4.6

Z'-Factor & Z-Factor Categorization of Screening Assay Quality		
$Z'\text{-Factor} = 1 - (3\sigma_{hc} + 3\sigma_{lc}) / \lvert \mu_{hc} - \mu_{lc} \rvert$	$Z\text{-Factor} = 1 - (3\sigma_{s} + 3\sigma_{c}) / \lvert \mu_{s} - \mu_{c} \rvert$	
Z-Factor or Z'-Factor Value	**Structure of Assay**	**Assay Quality**
1	SD = 0 (no variation), or the dynamic range → ∞	Ideal
1 > Z ≥ 0.5	Separation band is large	Excellent
0.5 > Z > 0	Separation band is small	Doable
0	No separation band; the sample signal variation and control signal variation bands touch	Yes/No
< 0	No separation band; the sample signal variation and control signal variation bands overlap	Unacceptable

Table 4.1. Summary of the implications of Z'-Factor and Z-Factor

Dimensions of the Bottom Structures in the 384 Hanging Drop Array Prototype Plates

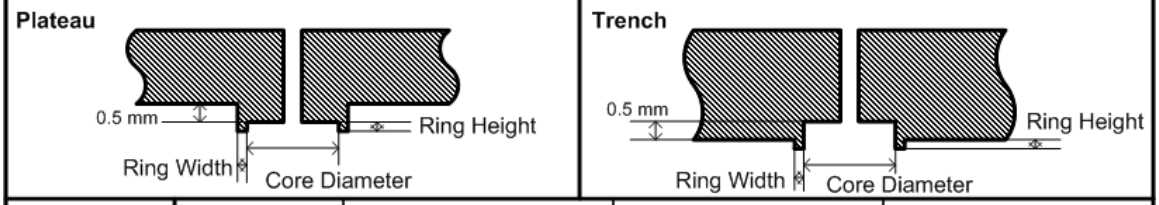

	Design	Core Diameter (mm)	Ring Height (mm)	Ring Width (mm)
Plateau	1 (Original)	3.00	0	0
	2	2.50	0.10	0.25
	3	2.50	0.25	0.25
	4	2.50	0.50	0.25
	5	2.75	0.10	0.25
	6	2.75	0.25	0.25
	7	2.75	0.50	0.25
	8	3.00	0.10	0.25
	9	3.00	0.25	0.25
	10	3.00	0.50	0.25
Trench	11	3.00	0	0
	12	2.50	0.10	0.25
	13	2.50	0.25	0.25
	14	2.50	0.50	0.25
	15	2.75	0.10	0.25
	16	2.75	0.25	0.25
	17	2.75	0.50	0.25
	18	3.00	0.10	0.25
	19	3.00	0.25	0.25
	20	3.00	0.50	0.25

Table 4.2. List of the specific dimensions of the different bottom surface structure designs in the 384 hanging drop array prototype plates

Dimensions of the Top Structures in the 384 Hanging Drop Array Prototype Plates

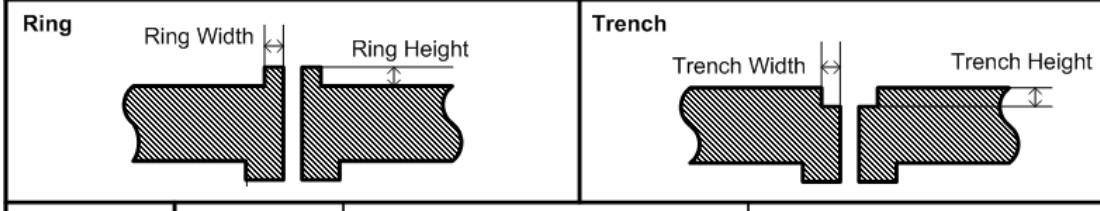

	Design	Height (mm)	Width (mm)
Ring	1	0.25	0.25
	2	0.50	0.25
	3	0.25	0.50
	4	0.50	0.50
Trench	5	0.25	0.25
	6	0.50	0.25
	7	0.25	0.50
	8	0.50	0.50

Table 4.3. List of the specific dimensions of the different top surface structure designs in the 384 hanging drop array prototype plate

4.5 References

1. Birmingham A, Selfors LM, Forster T, Wrobel D, Kennedy CJ, Shanks E, et al. Statistical methods for analysis of high-throughput RNA interference screens. Nat Methods 2009;6(8):569-75.

2. Friedrich J, Seidel C, Ebner R, Kunz-Schughart LA. Spheroid-based drug screen: considerations and practical approach. Nat Protoc 2009;4(3):309-24.

3. Fukuda J, Khademhosseini A, Yeo Y, Yang X, Yeh J, Eng G, et al. Micromolding of photocrosslinkable chitosan hydrogel for spheroid microarray and co-cultures. Biomaterials 2006;27(30):5259-67.

4. Hirschhaeuser F, Menne H, Dittfeld C, West J, Mueller-Klieser W, Kunz-Schughart LA. Multicellular tumor spheroids: an underestimated tool is catching up again. J Biotechnol 2010;148(1):3-15.

5. Kalinin Y, Berejnov V, Thorne RE. Controlling microdrop shape and position for biotechnology using micropatterned rings. Microfluid Nanofluidics 2008;5(4):449-54.

6. Kunz-Schughart LA, Freyer JP, Hofstaedter F, Ebner R. The use of 3-D cultures for high-throughput screening: the multicellular spheroid model. J Biomol Screen 2004;9(4):273-85.

7. Lee WG, Ortmann D, Hancock MJ, Bae H, Khademhosseini A. A hollow sphere soft lithography approach for long-term hanging drop methods. Tissue Eng Part C Methods 2010;16(2):249-59.

8. Lin RZ, Chang HY. Recent advances in three-dimensional multicellular spheroid culture for biomedical research. Biotechnol J 2008;3(9-10):1172-84.

9. Sakai Y, Nakazawa K. Technique for the control of spheroid diameter using microfabricated chips. Acta Biomater 2007;3(6):1033-40.

10. Shields K, Ackland ML, Ahmed N, Rice GE. Multicellular spheroids in ovarian cancer metastases: Biology and pathology. Gynecol Oncol 2009;113(1):143-8.

11. Sittampalam GS, Iversen PW, Boadt JA, Kahl SD, Bright S, Zock JM, et al. Design of signal windows in high throughput screening assays for drug discovery. J Biomol Screen 1997;2(72):159-69.

12. Sui Y, Wu Z. Alternative statistical parameter for high-throughput screening assay quality assessment. J Biomol Screen 2007;12(2):229-34.

13. Toh YC, Zhang C, Zhang, J, Khong YM, Chang S, Samper VD, et al. A novel 3D mammalian cell perfusion-culture system in microfluidic channels. Lab Chip 2007;7(3):302-9.

14. Torisawa Y, Chueh BH, Huh D, Ramamurthy P, Roth TM, Barald KF, et al. Efficient synchronous formation of uniform-sized embryoid bodies using a compartmentalized microchannel device. Lab Chip 2007;7(6):770-6.

15. Torisawa Y, Mosadegh B, Luker GD, Morell M, O'Shea KS, Takayama S. Microfluidic hydrodynamic cellular patterning for systematic formation of co-culture spheroids. Integr Biol 2009;1(11-12):649-54.

16. Ungrin MD, Joshi C, Nica A, Bauwens C, Zandstra PW. Reproducible, ultra high-throughput formation of multicellular organization from single cell suspension-derived human embryonic stem cell aggregates. PLoS ONE 2008;3(2):e1565.

17. Wu LY, DiCarlo D, Lee LP. Microfluidic self-assembly of tumor spheroids for anticancer drug discovery. Biomed Microdev 2008;10(2):197-202.

18. Yamada KM, Cukierman E. Modeling tissue morphogenesis and cancer in 3D. Cell 2007;130(4):601-10.

19. Zhang JH, Chung TD, Oldenburg KR. A simple statistical parameter for use in evaluation and validation of high throughput screening assays. J Biomol Screen 1999;4(2):67-73.

CHAPTER 5

Elucidating the Biology of CD133^{+} Prostate Cancer Cells and Its Relationship to Tumor Dormancy

Since the finding of the quiescent behavior of the CD133^{+} PC-3^{DsRed} cells in the co-culture spheroid model reported in Chapter 2, the intuitive next step is to verify whether and how the quiescence of these CD133^{+} PC-3^{DsRed} cells helps maintain their CD133 marker and keeps them "stem"-like. This chapter describes efforts to explore the underlying molecular mechanisms that are governing the CD133^{+} PC-3^{DsRed} cells in more depth by looking at their expression of key genes implicated in stem cell self-renewal, quiescence, homing, and localization. The findings from these studies would provide insights and serve as the basis for subsequent construction of a reporter system to allow real-time tracking of the CD133 expression in the PC-3 cells within the 3D co-culture constructs. In addition to the prostate cancer cell proliferation data presented in Chapter 2, we also took a step further to evaluate the quiescence of the prostate cancer cells cultured in the co-culture spheroids by looking at their cell cycling stage. Here, we present preliminary data on current findings in the relevant stem cell gene expression profiles in the CD133^{+} subpopulation of PC-3 cells and the cell cycling stage of prostate cancer cells. Additional efforts are required to elucidate the underlying mechanisms in keeping the CD133^{+} cells quiescent and thus maintaining their stem-like markers at the molecular level.

5.1 Introduction

5.1.1 Prostate Cancer Stem Cells

Cancer stem cells (CSCs) contain genetic changes that define them as cancer cells; but unlike the bulk tumor population, they are not genetically unstable (Reya *et al*. 2001). Animal studies have showed that these small number (less then 2%) of CSCs within the tumor mass are the essential ones responsible for continual tumor growth and metastasis (Al-Hajj *et al*. 2003). This implies that the "non-stem" majority of cancer cells in a tumor are not critical to target for treatment as they are genetically unstable and have limited ability to metastasize and grow. Rather, CSCs' lack of genetic instability represents a unique point of vulnerability, and therefore they are the essential targets to destroy to prevent cancers from metastasizing and killing the patients. Therefore, establishing a method to enrich, maintain, and monitor these CSCs *in vitro* will be vital and powerful in future fundamental CSC biological studies and novel anti-cancer therapeutic developments.

Recent studies have demonstrated the presence of CSCs in solid tumors such as breast, brain, pancreas, colon, and prostate cancers (Al-Hajj *et al*. 2003; Calabrese *et al*. 2007; Ricci-Vitani *et al*. 2009; Cho and Clarke 2008; Ailles and Weissman 2007). But the true identity of prostate CSCs has yet to be definitively defined. Currently, prostate CSCs have been identified as the subpopulation of prostate cancer cells carrying the surface marker phenotype of $CD44^{+}/\alpha_2\beta_1^{hi}/CD133^{+}$ (Collins *et al*. 2005). Specifically,

we have isolated the $CD133^+$ subpopulation from the metastatic prostate cancer PC-3 cell line, which is believed to be more "progenitor-like." These cells have been shown to generate clones of additional stem cells as well as regenerating the heterogeneous population observed in the original tumor when passaged in mice. However, it has not been possible to maintain and grow these cells *ex vivo*. Several challenges that make the study and designs of therapies against them nearly impossible include: i) they can only be isolated in small numbers; and ii) they are very difficult to grow *in vitro* because the isolated CSCs undergo spontaneous programmed differentiation in *in vitro* cultures. Nevertheless, various CSC populations have been reported to be enriched and maintained in sphere cultures (Hirschhaeuser *et al*. 2010). Recent studies have shown that CSCs from colorectal and brain cancers can only be maintained in 3D culture under serum-free conditions; whereas culturing of the CSCs under standard 2D monolayer conditions with serum-containing media led to loss of self-renewal, tumorigenic potential, and differentiation capabilities (Ricci-Vitiani *et al*. 2007; Lee *et al*. 2006). As a result, culturing CSCs as conventional 2D monolayers is not a viable approach as *in vitro* models for developments of novel therapeutics. To improve the current treatments and broaden the existing knowledge about cancer, it is crucial to develop cancer models involving these CSCs that possess the potent ability to regenerate tumors.

5.1.2 Nest Parasitism Hypothesis and Tumor Dormancy

Normal stem cells typically reside in microenvironmental niches in which cell fate decisions are regulated by surrounding cells, ECM components, and secreted local

and systemic factors (Dontu *et al*. 2005). Likewise, CSCs are also likely to be maintained in a niche (Ailles and Weissman 2007). In particular, several properties of prostate CSCs include: i) unlimited capacity for self-renewal; ii) use of the stromal derived factor-1 (SDF-1 or CXCL12) and its receptors CXCR4 or CXCR7 for migration and metastasis; iii) resistance to apoptosis and therapeutic agents targeting proliferating cells; iv) requirement for a specific microenvironment or niche to grow. Interestingly, these characteristics are in direct parallel with normal HSCs properties.

For prostate cancer, bone is the most common metastatic site; it provides various chemotactic, adhesion, and growth factors for prostate cancer to target and proliferate (Shiozawa *et al*. 2008). Recently, it has been hypothesized that the prostate cancer bone metastasis process is very much similar to the migration and homing behavior of HSCs to the bone marrow niche (Shiozawa *et al*. 2008, 2010, 2011). Given the complicated yet well-programmed process of HSCs self-renewal, proliferation, and differentiation, they must be tightly regulated within a physical locale, the HSC "niche" (Shiozawa *et al*. 2008). The HSC niche that regulates HSC homing, quiescence, and self-renewal is believed to be primarily comprised of osteoblastic (endosteal niche) and endothelial (vascular niche) cells as key components (Shiozawa *et al*. 2008). Critical molecules such as chemoattractants (stromal derived factor-1, SDF-1 or CXCL12), attachment factors (annexin II or Anxa2), and regulators of cell growth involved in HSC niche selection are also thought to be used by prostate cancer metastases to the bone. Once prostate cancer cells home to the bone marrow, they parasitize the bone microenvironment to regulate

their long-term survival, dormancy, and ultimately metastatic growth (Figure 5.1). Recently, Shiozawa *et al*. have proven this concept (Shiozawa *et al*. 2008, 2010, 2011).

In a mouse model of metastasis, disseminated human prostate cancer cells from primary tumors directly compete with HSCs for occupancy of the HSC niche (Shiozawa *et al*. 2011). HSCs and prostate cancer cells also colocalize to the endosteal bone surfaces of the bone marrow niches both *in vivo* and *in vitro* (Shiozawa *et al*. 2011). Initially, like HSCs, prostate cancer cells utilize the CXCR4/SDF-1 pathway to migrate and gain access to the bone marrow during metastasis to the bone (Sun *et al*. 2003, 2005., Wang *et al*. 2008). Engagement of SDF-1 receptors on PCa cells subsequently leads to increased expression of the adhesive-localization molecule annexin II, which has been shown to bind both PCa cells and HSCs to osteoblasts in the endosteal niche (Shiozawa *et al*. 2008; Taichman *et al*. 2007). Altogether, these findings suggest that factors from the HSC niche are critical in the osteotropism of prostate cancer metastasis to the bone.

The role of the HSC niche (in particular, the endosteal or osteoblast niche) is also thought to induce and maintain HSC quiescence (dormancy) and regulate differentiation (Shiozawa *et al*. 2010, 2011). Since metastatic PCa cells occupy the same niche as HSCs, it is likely that the molecules involved in the induction of HSC dormancy also induce dormancy in metastatic PCa cells. Shiozawa *et al*. have showed that the GAS6/AXL axis plays a critical role in regulating the quiescence and survival of prostate cancer in the HSC niche (Shiozawa *et al*., 2010). Specifically, it was first demonstrated that the binding of prostate cancer cells to annexin II induces the expression of GAS6 receptor

AXL in prostate cancer cells (Shiozawa *et al*., 2010). AXL binding to GAS6 produced by osteoblasts inhibited prostate cancer cell proliferation and induces quiescence of prostate cancer cells as shown by an increased fraction of cells in the G_0 cell cycle state and a decreased fraction in the G_1 and S/M/G_2 states (Shiozawa *et al*., 2010). Based on these data, it is likely that the activation of GAS6 receptor AXL on the metastasized prostate cancer cells in the marrow environment plays a critical role as a molecular switch to establish dormancy and thus protects prostate cancer cells from chemotherapy. As a result, these mechanisms together support the concept that metastatic prostate cancer cells target the HSC niche during metastasis and serve as molecular parasites of the HSC niche by hijacking the normal machinery in the niche to facilitate their survival, dormancy, and growth.

Based on the nest parasitism hypothesis, we have already adapted 3D spheroid culture to engineer *in vitro* 3D prostate cancer bone micrometastases from the $CD133^+$ PC-3^{DsRed} cells as innovative co-culture constructs in an effort to maintain their progenitor cell properties in Chapter 2. We showed that the $CD133^+$ PC-3^{DsRed} subpopulation was relatively quiescent when cultured in co-culture spheroids with endothelial cells and osteoblasts. Because the $CD133^+$ PC-3^{DsRed} did not divide but remained dormant, it is very likely that their CD133 marker was also maintained. Here, we describe efforts to develop a reporter system to allow tracking of prostate cancer progenitor cell properties in real-time by correlating the CD133 marker of PC-3 cells to the expression of key genes relevant in stem cell self-renewal, quiescence, migration, and localization. Specifically, the genes we looked at include Bmi-1, a gene implicated in

stem cell self-renewal regulation, and its downstream target Ink4a (Park *et al*. 2004; Iwama *et al*. 2004; Lessard and Sauvageau 2003). Additionally, we looked at the expression of the two important receptors for SDF-1—CXCR4 and CXCR7, which are essential elements in the migration and homing of hematopoietic stem cells (HSCs) and prostate cancer metastasis to the bone marrow niche (Sun *et al*. 2003, 2005., Wang *et al*. 2008). The expression of Annexin II receptor (Anxa2R) that plays a significant role in the binding and localization of prostate cancer cells to the osteoblasts in the bone marrow niche (Shiozawa *et al*. 2008) was also investigated. Finally, we explored the expression levels of three receptors for GAS6—the AXL family of receptor tyrosine kinases (AXL, Sky, and Mer), which are regulators of cell growth and quiescence in the hematopoietic system as well as prostate cancer metastasis to the bone (Shiozawa *et al*. 2010). These essential genes implicated in HSCs and metastatic prostate cancer cells are expected to be up-regulated in the subpopulation of prostate cancer cells enriched for CSCs.

Since the eventual goal of establishing an accurate *in vitro* model of prostate cancer bone metastasis niche containing dormant prostate CSCs is to use it as a basis for the development of novel types of anti-cancer therapy, we transferred the culture of the PC-3 co-culture spheroids from the microfluidic device mentioned in Chapter 2 to the high-throughput hanging drop platform developed in Chapter 3. The characterization of PC-3 growth rate in the 3D co-culture spheroids maintained in the 384 hanging drop plate was also performed. To confirm the quiescent behavior of the prostate cancer cells observed in Chapter 2, we also initiated studies to explore the cell cycling stage of prostate cancer cells cultured in the 3D co-culture spheroids

5.2 Materials and Methods

5.2.1 General Cell Culture

PC-3^{DsRed} metastatic prostate cancer cells stably transfected with DsRed), human umbilical vein endothelial cells (HUVECs), and MC3T3-E1 mouse pre-osteoblasts are cultured and maintained as described in Chapter 2, Section 2.2.1—General Cell Culture. PC-3$^{Luc\ \ GFP}$ (mesenchymal PC-3 cells that have already undergone epithelial-mesenchymal transition (EMT), and stably transfected with luciferase and GFP) and PC-3$^{Luc\ E\ GFP}$ (epithelial PC-3 cells that have not undergone EMT, and stably transfected with luciferase and GFP) are cultured in the same way as PC-3^{DsRed} cells.

5.2.2 PC-3^{DsRed} CD133^{+} Cell Sorting

PC-3^{DsRed} CD133^{+} and CD133^{-} cells were isolated using CD133 Cell isolation kit, according to the manufacturer's protocol (Miltenyl Biotec) as described in Chapter 2, Section 2.2.7—PC-3^{DsRed} CD133^{+} Cell Sorting.

5.2.3 CD44 and Annexin II Receptor Subpopulations Cell Sorting

PC-3^{DsRed} CD133^{+} and CD133^{-} subpopulations of cells are further sorted for CD44^{+} and CD44^{-} subpopulations (Figure 5.3a), or Anxa2R^{+} and Anxa2R^{-} subpopulations (Figure 5.3a) using FACS Vantage dual-laser flow cytometer (Becton Dickinson) following staining with anti-Human CD44 antibodies (BD Pharmingen, San Diego, CA) or anti-Anxa2R antibodies. Annexin II p11 peptides (S100A10 (human) Recombinant Protein, Thermo Scientific, Rockford, IL) were used as antibodies for Anxa2R because Anxa2R was previously shown to bind to the p11 subunit of Annexin II (Lu *et al*. 2006). Annexin II p11 peptides were labeled with fluorescent dye prior to flow sorting using Alexa Fluor® 488 Microscale Protein Labeling Kit (A30006, Molecular Probes, Eugene, OR) according to manufaturer's protocol. PC-3^{DsRed} cells were then sorted for Anxa2R^{+} and Anxa2R^{-} subpopulations using these fluorescent (Alexa Fluor® 488) conjugated p11 peptides.

5.2.4 RNA Extraction and QRT-PCR

QRT-PCR was performed using standard techniques. Total RNA was isolated using RNeasy Mini Kit (Qiagen, Valencia, CA), and first-strand complementary DNA (cDNA) was synthesized with 0.8 μg of total RNA in a 40 μl reaction volume. Reverse transcript products were analyzed by QRT-PCR in TaqMan Gene Expression Assays of several target genes including Bmi-1, Ink4a, CXCR4, CXCR7, Anxa2R, AXL, Sky, Mer, and β-Actin (Applied Biosystems, Foster City, CA). QRT-PCR analysis was carried out using 15.0 μl of TaqMan Universal PCR Master Mix (Applied Biosystems), 1.5 μl of TaqMan Gene Expression Assay, 1 μl of cDNA, and 12.5 μl of RNAse/DNAse-free

water in a total volume of 30 μl. Negative controls were reactions without template. The initial single cycle of 95°C for 15 minutes to activate the Taq polymerase was followed by 40 cycles of second step PCR (95°C for 30 seconds and 60°C for 1 minute). The PCR product was detected as an increase in fluorescence using an ABI PRISM 7700 sequence detection system (Applied Biosystems). RNA quantity (C_R) was normalized to the housekeeping gene β-Actin control by using the formula $C_R = 2^{(40 - Ct \text{ of sample}) - (40 - Ct \text{ of control})}$. The threshold cycle ($C_t$) is the cycle at which a significant increase in fluorescence occurs.

5.2.5 Formation and Culture of PC-3^{DsRed}, PC-3$^{Luc\ GFP}$, and PC-3$^{Luc\ E\ GFP}$ Co-culture Spheroids with HUVEC and MC3T3-E1 Cells in the 384 Hanging Drop Array Plate

Cell suspensions for the hanging drop experiments were made by dissociating cells with 0.25% trypsin-EDTA (Gibco 25200, Invitrogen Co.), centrifugation of dissociated cells for 5 minutes, and re-suspended in the complete growth media of the specific cell types. Cell densities of each cell type were estimated using a hemocytometer. PC-3^{DsRed} (or PC-3$^{Luc\ GFP}$ or PC-3$^{Luc\ E\ GFP}$), HUVEC, and MC3T3-E1 heterogeneous cell suspension was then pre-mixed at 1:50:50 ratio prior to seeding in the 384 hanging drop array plate. Consequently, the co-culture media consists of PC-3 complete growth media, HUVEC endothelial growth medium-2 (EGM-2), and MC3T3-E1 complete growth media at 1:50:50 ratio, and supplemented with 50 μg/ml ascorbic acid.

The pre-mixed heterogeneous cell suspension was subsequently formed into hanging drops in the second generation modified 384 hanging drop array plates described in Chapter 4. The hanging drop formation process was carried out using the standard protocol as previously described in Chapter 3 with a minor increase in the hanging drop volume to accommodate the larger volume allowed by the second generation plates. Briefly, on the spheroid culture plate, a 20 μl heterogeneous cell suspension was dispensed into the bottom surface of the access hole at each cell culture site to form a hanging drop. In order to prevent evaporation, 4 ml of distilled water was added into the peripheral water reservoir. In addition, the plate was sandwiched by a 96-well plate lid and plate filled with distilled water, and wrapped in Parafilm. The growth media was exchanged every other day by taking 8 μl of media from a drop, and adding 10 μl of fresh co-culture media into a drop to account for minor evaporation of the original drop. 1200-cell co-culture spheroids were formed for the PC-3 proliferation experiments; and 3000-cell co-culture spheroids were formed for the subsequent cell cycling stage analysis (to ensure enough PC-3 cells for analysis by flow cytometry).

5.2.6 PC-3^{DsRed} Proliferation Tracking, Viability Evaluation, and Doubling Time Calculation

Once the prostate cancer co-culture spheroids are formed in the 384 hanging drop plates, the spheroids were cultured and monitored for 7 days in the PC-3 proliferation characterization experiments. Co-culture spheroids cultured in the 384 hanging drop array plates were imaged by phase contrast microscopy as well as fluorescence microscopy (Nikon TE-300). The number of PC-3^{DsRed} cells within each spheroid was

tracked by fluorescence everyday for a total of 7 days. On the last day (Day 7) of culture, the spheroids were stained with calcein-AM (L3224, Invitrogen) to evaluate cellular viability. 5 μl of calcein-AM working solution dissolved in PBS to a concentration of 5μg/ml was added directly into the 20 μl hanging drops (final calcein-AM concentration of 1μg/ml) and incubated for 30 minutes at 37^{o}C.

PC-3^{DsRed} doubling time calculation for the co-culture spheroids was slightly modified from the method described in Chapter 2. The modified calculation method is believed to provide a more accurate estimate of the doubling time. Briefly, PC-3^{DsRed} doubling time inside the co-culture spheroids was calculated by fitting an exponential-fit line through the PC-3^{DsRed} proliferation graph of each spheroid sample (number of PC-3^{DsRed} cells/spheroid vs. time). The equation obtained from each fit was subsequently used to solve for the time it takes for the initial number of PC-3^{DsRed} cells per spheroid at day 1 to double. The final doubling time was determined to be the time it takes for the PC-3^{DsRed} cells present at day 1 to double. The same method was used to calculate the doubling time of all PC-3^{DsRed} co-culture spheroid samples. The average and standard error were then calculated from the estimated doubling time for each co-culture spheroid sample.

5.2.7 Spheroid Retrieval for Flow Cytometry Analysis

For the cell cycling stage analysis experiments, spheroids were cultured and monitored for 14 days to allow sufficient time for the prostate cancer cells to adapt to the

3D co-culture environment. Co-culture spheroids cultured in the 384 hanging drop array plates were imaged by phase contrast microscopy as well as fluorescence microscopy (Nikon TE-300) every other day. On Day 14, spheroids were retrieved from the 384 hanging drop plates and pooled for evaluation of the prostate cancer cell cycling stage. With the simple liquid handling procedures offered by the 384 hanging drop plate, spheroids were easily harvested by direct pipetting. Upon co-culture spheroids retrieval (enough spheroids were collected to ensure that there are at least 10,000 prostate cancer cells to analyze), the spheroids were gently broken up into single cells using enzyme-free cell dissociation buffer with 1 hour incubation time and gentle pipetting. After spheroids were broken into single cells, the cell suspension was centrifuged to remove cell dissociation buffer and fixed in BD Cytofix (554655, BD Biosciences) overnight.

5.2.8 Cell Cycling Assays

Cell cycle status of the prostate cancer cells in these co-culture spheroids and conventional 2D mono-cultures were analyzed by FACS using propidium iodide (PI, Molecular Probes) and Ki-67 staining methods. Ki-67 antibody was conjugated to APC-Cy7 using Lightning-Link APC-Cy7 Tandem Conjugation Kit (Innova Biosciences) following manufacturer's protocol. Cell samples were first treated with saponin to permeabilize cell membranes without destroying them. PC-$3^{\text{Luc GFP}}$ or PC-$3^{\text{Luc E GFP}}$ cells, HUVECs, and MC3T3-E1 cells from 2D mono-cultures were pre-mixed at equal ratios to obtain samples with heterogeneous cell mixtures. Thereafter, cells were simultaneously incubated in 50 μg/ml of PI and Ki-67 conjugated antibody for 1 hour. The cell cycle

state was analyzed by flow cyometry (BD FACSAria II Flow Cytometer, Becton Dickinson). We specifically look for the prostate cancer cell population, which is the only cell type within the sample mixtures that stably expresses GFP. Since the intensity of the PI signal is directly proportional to DNA content, a histogram of the PI intensity was plotted on the linear scale to identify peaks that signify cell in the G_0/G_1 phase, S Phase, and G_2/M phase. The prostate cancer cell population was also analyzed for negative Ki-67 staining, which indicates that the cells are in the quiescent G_0 state.

5.3 Results and Discussion

5.3.1 Gene Expression Profiles in CD133$^+$ and CD133$^-$ PC-3^{DsRed} Cells

In an effort to develop a reporter system to monitor the maintenance of the CD133 progenitor marker on PC-3^{DsRed} cells in real-time, we started the initiative to look at the expression profiles of several stem cell-relevant genes in the CD133$^+$ and CD133$^-$ subpopulations of PC-3^{DsRed} cells. The rationale is that if we can identify and correlate key stem cell-related genes to the presence of CD133 in PC-3^{DsRed} cells, then a luciferase construct could be placed under the promoter control of the target gene of interest, and transfect the construct into PC-3^{DsRed} cells. Real-time monitoring of the presence of the CD133 marker in PC-3^{DsRed} cells could then be achieved by a simple luciferase assay.

PC-3^{DsRed} cells were sorted for CD133^{+} and CD133^{-} subpopulations for a total of two times (designated as batch I and batch II). Both batches were evaluated for the expression levels of 8 critical genes implicated in the self-renewal, homing, localization, and quiescence of HSCs and metastatic prostate cancer cells (Bmi-1, Ink4a, CXCR4, CXCR7, Annexin II receptor, AXL, Sky, and Mer) in two repeat trials. Figure 5.2a and b summarize the results obtained from the evaluation of these 8 gene expression levels in the two batches of sorted CD133^{+} and CD133^{-} PC-3^{DsRed} cells from two separate trials. Unfortunately, no correlation was found between the CD133 marker of prostate cancer progenitor cell and the 8 genes investigated. The results obtained were not consistent between the two different batches of sorted CD133^{+} and CD133^{-} cells, and between the two independent trials. Since the data obtained was not conclusive we were not able to proceed to the construction and transfection of the proposed luciferase construct.

5.3.2 CD44^{+}, CD44^{-}, Anxa2R^{+}, and Anxa2R^{-} Subpopulations

Because the gene expression profile data we obtained from the PC-3^{DsRed} cells sorted for CD133^{+} and CD133^{-} was inconclusive, we hypothesized that merely sorting for the CD133 marker did not produce a pure population for prostate cancer progenitor cells. Therefore, we proceeded to sort the CD133^{+} and CD133^{-} populations of PC-3^{DsRed} cells further into CD44^{+} and CD44^{-}, or Anxa2R^{+} and Anxa2R^{-} subpopulations (Figure 5.3a). Figure 5.3b and Table 5.1 show the sorting statistics of the CD44^{+} and Anxa2R^{+} subpopulations from two independent sorting trials from two batches of cells. In both batches, the CD133^{+} PC-3^{DsRed} population seems to be enriched in both CD44^{+} and

Anxa2R^{+} cells. In the first batch, only about 5% of the CD133^{-} PC-3^{DsRed} cells are CD44^{+}, but 90% of the CD133^{+} PC-3^{DsRed} cells are CD44^{+}. Similarly in the second batch, only less than 1% of CD133^{-} PC-3^{DsRed} cells are CD44^{+}, but 66% of the CD133^{+} PC-3^{DsRed} cells are CD44^{+}. For Anxa2R sorting, we see a larger difference in the subpopulation percentages between the two batches of cells. Nevertheless, the overall trend is still the same. Only about 0.4% of the CD133^{-} PC-3^{DsRed} cells are Anxa2R^{+}, but 3% of the CD133^{+} PC-3^{DsRed} cells are Anxa2R^{+} in the first trial. In the second batch, we see a huge increase in the percentage of Anxa2R^{+} cells with 9% of the CD133^{-} PC-3^{DsRed} cells being Anxa2R^{+} and 70% of the CD133^{+} PC-3^{DsRed} cells being Anxa2R^{+}.

Next, we looked at the expression levels of three select stem cell genes that seemed more relevant and consistent in previous results—Bmi-1, Ink4a, and Anxa2R in all the eight sorted subpopulations. Figure 5.4a shows the overall results and Figure 5.4b highlights the comparison only between the double negative (–/–) and double positive (+/+) cell populations. Again, we found inconsistency in the gene expression level profiles between these two different sorted batches of cells. Since no strong correlation was found between the genes relevant in stem cells and the prostate cancer stem cell-enriched populations, we were not able to proceed in developing a reporter system to monitor the CD133 marker in PC-3^{DsRed} cells. As a result, we have not successfully found a method to validate the maintenance of stem- or progenitor-like conditions in the quiescent CD133^{+} PC-3^{DsRed} co-culture spheroids reported in Chapter 2.

5.3.3 PC-3^{DsRed} Growth and Viability in Co-culture Spheroids Cultured in the 384 Hanging Drop Array Plate

To lay the foundation for future anti-cancer drug screening experiments, the culture of PC-3^{DsRed}, HUVEC, and MC3T3-E1 in co-culture spheroids as an *in vitro* model for metastatic prostate cancer niche was scaled up to a high-throughput format in the second generation 384 hanging drop array plates described in Chapter 4. Due to the change in culture platform and the increase in co-culture spheroid size, PC-3^{DsRed} cell proliferation within the 3D co-culture constructs was characterized again. PC-3^{DsRed} cells were tracked for their proliferation within each spheroid by their red fluorescence everyday for 7 days. Figure 5.5a to c show the overall growth pattern and viability of the PC-3^{DsRed} cells within the 3D co-culture spheroids over the course of 1 week. Figure 5.5a shows the optical and fluorescent time-lapse images of a representative PC-3^{DsRed}, HUVEC, and MC3T3-E1 co-culture spheroid. It is clear from both the phase and fluorescent images that PC-3^{DsRed} cells were still able to actively proliferate inside the co-culture spheroids. Moreover, PC-3^{DsRed} cells were still alive after 7 days of culture inside the co-culture spheroid as shown in Figure 5.5b with a live viability staining image obtained using fluorescent microscopy. Green cells stained with calcein-AM indicate live cells whereas red cells were PC-3^{DsRed} cells that expressed red fluorescence. Since almost all the red cells overlap with the viable green color, most PC-3^{DsRed} cells were able to survive under the hanging drop 3D co-culture environment after 7 days in culture. Figure 5.5c summarizes the overall proliferation trend of PC-3^{DsRed} cells cultured in the co-culture spheroids as hanging drops. As found in the results from Chapter 2, PC-3^{DsRed} cells proliferated at a relatively slow rate in 3D co-culture spheroids compared to conventional 2D monolayer mono-cultures. However, as we calculated the doubling time

of the PC-3^{DsRed} cells under the 3D co-culture hanging drop environment, we found an obvious decrease in the doubling time estimation from the result presented in Chapter 2. The PC-3^{DsRed} doubling time in the hanging drop platform was estimated to be 87 hours (80 hours if calculated using the original doubling time estimation method described in Chapter 2) while it was estimated to be around 200 hours (Table 2.1) in the original study. Although the growth rate of PC-3^{DsRed} cells inside 3D co-culture spheroids in the hanging drop platform is found to be about 2.5 times faster than in the microfluidic device, such proliferation rate of PC-3^{DsRed} cells in 3D co-culture environment is still much slower than the 24 hour doubling time of PC-3^{DsRed} cells in conventional 2D mono-culture (Table 2.1).

It is postulated that perhaps the higher initial seeding number (1200-cell spheroids in hanging drop plate versus the 300- to 400-cell spheroids in microfluidic device) has an effect on the overall growth rate of the PC-3^{DsRed} cells in the 3D co-culture spheroids. Higher number of PC-3^{DsRed} cells aggregated closely inside a larger compacted 3D co-culture spheroid construct, where diffusion and transport are less efficient than smaller spheroid, consequently leads to secretion of more autocrine factors localized within the spheroid and therefore seen at higher concentrations by the individual PC-3^{DsRed} cells. If the growth rate of the PC-3^{DsRed} cells in the larger spheroids was already faster than in the smaller spheroids, then the condition could even be exacerbated as PC-3^{DsRed} cells start to proliferate and out number the support cells. Although the co-culture ratio between these independent experiments was kept constant, but because the HUVEC and MC3T3-E1 support cells mainly remain quiescent, it is also plausible that secreted factors from the

neighboring support cells to keep PC-3^{DsRed} cells quiescent would be diluted out to lower concentrations not enough to induce dormancy of the PC-3^{DsRed} cells.

5.3.4 Cell Cycling Stage of PC-3$^{Luc\ GFP}$ and PC-3$^{Luc\ E\ GFP}$ Cells in Co-culture Spheroids

To explore whether the 3D co-culture spheroid constructs induce prostate cancer cells into dormant states, cell cycling states were evaluated by flow cytometry. We specifically looked for and compared the cell cycling states from two types of PC-3 populations—mesenchymal PC-3$^{Luc\ GFP}$ cells that have been characterized to have already undergone EMT and epithelial PC-3$^{Luc\ E\ GFP}$ cells that have not undergone EMT. 3000-cell PC-3, HUVEC, MC3T3T-E1 co-culture spheroids were formed and cultured from both types of PC-3 cells, and the PC-3 population was analyzed for their cell cycling states on Day 14. The phase and fluorescent time-lapse images for both PC-3 cell types cultured in the co-culture spheroids were shown in Figure 5.6a and b. From both the phase and fluorescent images, it is very obvious that both PC-3 cell types proliferated over the 14 days of culture. No obvious difference was observed between these two types of PC-3 cells.

Figure 5.7 and Figure 5.8 show the results obtained from PI and Ki-67 staining of PC-3$^{Luc\ GFP}$ cells, respectively. And Figure 5.9 and Figure 5.10 show the results obtained from PI and Ki-67 staining of PC-3$^{Luc\ E\ GFP}$ cells, respectively. The results obtained from the 3D co-culture spheroid samples were also compared to the cell cycling states of the same types of PC-3 cells cultured in conventional 2D monolayer mono-cultures. Again,

no obvious difference was found in the cell cycling states of the mesenchymal PC-3$^{Luc\ GFP}$ cells and the epithelial PC-3$^{Luc\ E\ GFP}$ cells. From the PI staining results, no obvious G_0/G_1 peak was identified for both mesenchymal and epithelial PC-3 cell types in both 2D mono-culture and 3D co-culture samples. Most of the cells were found in the S and G_2/M phases of the cell cycle (Figure5.7, Figure 5.9, and Table5.2). This signifies that the majority of both types of PC-3 cells cultured in either 2D mono-cultures or 3D co-cultures are in their actively proliferating states. These results are further confirmed by KI-67 staining results presented in Figure 5.8 and Figure 5.10. Almost all cells from both PC-3 cells types cultured in either 2D mono-cultures or 3D co-culture spheroids are Ki-67$^+$. This indicates that almost all cells are in the G_1 and S/M/G_2 states. 3D co-culture condition did not increase the fraction of PC-3 cells in the quiescent G_0 state. Thus, dormancy of prostate cancer cells was not induced in the 3D co-culture spheroids. These results are also in accordance with our visual observation as shown in Figure 5.6.

Although quiescence was not found to be induced in the PC-3 cells cultured in the 3D co-culture spheroids, it should be noted that these are the bulk population of PC-3 cells. Further experiments are required to characterize the proliferation and cell cycling state of the CD133$^+$ subpopulation of PC-3 cells that were found to be quiescent within the co-culture spheroids in Chapter 2. It is very likely that it is only the CD133$^+$ population and not the bulk prostate cancer population that is more quiescent in the bone marrow niche. Proving such concept would support the CSC hypothesis that only CSCs are able to establish metastasis, remain dormant, escape from anti-cancer treatments such as chemotherapy, and regenerate tumors.

5.4 Conclusion

We describe efforts to study the underlying mechanisms in regulating prostate cancer stem cells and tumor dormancy in more detail. Specifically, we first explored the relationship between several stem cell-relevant genes and the $CD133^+$ prostate cancer cell population believed to be enriched in CSCs in an effort to develop a reporter system to track the maintenance of the CD133 marker in prostate cancer cells. Although the results were inconsistent, we were prompted to study prostate CSCs utilizing alternative approaches from the tumor dormancy perspective. We subsequently scaled up the PC-3 co-culture spheroids culture as *in vitro* 3D models of prostate cancer bone metastasis in a high-throughput format using the 384 hanging drop plates in preparation for future drug screening initiatives. While utilizing the hanging drop platform, we showed that PC-3 cells still actively proliferate in the co-culture spheroids, and thus dormancy of the bulk prostate cancer cell population was not induced by 3D co-culture. We also obtained valuable insights that the co-culture ratios and the absolute initial cell seeding numbers may have an effect in prostate cancer cell growth behavior. This is in accordance with the clinical observation that very few numbers of disseminated tumor cells metastasized to distant sites such as the bone marrow niche could remain dormant for a long time in some patients while relapse is found in other patients much sooner.

A lot of the findings and concepts presented in this chapter are still current work in progress. Much effort is still needed to investigate the prostate CSC-enriched $CD133^+$ population in more detail. Specifically, the proliferation pattern, quiescence, and maintenance of stem or progenitor cell properties of the $CD133^+$ prostate cancer cells should be well-characterized in the 3D co-culture spheroids. The proliferation characterization and quiescence validation can be analyzed by the same techniques presented in this chapter. The presence of the CD133 marker could also be confirmed by flow cytometry. Most importantly, efforts should be devoted to explore the molecular mechanisms in inducing the $CD133^+$ prostate cancer cells in the co-culture spheroids into dormant state as seen in Chapter 2. We have already initiated studies to elucidate such underlying mechanisms by evaluating the quiescence of prostate cancer cells co-cultured with support cells (specifically the MC3T3-E1 mouse pre-osteoblasts) that have knockdowns of various key molecules implicated in tumor dormancy—GAS6, Annexin II, SDF-1, TGFβ, and BMP7. Another important question to address is whether the dormant state of $CD133^+$ prostate cancer cells is able to maintain their CD133 marker and thus keep their as stem- or progenitor-like properties. As these significant biological questions are unraveled, it would be easy to successfully engineer an accurate *in vitro* 3D metastatic prostate cancer bone marrow niche to culture and maintain CSCs in their stem-like and dormant states using our high-throughput hanging drop platform. An *in vitro* niche containing a pure and quiescent prostate CSC population will serve as an accurate and excellent model to screen and test for drugs that specifically target the dormant metastasized prostate cancer cells. Such an *in vitro* bone metastasized prostate cancer model reflective of the actual dormant tumor in the metastatic niche *in vivo* is an integral

part in the success of novel anti-cancer therapeutic development. Findings in the molecular mechanisms involved in inducing tumor dormancy will provide significant insights into the design and targets of novel anti-cancer therapeutics.

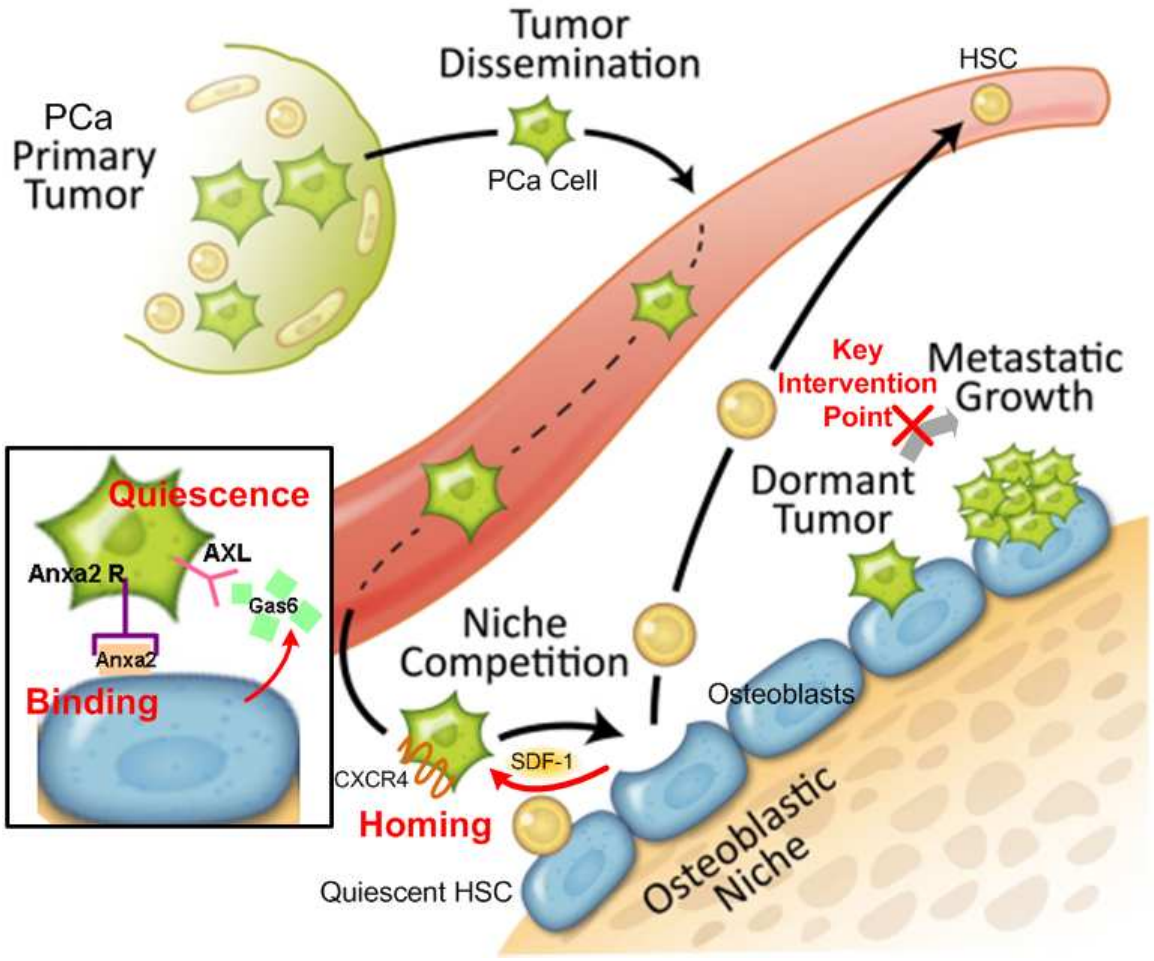

Figure 5.1. Schematic cartoon illustrating the nest parasitism hypothesis of prostate cancer metastasis to the bone, highlighting the homing, binding, and quiescence mechanisms leading to tumor dormancy in the bone marrow.

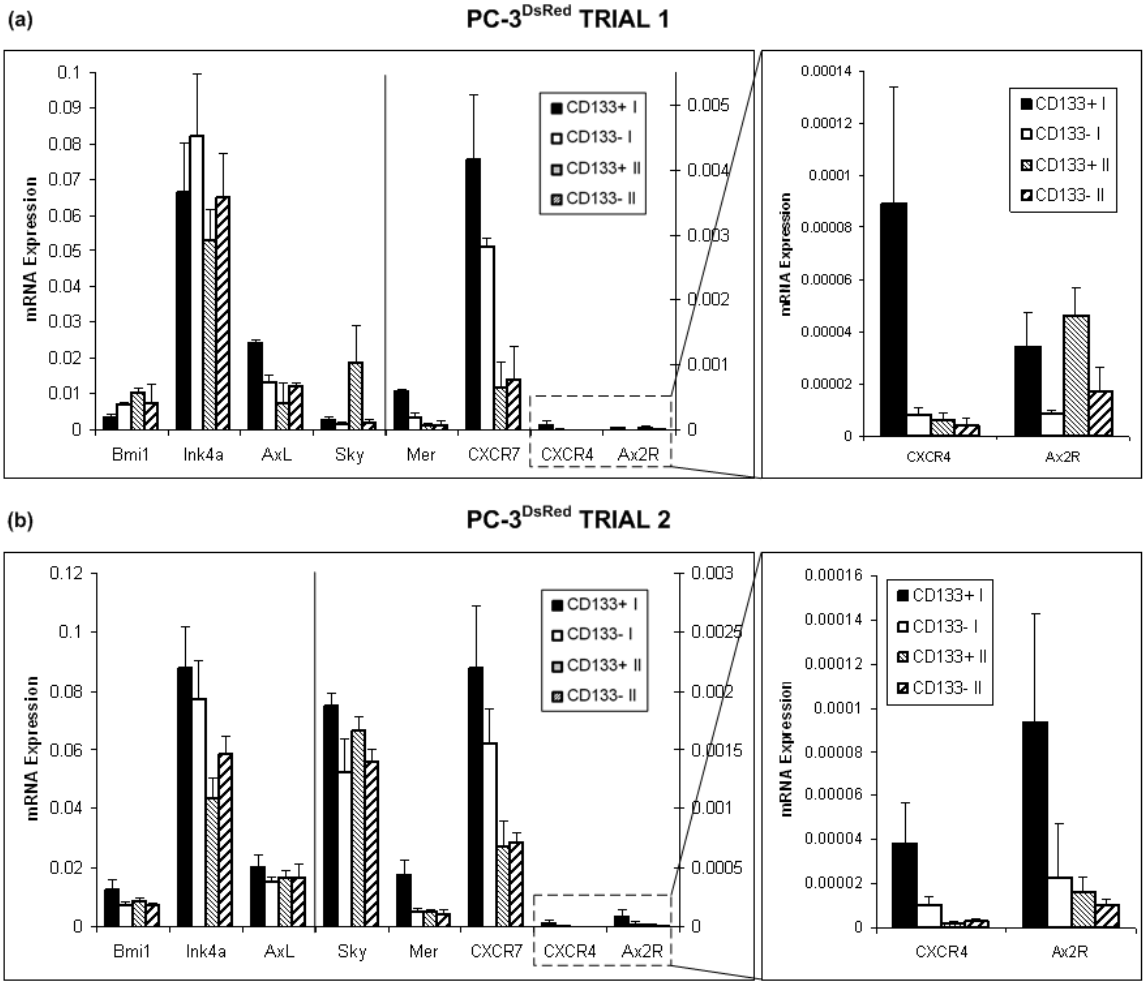

Figure 5.2. Bmi-1, Ink4a, AXL, Sky, Mer, CXCR7, CXCR4, and Anxa2R mRNA expression levels of $CD133^{+}$ and $CD133^{-}$ subpopulations of the $PC\text{-}3^{DsRed}$ cell line as determined by real time RT-PCR. Data obtained from sorted Batch I of cells are designated with "I," and similarly Batch II cells are designated with "II." Results from trial 1 are shown in **(a)**, and results from trial 2 are shown in **(b)**. Data were normalized to β-actin and are presented as mean ± SD from triplicates.

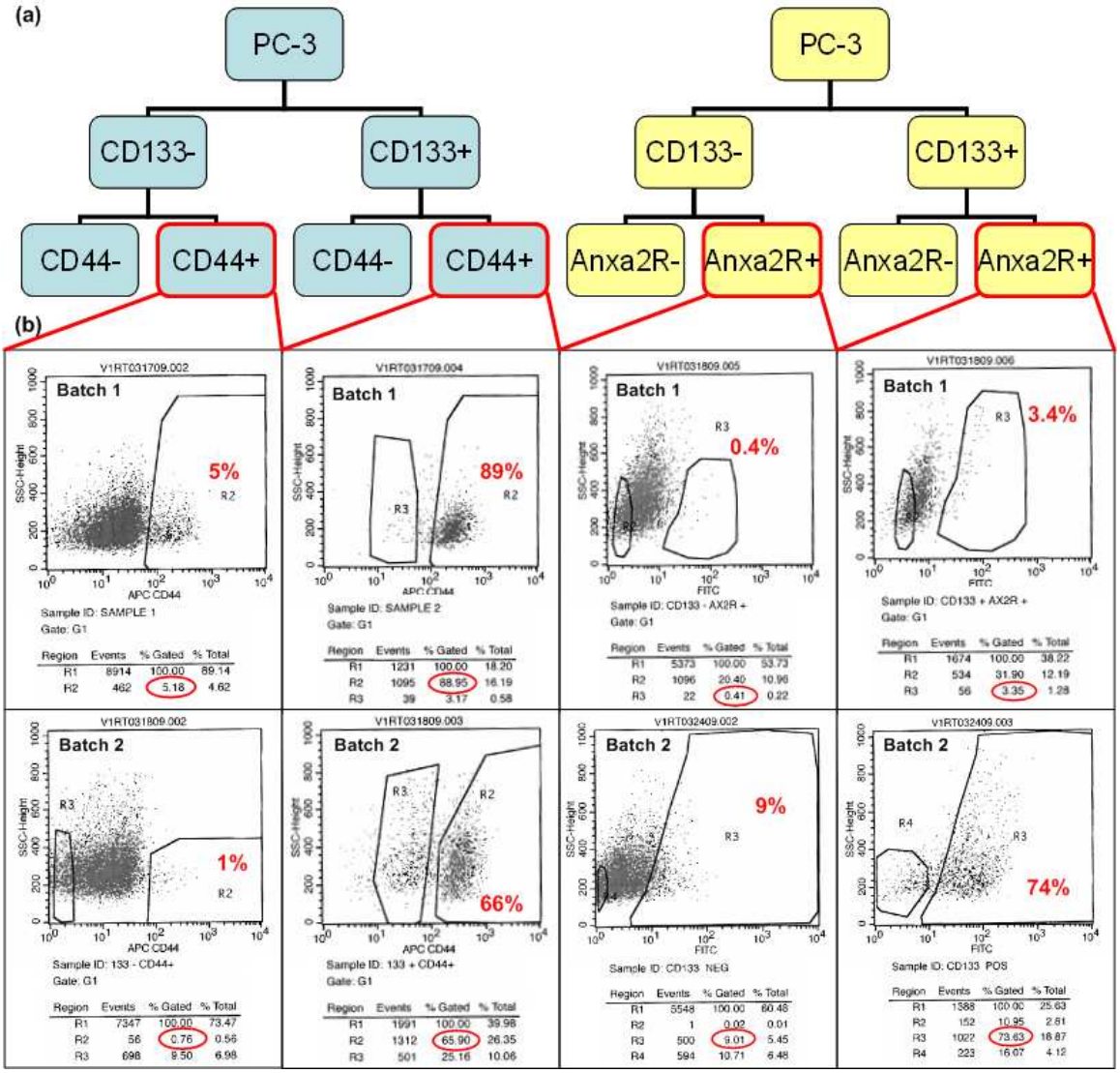

Figure 5.3. **(a)** Organizational charts outlining the sequential sorting process of PC-3^{DsRed} cells into various subpopulations. **(b)** Flow cytometric analysis of the percentages of CD44^{+} (left 2 columns) or Anxa2R^{+} (right 2 columns) subpopulations within the CD133^{-} and CD133^{+} PC-3^{DsRed} cells. The first row of flow cytometric data represent data from the first sorting batch of cells, and the second row of data represent data from the second sorting batch of cells.

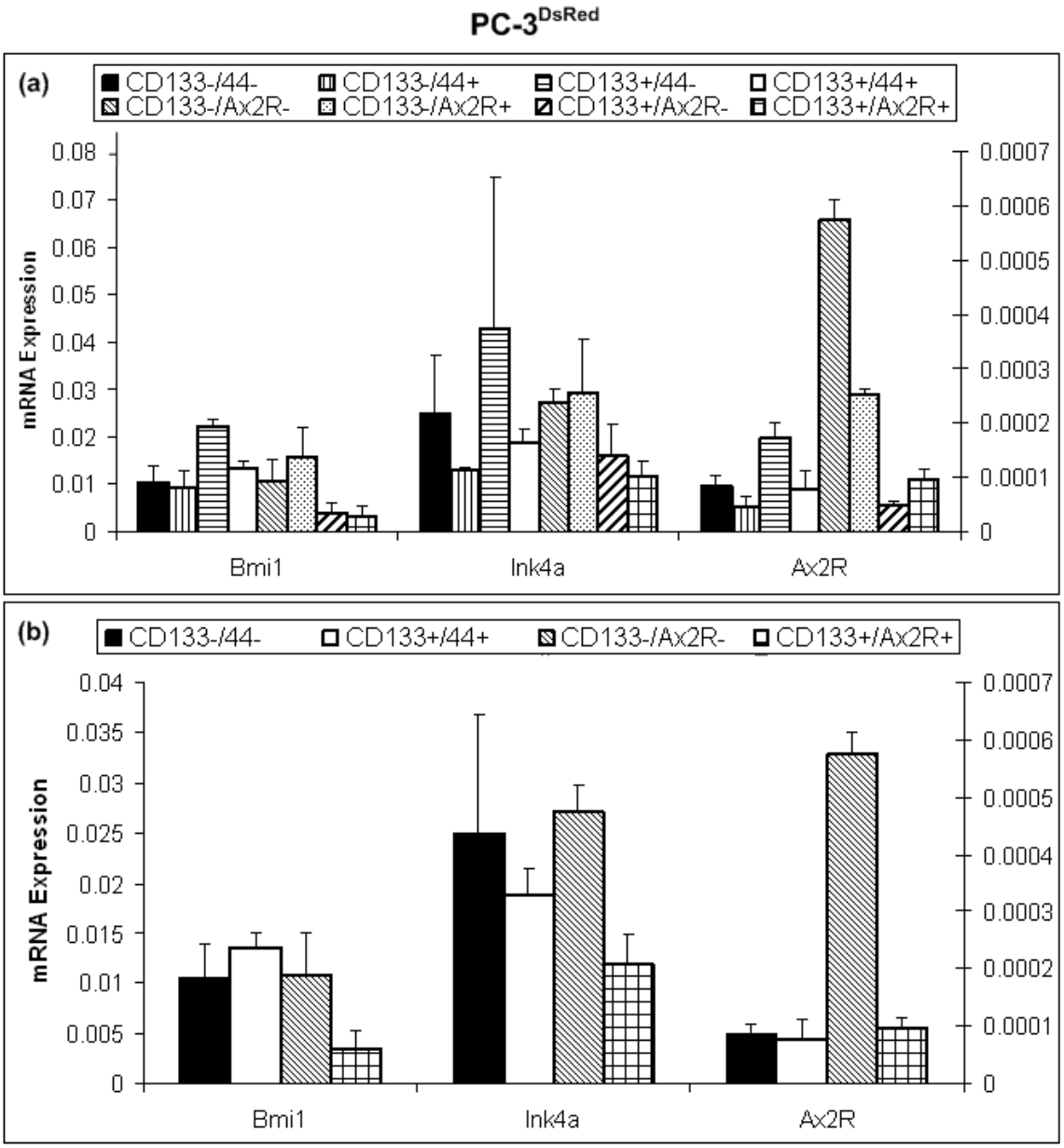

Figure 5.4. **(a)** Bmi-1, Ink4a, and Anxa2R mRNA expression levels of the various 8 different subpopulations (See Figure 5.3a) of the PC-3^{DsRed} cell line as determined by real time RT-PCR. **(b)** Bmi-1, Ink4a, and Anxa2R mRNA expression levels data from (a), but only showing results from the 4 double negative and double positive PC-3^{DsRed} subpopulations (See Figure 5.3a)—CD133^{-}/CD44^{-}, CD133^{+}/CD44^{+}, CD133^{-}/Anxa2R^{-}, and CD133^{+}/Anxa2R^{+}. Data were normalized to β-actin and are presented as mean ± SD from triplicates.

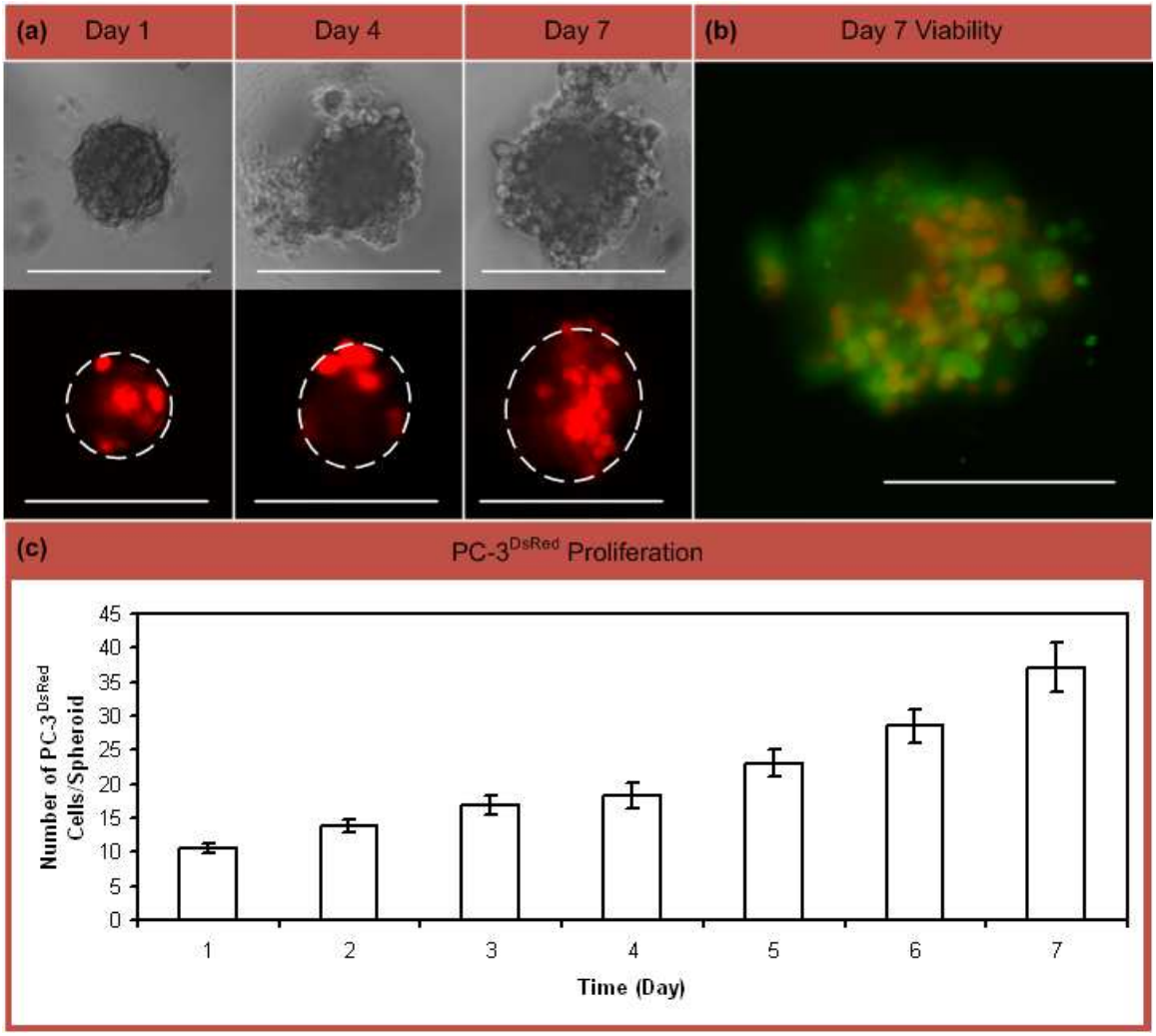

Figure 5.5. **(a)** Phase and fluorescent time-lapse images of a representative 1200-cell PC-3^{DsRed}, HUVEC, and MC3T3-E1 1:50:50 co-culture spheroid showing PC-3^{DsRed} proliferation over 7 days in the hanging drop culture. **(b)** A fluorescent image of live calcein-AM staining overlapped with the red fluorescence from PC-3^{DsRed} cells within the co-culture spheroid illustrating the viability of PC-3^{DsRed} cells. Red = PC-3^{DsRed} cells, Green = Live cells (calcein-AM stain), Yellow = Live PC-3^{DsRed} cells. **(c)** Graph of PC-3^{DsRed} proliferation pattern inside co-culture spheroids over a course of 1 week. Y-axis shows the average number of PC-3^{DsRed} cells per spheroid, and x-axis is the time in days. Data is presented as mean ± standard error. Scale bar is 200 μm.

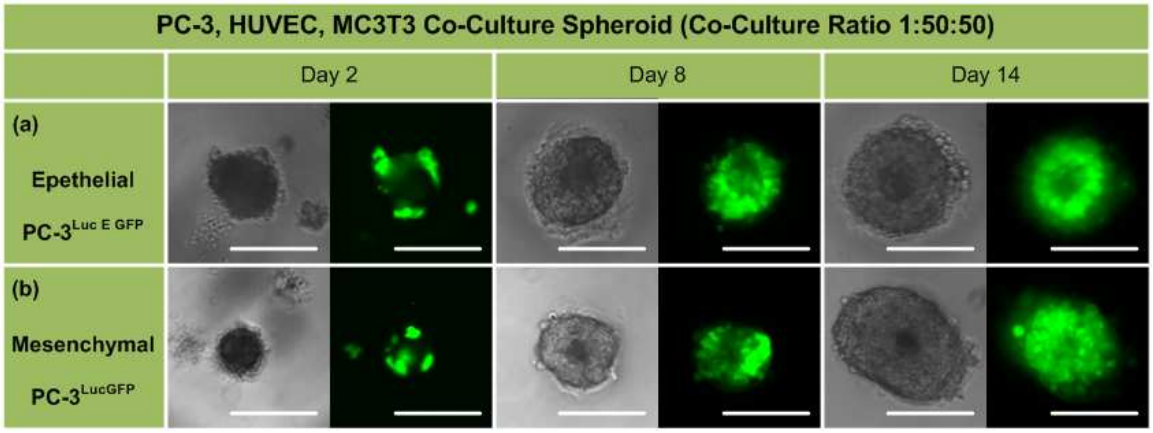

Figure 5.6. Phase and fluorescent time-lapse images of a representative 3000-cell **(a)** epithelial PC-3$^{Luc\ E\ GFP}$ and **(b)** mesenchymal PC-3$^{Luc\ GFP}$ spheroid co-cultured with HUVEC and MC3T3-E1 cells at 1:50:50 ratio, showing PC-3^{DsRed} proliferation over 14 days in the hanging drop culture.

Figure 5.7. Flow cytometric analyses of PI staining in mesenchymal PC-3$^{Luc\ GFP}$ cells from 2D mono-culture and 3D co-culture spheroid samples showing the percentages of cells in each of the G_0/G_1, S, and G_2/M cell cycling states. Each histogram represents data from **(a)** 2D mono-culture unstained control, **(b)** 2D mono-culture stained sample, **(c)** 3D co-culture spheroid unstained control, **(d)** 3D co-culture spheroid stained sample 1, and **(e)** 3D co-culture spheroid stained sample 2.

(a) 2D Mono-culture Unstained Control

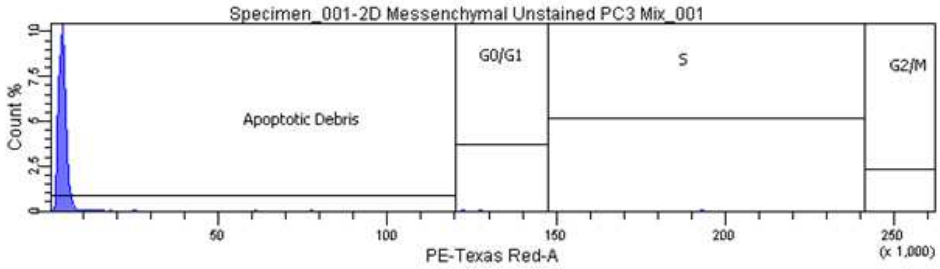

(b) 2D Mono-culture Stained Sample

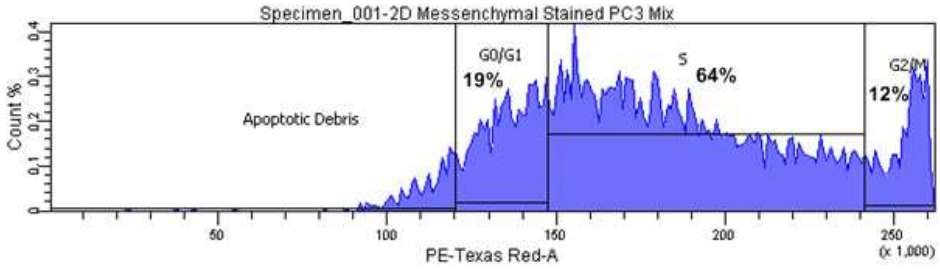

(c) 3D Co-culture Unstained Control

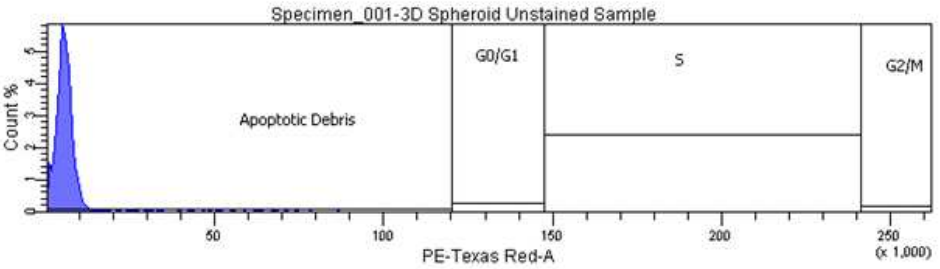

(d) 3D Co-culture Stained Sample 1

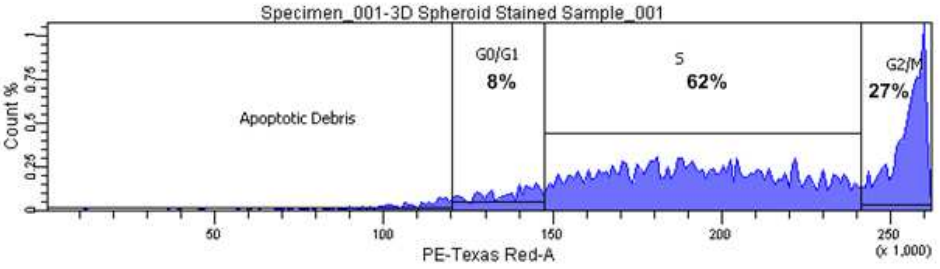

(e) 3D Co-culture Stained Sample 2

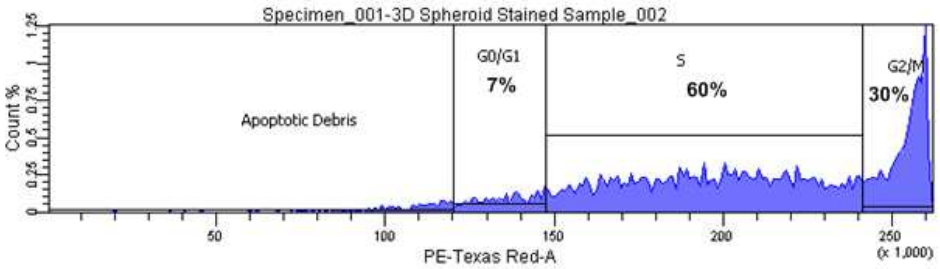

Figure 5.7

Figure 5.8. Flow cytometric analyses of Ki-67 staining in mesenchymal PC-3$^{Luc\ GFP}$ cells from 2D mono-culture and 3D co-culture spheroid samples showing the percentages of cells that are Ki-67^{+} (G_1, S, G_2, and M states of cell cycle). Each histogram represents data from **(a)** 2D mono-culture unstained control, **(b)** 2D mono-culture stained sample, **(c)** 3D co-culture spheroid unstained control, **(d)** 3D co-culture spheroid stained sample 1, and **(e)** 3D co-culture spheroid stained sample 2.

(a) 2D Mono-culture Unstained Control

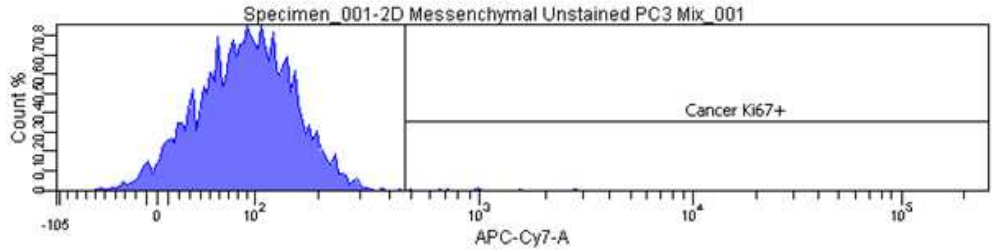

(b) 2D Mono-culture Stained Sample

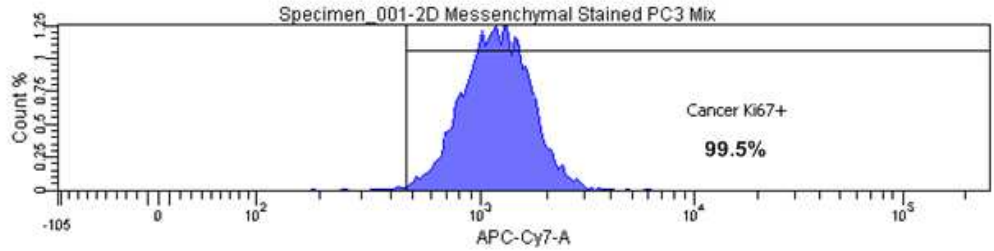

(c) 3D Co-culture Unstained Control

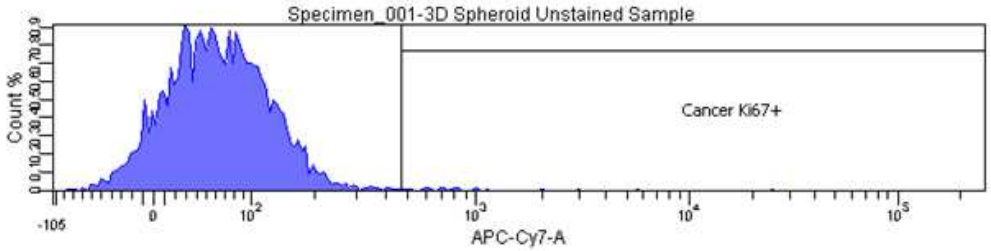

(d) 3D Co-culture Stained Sample 1

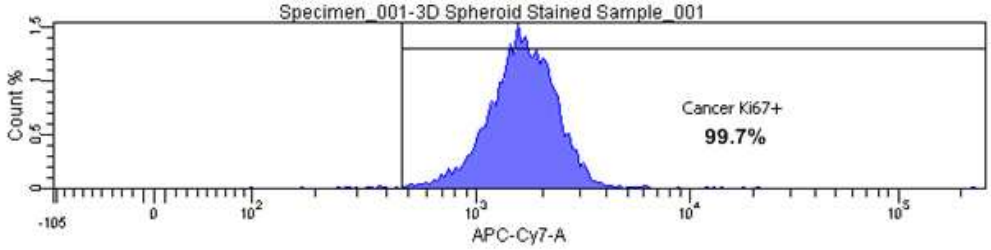

(e) 3D Co-culture Stained Sample 2

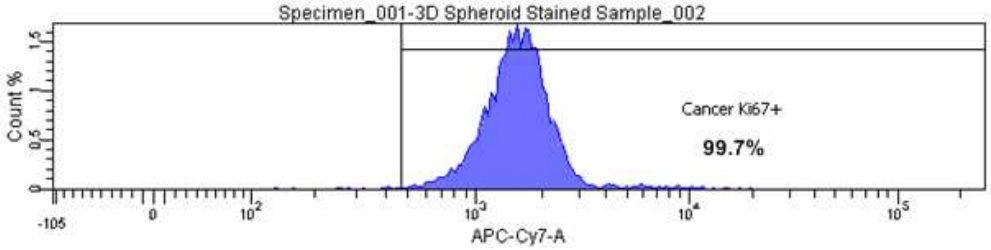

Figure 5.8

Figure 5.9. Flow cytometric analyses of PI staining in epithelial PC-3$^{\text{Luc E GFP}}$ cells from 2D mono-culture and 3D co-culture spheroid samples showing the percentages of cells in each of the G_0/G_1, S, and G_2/M cell cycling states. Each histogram represents data from **(a)** 2D mono-culture unstained control, **(b)** 2D mono-culture stained sample, **(c)** 3D co-culture spheroid unstained control, **(d)** 3D co-culture spheroid stained sample 1, and **(e)** 3D co-culture spheroid stained sample 2.

(a) 2D Mono-culture Unstained Control

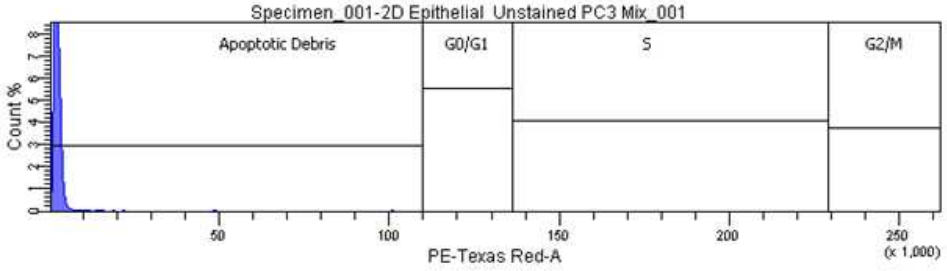

(b) 2D Mono-culture Stained Sample

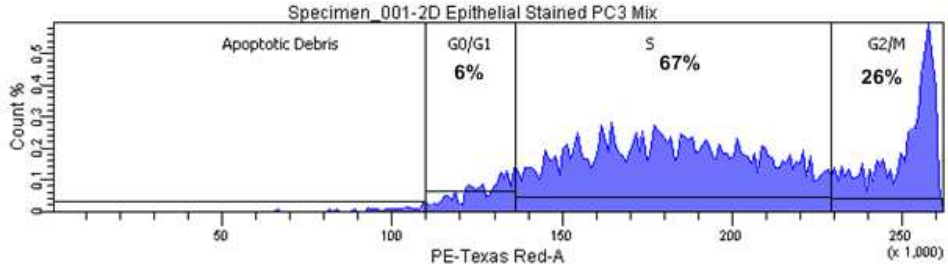

(c) 3D Co-culture Unstained Control

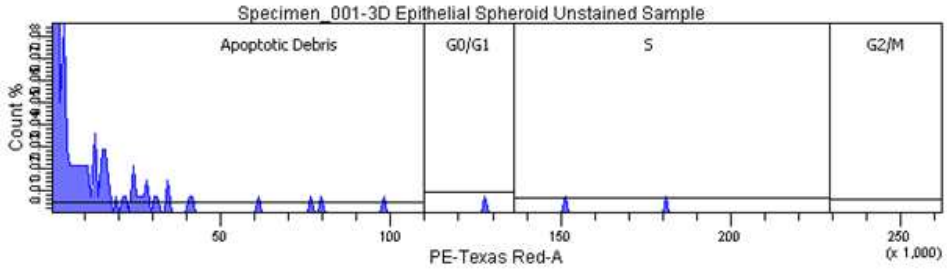

(d) 3D Co-culture Stained Sample 1

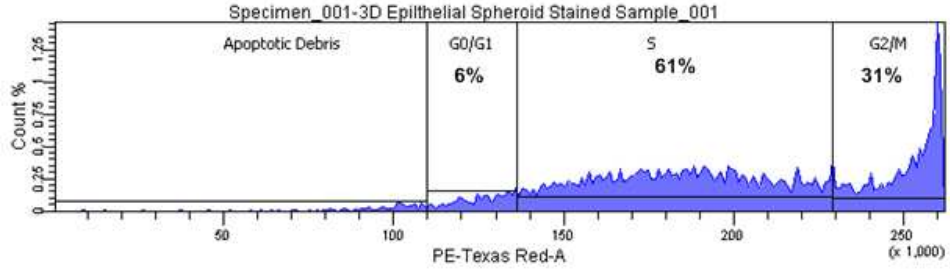

(e) 3D Co-culture Stained Sample 2

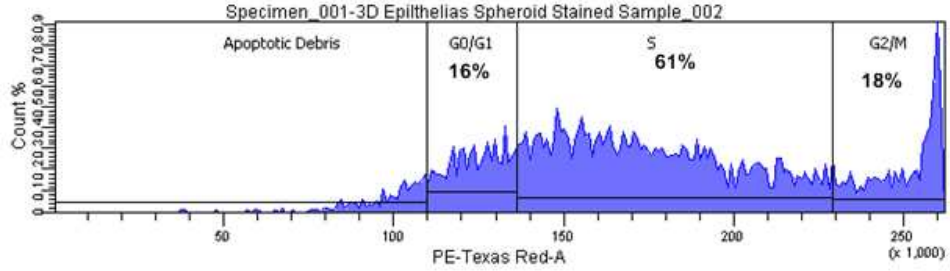

Figure 5.9

Figure 5.10. Flow cytometric analyses of Ki-67 staining in epithelial PC-3$^{Luc\ E\ GFP}$ cells from 2D mono-culture and 3D co-culture spheroid samples showing the percentages of cells that are Ki-67^{+} (G_1, S, G_2, and M states of cell cycle). Each histogram represents data from **(a)** 2D mono-culture unstained control, **(b)** 2D mono-culture stained sample, **(c)** 3D co-culture spheroid unstained control, **(d)** 3D co-culture spheroid stained sample 1, and **(e)** 3D co-culture spheroid stained sample 2.

(a) 2D Mono-culture Unstained Control

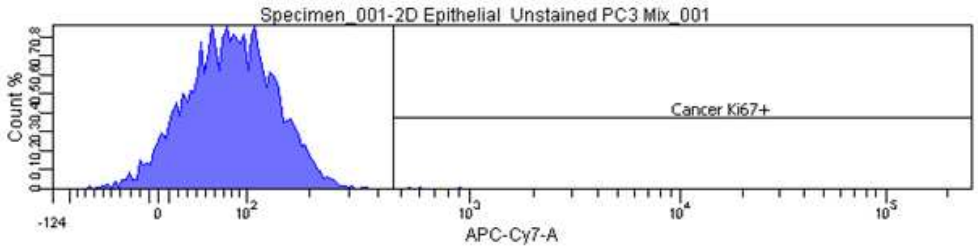

(b) 2D Mono-culture Stained Sample

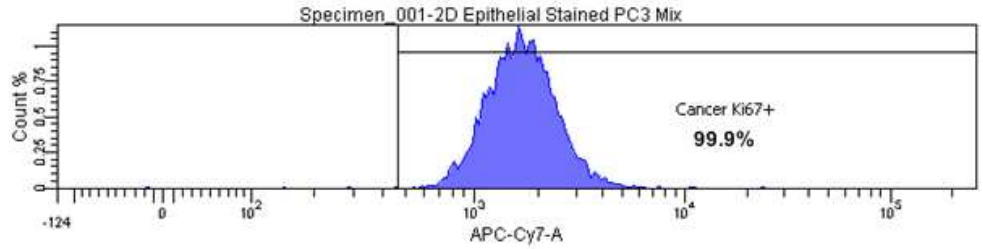

(c) 3D Co-culture Unstained Control

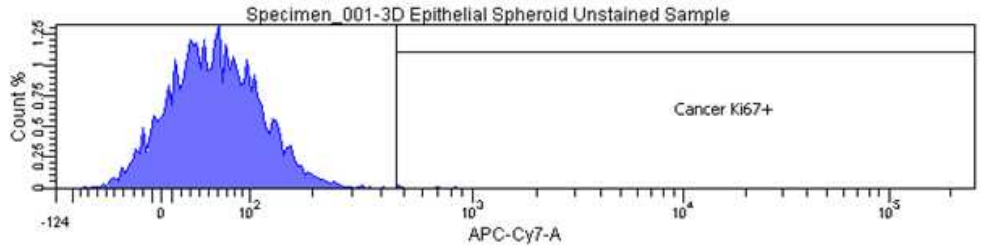

(d) 3D Co-culture Stained Sample 1

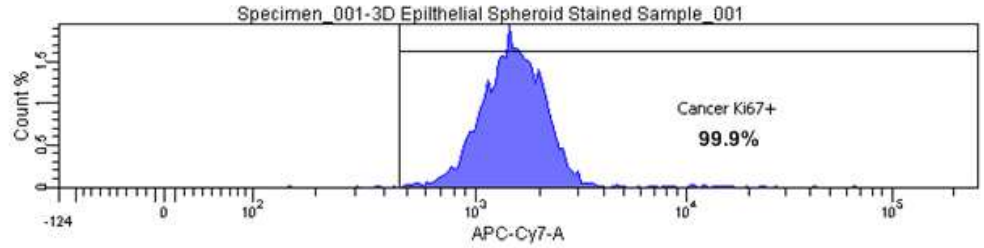

(e) 3D Co-culture Stained Sample 2

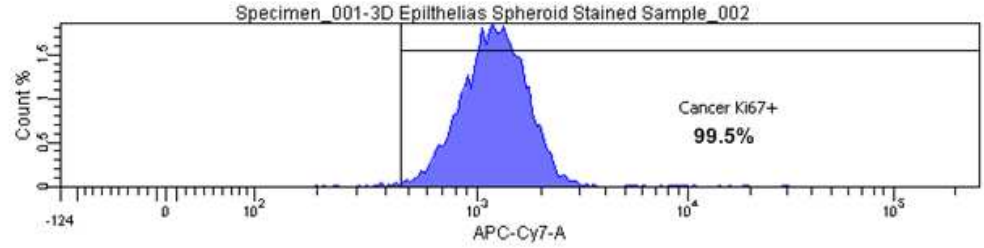

Figure 5.10

PC-3^{DsRed} Sorting Statistics			
	Trial	**CD133$^-$**	**CD133$^+$**
% of CD44$^+$ Cells	**1**	5.2%	89.0%
	2	0.8%	65.9%
% of Anxa2R$^+$ Cells	**1**	0.4%	3.4%
	2	9.0%	73.6%

Table 5.1. Summary of CD44$^+$ and Anxa2R$^+$ subpopulations found in CD133$^-$ and CD133$^+$ PC-3^{DsRed} cells

Cell Cycling State of PC-3 Cells						
Cell Cycle	% Cell					
	Mesenchymal PC-3$^{Luc\ GFP}$			Epithelial PC-3$^{Luc\ E\ GFP}$		
	2D Mono-culture	3D Co-culture Sample 1	3D Co-culture Sample 2	2D Mono-culture	3D Co-culture Sample 1	3D Co-culture Sample 2
G_0 (Ki-67$^-$)	0.5%	0.3%	0.3%	0.1%	0.1%	0.5%
G_0/G_1	18.9%	7.9%	7.0%	6.4%	5.9%	15.7%
S	64.4%	62.2%	59.9%	66.9%	61.0%	61.0%
G_2/M	12.1%	26.6%	29.5%	26.2%	31.1%	18.1%

Table 5.2. Summary of the cell cycling state of mesenchymal and epithelial PC-3 cells from 2D mono-cultures and 3D spheroid co-cultures

5.5 References

1. Al-Hajj M, Wicha MS, Benito-Hernandez A, Morrison SJ, Clarke MF. Prospective identification of tumorigenic breast cancer cells. Proc Natl Acad Sci U S A 2003;100(7):3983-8.

2. Ailles LE, Weissman IL. Cancer stem cells in solid tumors. Curr Opin Biotechnol 2007;18(5):460-6.

3. Calabrese C, Poppleton H, Kocak M, Hogg TL, Fuller C, Hamner B, et al. A perivascular niche for brain tumor stem cells. Cancer Cell 2007;11(1):69-82.

4. Cho RW, Clarke MF. Recent advances in cancer stem cells. Curr Opin Genet Dev 2008;18(1):48-53.

5. Collins AT, Paul AB, Hyde C, Stower MJ, Maitland NJ. Prospective identification of tumorigenic prostate cancer stem cells. Cancer Res 2005;65(23):10946-51.

6. Dontu G, Liu S, Wicha MS. Stem cells in mammary development and carcinogenesis: implications for prevention and treatment. Stem Cell Rev 2005;1(3):207-13.

7. Hirschhaeuser F, Menne H, Dittfeld C, West J, Mueller-Klieser W, Kunz-Schughart LA. Multicellular tumor spheroids: an underestimated tool is catching up again. J Biotechnol 2010;148(1):3-15.

8. Iwama A, Oguro H, Negishi M, Kato Y, Morita Y, Tsukui H, et al. Enhanced self-renewal of hematopoietic stem cells mediated by the polycomb gene product Bmi-1. Immunity 2004;21(6):843-51.

9. Lee J, Kotliarova S, Kotliarov Y, Li A, Su Q, Donin NM, et al. Tumor stem cells derived from glioblastomas cultured in bFGF and EGF more closely mirror the phenotype and genotype of primary tumors than do serum-cultured cell lines. Cancer Cell 2006;9(5):391-403.

10. Lessard J, Sauvageau G. Bmi-1 determines the proliferative capacity of normal and leukaemic stem cells. Nature 2003;423(6937):255-60.

11. Lu G, Maeda H, Reddy SV, Kurihara N, Leach R, Anderson JL, et al. Cloning and characterization of the annexin II receptor on human marrow stromal cells. J Biol Chem 2006;281(41):30542-50.

12. Park IK, Morrison SJ, Clarke MF. Bmi1, stem cells, and senescence regulation. J Clin Invest 2004;113(2):175-9.

13. Reya T, Morrison SJ, Clarke MF, Weissman IL. Stem cells, cancer, and cancer stem cells. Nature 2001;414(6859):105-11.

14. Ricci-Vitiani L, Lombardi DG, Pilozzi E, Biffoni M, Todaro M, Peschle C, et al. Identification and expansion of human colon-cancer-initiating cells. Nature 2007;445(7123):111-5

15. Shiozawa Y, Havens AM, Jung Y, Ziegler AM, Pedersen EA, Wang J, et al. Annexin II/Annexin II receptor axis regulates adhesion, migration, homing, and growth of prostate cancer. J Cell Biochem 2008;105(2):370-80.

16. Shiozawa Y, Havens AM, Pienta KJ, Taichman RS. The bone marrow niche: habitat to hematopoietic and mesenchymal stem cells, and unwitting host to molecular parasites. Leukemia 2008;22(5):941-50.

17. Shiozawa Y, Pedersen EA, Havens AM, Jung Y, Mishra A, Joseph J, et al. Human prostate cancer metastases target the hematopoietic stem cell niche to establish footholds in mouse bone marrow. J Clin Invest 2011. DOI:10.1172/JCI43414.

18. Shiozawa Y, Pedersen EA, Patel LR, Ziegler AM, Havens AM, Jung Y, et al. GAS6/AXL axis regulates prostate cancer invasion, proliferation, and survival in the bone marrow niche. Neoplasia 2010;12(2):116-27.

19. Sun YX, Schneider A, Jung Y, Wang J, Dai J, Wang J, et al. Skeletal localization and neutralization of the SDF-1(CXCL12)/CXCR4 axis blocks prostate cancer metastasis and growth in osseous sites in vivo. J Bone Miner Res 2005;20(2):318-29.

20. Sun YX, Wang J, Shelburne CE, Lopatin DE, Chinnaiyan AM, Rubin MA, et al. Expression of CXCR4 and CXCL12 (SDF-1) in human prostate cancers (PCa) in vivo. J Cell Biochem 2003;89(3):462-73.

21. Taichman RS, Loberg RD, Mehra R, Pienta KJ. The evolving biology and treatment of prostate cancer. J Clin Invest 2007;117(9):2351-61.

22. Wang J, Shiozawa Y, Wang J, Wang Y, Jung Y, Pienta KJ, et al. The role of CXCR7/RDC1 as a chemokine receptor for CXCL12/SDF-1 in prostate cancer. J Biol Chem 2008;283(7):4283-94.

CHAPTER 6

Conclusion and Future Direction

Cancer is a devastating disease that has greatly influenced the lives of many. Despite vast amount of research and efforts dedicated to cancer biology in the past several decades, cancer still remains incurable to date. Recent conception of the cancer stem cell (CSC) hypothesis possesses great potential to offer revolutionary advancements in understanding cancer and developing novel anti-cancer therapeutics from a different perspective. Particularly, the dormancy stage of cancer thought to be maintained by quiescent CSCs before the subsequent uncontrolled metastatic outbreak is a key intervention point of interest. Unfortunately current *in vitro* models of cancer do not faithfully recreate the *in vivo* complex metastatic environment, and the maintenance of CSCs *in vitro* has not been possible. The ability to reproduce an accurate metastatic microenvironment to maintain CSCs *in vitro* will provide new insights into cancer biology and anti-cancer drug discovery. The work described in this dissertation represents efforts toward this goal with sophisticated utilization of micro-technologies for 3D spheroid culture as a compelling solution to the development of such model.

6.1 Overall Contributions

Development of *in vitro* culture systems that properly model the growth behavior and microenvironment of cancer cells is essential for advancing the understanding of cancer biology and therapeutic design. This dissertation research contributed to the field of cancer biology by using micro-technologies to integrate complex tumor microenvironment components into an *in vitro* metastatic niche model that recapitulates a more physiologically-relevant growth characteristic of prostate cancer cells. This interdisciplinary research effort represents advancements in both biotechnological development and cancer research. Technologically we developed innovative 3D culture platforms for use in fundamental biological studies and drug discovery, and continually demonstrated additional system improvements throughout the works described in this dissertation. Biologically we established an *in vitro* prostate cancer metastasis bone marrow niche model and used it to gain insights into the biology of tumor dormancy regulation.

6.1.1 Technological Innovations

Micro-technologies offer great advantages to reproduce *in vivo*-like conditions in an accurate manner *in vitro*. The microfluidic spheroid culture device described in Chapter 2 represents an initial step in advancing current 3D culture systems and in establishing an accurate *in vitro* model reflective of the complex *in vivo* prostate cancer metastatic niche in the bone marrow. By integrating microfluidics, the system allows for

efficient formation and uniform control of 3D spheroids not otherwise possible in conventional methods. From a more practical perspective, the versatility of such 3D spheroid culture system to generate accurate *in vitro* models and its impact on biomedical sciences will be increased with the integration of simple fabrication process and high-throughput capabilities. Through the work described in Chapter 3, we have made such improvement in scaling up efficient formation and culture of 3D spheroids as hanging drops in a high-throughput format.

The 384 hanging drop array plate, offers high-throughput microscale 3D cell culture as accurate tissue or tumor constructs to obtain more in-depth knowledge of essential biological processes, model pathological diseases, and screen for novel therapeutics. We have revolutionized the approach to conventional hanging drop 3D spheroid cultures by turning droplet fluidics into a simple, user-friendly platform to enable practical use by a vast range of biomedical disciplines. This system has several compelling attributes such as material compatibility with hydrophobic drugs and standardized design compatibility with high-throughput screening instruments that can make a significant contribution to delivering the potential of expediting medical innovation and drug discovery processes.

For the plate to become more widely adopted, the system must not just provide high-throughput feature, but it should also feature a simple user-interface and be readily available. The hanging drop formation process in the platform makes 3D spheroid culture as straightforward as routine 2D cell culture. Furthermore, since the 384 hanging

drop plate is fabricated by injection molding, we have established a platform that not only is user-friendly and cost effective, but can also be mass produced as an integral tool for immediate translational research applications. The platform greatly reduces the complexity of microfabrication required in the microfluidic device described in Chapter 2, making the technology more accessible to a broad range of users. As the high-throughput 3D culture platform becomes widely adopted by researchers across multiple fields in academia disciplines, medical clinics, and the pharmaceutical/biotech industries, the volume of meaningful data obtained by studying and screening on 3D cell models will increase dramatically, thus, more accurately elucidate key biological processes, predict clinical efficacy, and eventually expedite the drug discovery process.

To further enhance the practicality of the platform, the plate must also allow for stable-long term culture and robust performance under high-throughput screening assays. These issues have been well addressed by the work described in Chapter 4. However, currently the spheroid cultured as the hanging drops in the platform can only be imaged by taking the plate out of the humidification chamber and therefore subjecting the hanging drops to evaporation and compromising the sterility of culture. Future addition of a thin clear plate filled will water that tightly fits underneath the hanging drop plate is envisioned to allow automated microscopic imaging for extended period of time, which is a critical component in high-throughput screening applications.

6.1.2 Biological Advancements

From the biological standpoint, conventional *in vitro* and *in vivo* models are limited in their ability to study the dormancy state of cancer metastasis due to technical difficulties associated with inducing metastatic dormancy in animals and recreating the complex microenvironment found in the distant metastatic sites. 3D co-culture systems with carefully engineered patterns will overcome the limitations of conventional methods and enable the reproduction of physiologic and pathologically-relevant environment *in vitro*, which may eventually contribute to establishing better understanding of the role of tumor microenvironment in a variety of cancers. Specifically, the use of 3D co-culture spheroids throughout this dissertation research provides the capabilities to properly mimic the tumor microenvironment with inherent oxygen and nutrient gradients. Co-culture spheroid is therefore an integral and compelling tool in studying cancer biology, and it especially has promising applications for CSC culture and maintenance. The versatility of 3D co-culture systems will be further enhanced with the combination of spheroid size control and the various patterning techniques presented in Chapter 4. The ability to recreate complex delicate organizations found in *in vivo* systems will provide a platform for tissue engineering and *in vitro* tumor models that may be immediately interesting and useful in regenerative medicine and other therapeutic designs.

6.2 Summary

We have taken the initiatives to study tumor dormancy by establishing an *in vitro* prostate cancer micrometastases dormancy model using micro-technologies. The

engineered bone metastatic niche is subsequently used to study tumor dormancy, and can potentially be applied to anti-cancer therapeutic development as screening and testing model. Specifically, we first developed a 3D prostate cancer co-culture spheroid construct in a microfluidic device and characterized the growth behavior of the prostate cancer cells. The recapitulation of a more physiologically-relevant prostate cancer growth rate in these co-culture models provided insights into the metastatic niche. Next, we developed an innovative high-throughput hanging drop platform for long-term 3D spheroid culture and explored a wide range of techniques to engineer micro-scale 3D tissues and tumors. Such platform provided a user-friendly and practical solution to the obstacles hindering researchers from adopting the physiologically-relevant 3D cultures. Finally, to follow up on our finding of the quiescent behavior of the stem cell-enriched subpopulation of prostate cancer cells in the co-culture spheroids, we investigated the underlying biology of prostate CSC and cancer dormancy in the metastatic niche in more detail. The described work represents advancements in *in vitro* 3D culture systems and models for cancer metastasis. Despite these advances, the current metastatic prostate cancer model may still require further optimization in future research, which can be built upon the 3D culture systems and techniques developed in this dissertation research.

6.3 Future Directions

Since we have not completely validated the quiescent, dormant state of prostate cancer cells in the co-culture spheroids described, the current spheroid “niche” should be

refined and optimized for dormant prostate cancer cell culture before proceeding to actual anti-cancer drug screening. Given the quiescent, non-proliferating behavior of the $CD133^+$ subpopulation of PC-3 cells inside co-culture spheroids found in Chapter 2, it is promising to pursue the engineering of an *in vitro* prostate cancer dormancy niche from the CSC-enriched subpopulation. The quiescent cell cycling state and the maintenance of CSC markers should be confirmed using flow cytometric analyses as described in Chapter 5. When further refinements of the niche are required to induce prostate cancer cells into dormant states, the optimization process could be easily accomplished using the 384 hanging drop array plate described in Chapter 3. Multiple conditions could be tested simultaneously given the high-throughput capability of the platform. Feasible factors to manipulate include different co-culture ratios of the cancer and support cell types, and different spatial localization and distribution of the different co-culture cell types within the spheroid constructs. The effect of these different conditions on the prostate cancer cell proliferation rate should be investigated. Patterning the location of specific co-culture cell types within a spheroid can be achieved using techniques presented in Chapter 4. Complex patterns (Figure 6.1) of the co-culture cell types are envisioned to be engineered by integrating a combination of concentric layer patterning with side-by-side Janus spheroid patterning. Sophisticated patterning and precise localization of the different niche components within co-culture spheroids would allow for exploration of the different roles of the endosteal versus the vascular niche. The ideal dormant metastatic niche should allow for the culture and maintenance of quiescent progenitor-like prostate cancer cells that often escape from conventional chemotherapeutic agents that target actively proliferating cells. Various factors from the cancer and support cells

can also be manipulated through knockdowns of key genes implicated in cancer stem cells, metastasis, and dormancy. This will provide a greater understanding of the underlying molecular mechanisms in regulating dormancy that could potentially lead to the elucidation of new cellular and molecular targets for anti-cancer therapy. Collectively, these research efforts will pave the way for screening of drugs against the established *in vitro* 3D dormant prostate cancer bone micrometastases on the 384 hanging drop plate. The high-throughput and user-friendly 3D spheroid culture platform readily usable by clinicians also offers the capability to test anti-cancer drugs on patient-derived cells for special individualized treatments.

As an immediate first step to understand the prostate CSC population further, conventional anti-cancer drugs such as 5-fluorouracil (5-FU) that targets proliferation could be applied to bulk PC-3 co-culture spheroids (same model as presented in Chapter 2, but cultured in the 384 hanging drop array plate developed in Chapters 3 and 4). The PC-3 cell population would subsequently be isolated and then analyzed for the number of $CD133^+$ PC-3 progenitor cells that remain in the co-culture spheroid constructs. The actively proliferating $CD133^-$ subpopulation of PC-3 cells is expected to be killed by anti-proliferation drugs while the quiescent $CD133^+$ subpopulation of PC-3 cells is expected to be resistant to the anti-proliferation drugs. Therefore, the remaining prostate cancer cells to be analyzed are expected to be enriched in the $CD133^+$ progenitor population. Alternatively, PC-3 cells could be sorted into $CD133^+$ and $CD133^-$ subpopulations prior to the formation of the co-culture spheroid constructs. Anti-cancer drugs would then be applied to both $CD133^+$ and $CD133^-$ PC-3 co-culture spheroids, and the effect of the

drugs on these two subpopulations of PC-3 cells would be compared. After drug treatment on the co-culture spheroids and isolating the prostate cancer cells, QPCR can be performed for the $CD133^+$ subpopulation (and possibly the $CD133^+/CD44^+$ subpopulation) versus the entire population to explore and compare the expression levels of key stem cell and metastasis relevant genes. 3D co-culture of prostate cancer cells with osteoblasts and endothelial cells is expected to affect the gene expression levels in prostate cancer cells as compared to conventional 2D mono-cultures (as explored in Chapter 5). This will provide greater insights into the true prostate CSC markers as well as the underlying mechanisms regulating the prostate CSCs. Altogether, the development of the 3D prostate cancer co-culture spheroid model as well as the high-throughput hanging drop array plate will become essential and useful tools in studying prostate CSCs from a novel approach to provide ground-breaking impacts in the field.

6.4 Concluding Thoughts

The work described here does not signify that we have cured cancer. Nevertheless, it marks a significant step towards the development of a revolutionary class of anti-CSC drugs that seems promising in eradicating cancer at the dormancy stage before malignant cancer cells propagate and develop into metastatic outbreak that is often lethal. The prostate cancer bone metastasis niche model has brought valuable insights to cancer biology. It also serves as an accurate model that bridges the gap between conventional artificial 2D monolayer systems and the actual *in vivo* environment. The

384 hanging drop plate further represents a technological breakthrough that could potentially revolutionize the current 3D cell culture standards in biomedical disciplines and drug screening platforms in the pharmaceutical industry.

Development of novel anti-cancer therapeutics is an interdisciplinary effort that requires contributions from a range of scientific and engineering fields in academia and industry. Our work is only a small part of a continual and collective endeavor in realizing the goal of curing cancer. Together, with huge ongoing efforts and innovations from around the world dedicated to finding a cure for cancer, the future will witness exciting medical breakthroughs and advancements in oncology. Finding a cure for cancer is not a simple problem, but it will be within our reach in the near future as we unravel the underlying cancer progression mechanisms step by step. As simple but powerful tools, *in vitro* 3D culture systems and models for physiological and pathological tissues are envisioned to have tremendous impact on biological studies and drug discovery, and will continue to serve as the fundamental basis for more biomedical applications to come in the future.

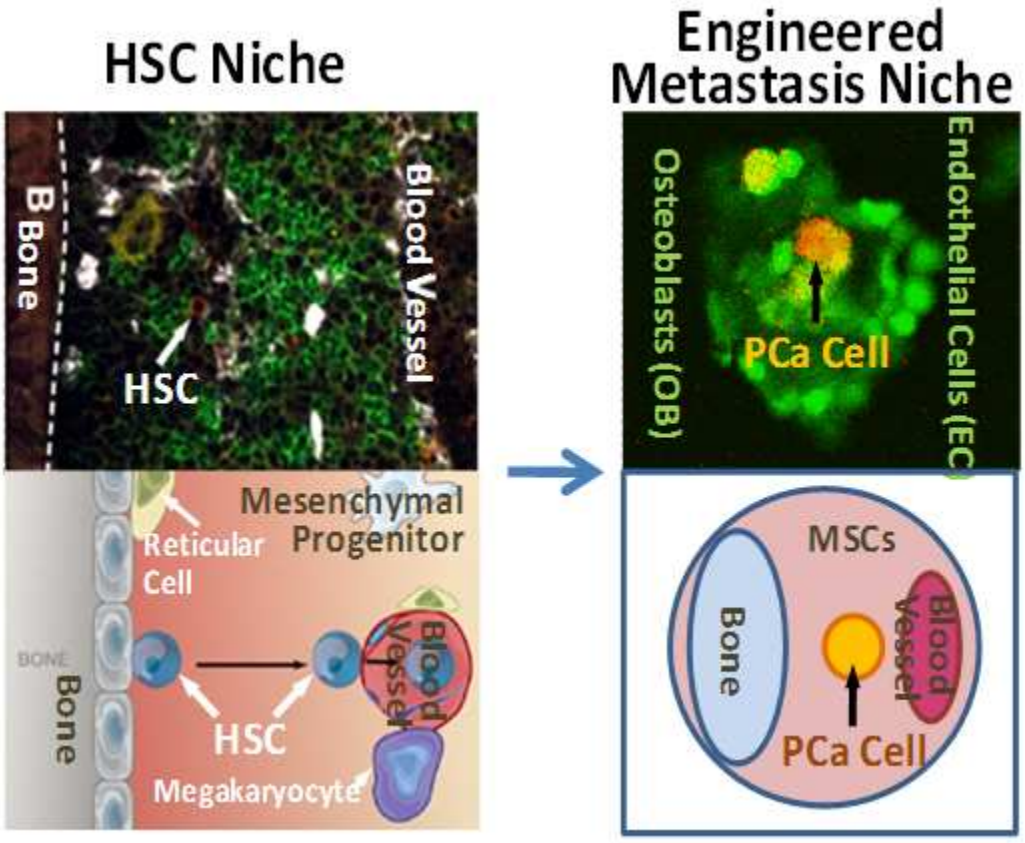

Figure 6.1. Schematic illustration of an engineered metastasis niche with the various component cells spatially patterned to model the *in vivo* hematopoietic stem cell (HSC) niche.